Structure and evolution of central and south Hadeland, the Oslo Region

Joakim Skreden Erga

Master Thesis in Geodynamics and Basin Studies

Department of Earth Science

University of Bergen

June 2022

Abstract

The Oslo Region has been influenced by at least two major tectonic events: Contraction and formation of the Caledonian orogeny as a result of plate convergence and, later, extension and formation of the Oslo Graben in Permian. Hadeland, situated in the northern part of the region, has been of particular interest for geologist to understand the geological evolution of the Oslo Region. However, until recently, the folded and thrusted 425 Ma old sedimentary sequence which exhibits typical thin-skinned foreland structures has been difficult to map out in a desired quality due to poorly exposed outcrops. Also, the structural timing and evolution is not fully understood. Relatively new LiDAR data allow for diagnostic structural patterns to be exposed, and to review both LiDAR's potential in bedrock mapping and Hadeland's structural geology in a new light. Calcite samples have been obtained and dated utilizing their U-Pb relations in an attempt to uncover the structural evolution of the area as well as pinpointing exact dates for deformational events in the Oslo Region.

Results from this thesis have produced a new 1:50 000 bedrock map covering central and south Hadeland. The map shows significant improvements to the existing map, clearly displaying the advantage provided by LiDAR data. Based on the new delineations, a geologic cross-section has been constructed, and new calculations of Caledonian shortening indicates a minimum of 30 % shortening of the affected strata by folding and thrusting. Seven out of 34 mounts sent for U-Pb dating proved datable but produced relatively inconclusive results with high uncertainties. Only one sample with an estimated age of 236 ± 39 Ma correlated with the Permian rifting.

In summary, this thesis has shown the efficiencies and strengths of LiDAR data as a tool in bedrock mapping, but also some of the shortcomings. The new and improved bedrock map points toward a larger displacement caused by thrusting than previously thought, a finding which is likely due to the improved delineations introduced by LiDAR data in mapping. In addition, total shortening of the area is postulated to be in the range of 38-45 %, indicating that differences in shortening in the mid-Ordovician to Silurian successions might be larger from north to south than previously estimated in the region. While the majority of dated calcite samples are interpreted to be from reactivation of faults and fractures in the latest 35 Ma, successful dating of the Permian Rift indicates that the method may still have validity in the Oslo Region, but it requires a larger and more comprehensive field campaign.

Acknowledgements

This thesis is part of my MSc degree in Geodynamics and Basin studies at the Department of Earth Science, University of Bergen. First and foremost, I wish to thank my main supervisor Prof. Atle Rotevatn for valuable guidance, critical discussions, and comments both during the field and throughout the writing process. You are always encouraging and positive. I would also like to express my sincere gratitude to my co-supervisors Prof. Haakon Fossen for contributing with valuable feedback on the structural geology, Sci. Björn Johan Emil Burr Nyberg for your expertise in QGIS, and Cand. Real. Ragnar Knarud for your exceptional passion for- and general knowledge about the geology at Hadeland. Our several-hour-long meetings have definitely helped me stay on track.

A special thanks goes to Åse Hestnes for phenomenal assistance in sample preparations, general feedback, and motivating conversations. Andreas Lambach Viken is thanked for mount preparations in the lab, and Dr. Kerstin Drost from Trinity College Dublin for performing U-Pb dating of calcites, and providing me with precious feedback. My brainy big sister MSc. Amalie Skreden Erga is thanked for comments and feedback on the text. Also, I want to send my gratitude to Anne Margrethe Knarud and Ragnar Knarud for great hospitality and the elaborate meals through my stay at your place in Hadeland. It was a joy!

Thanks also to my fellow students at the Department of Earth Science for some great memories through all of the five years. A special thanks goes to the members of Babesa® as well as Andreas Braut, Hanna Braut, Bendik Brustad and Jørgen Sømme for putting my mind on other stuff and feeding me with positive energy through the process of writing.

Finally, I would like to thank my family for unlimited support, and for always believing in me. This final year would not have been manageable without you.

Joakim Skreden Erga

Bergen, June 2022

Contents

1 Introduction

This chapter introduces the rationale and background of the study, its aims, and the position of the study area.

1.1 Rationale and background

The Hadeland area has been of interest to geologists for many decades due to its complex stratigraphy, the prominent geological difference between the north and the south, and geographical position in the Oslo Graben (Braithwaite and Heath, 1996; Morley, 1987b). The uppermost Ordovician and Silurian stratigraphy was described in 1908 by Johan Kiær (Kiær, 1908) and revised by multiple geologists in the following years (e.g. by Holtedahl and Schetelig, 1923; Størmer, 1943; Størmer, 1945; Owen et al., 2001). The relatively incompetent lower Ordovician shales in the north and the more competent upper Ordovician and Silurian succession further south have been influenced by Caledonian thrusting and Permian extension. This has resulted in a faulted and thrusted succession above a detachment horizon overlaying the autochthonous Precambrian crystalline basement (Morley, 1987b). These structures are well known but relatively crudely mapped, leaving room for improvement in the resolution of mapped structures by taking advantage of new technology provided by LiDAR hillshade images from Kartverket (2015). They allow for diagnostic, structural patterns to be exposed that are challenging to map in the field or by aerial photos due to the poorly exposed and highly drift-covered state of the area (Figure 1.1). Also, the timing and nature of deformation in the area is not fully understood.

LiDAR has great potential in delineating and mapping bedrock geology in Scandinavia, but has to date not been used to a great extent (Pavlis and Bruhn, 2011; Johnson et al., 2015). This study utilizes relatively new LiDAR data from Kartverket (2015) and combines them with stratigraphic and structural field observations to update parts of the 1:50 000 Gran bedrock map in areas where LiDAR data is found to be a beneficial tool. The resulting map will provide a basis for the study on large scale structures in central and south Hadeland, and new estimates on Caledonian shortening to constrain the structure and evolution of the study area. It will also enable discussions on how and if LiDAR data should be implemented in bedrock mapping, as well as placing central and south Hadeland's structural geology in a regional context. U-Pb dating of calcite has been attempted in this thesis, but the geochronological results were

inconclusive. The methodology and results are nevertheless described to document this aspect of the work for possible later studies in the Oslo Region.

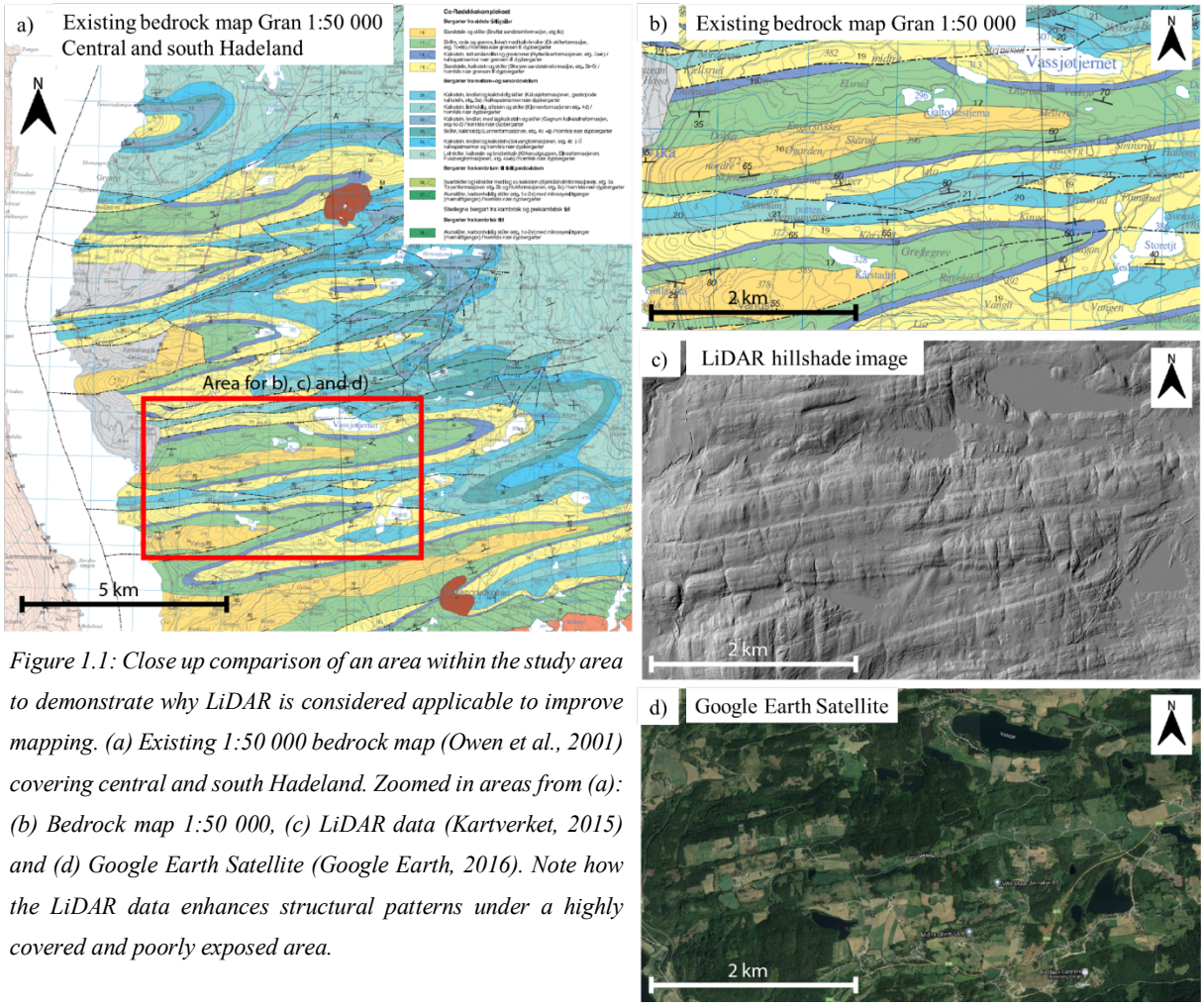

Figure 1.1: Close up comparison of an area within the study area to demonstrate why LiDAR is considered applicable to improve mapping. (a) Existing 1:50 000 bedrock map (Owen et al., 2001) covering central and south Hadeland. Zoomed in areas from (a): (b) Bedrock map 1:50 000, (c) LiDAR data (Kartverket, 2015) and (d) Google Earth Satellite (Google Earth, 2016). Note how the LiDAR data enhances structural patterns under a highly covered and poorly exposed area.

1.2 Study aims

The main aims of this study are to:

1. Improve the mapping of key units and structures, and to create an improved map and geological cross-section with basis in existing geological maps and new, airborne LiDAR data. The results of this will be used to update part of NGU's Gran 1:50 000 bedrock map from this area.
2. Evaluate the benefit of high-resolution LiDAR for bedrock mapping in improving existing NGU maps at a 1:50 000 scale and compose a workflow for implementation of LiDAR data in bedrock mapping.
3. Characterize the structural style of the area based on a combination of digital mapping and outcrop work, and estimate the amount of (Caledonian) shortening in the area.

4. Temporally constrain deformation/fluid events using U-Pb dating of calcite mineralization in faults and veins in the area, targeting Caledonian compressional structures as well as Permian extensional structures.
5. Based on the above, synthesize the spatial and temporal structural evolution of the study area.

1.3 Study area

Central and south Hadeland, the study area in this thesis, can be seen in Figure 1.2. Today, the term "Hadeland" is commonly used for a geographical area including the municipalities of Jevnaker, Lunner and Gran. The district is outlined following this definition, but, in this thesis, north Hadeland is used for the shale dominated area north of the study area, studied by e.g. Morley (1987b). Central and south Hadeland is the sand- and limestone dominated succession highlighted on the existing bedrock map from Owen et al. (2001) (Figure 1.2). This is in line with nomenclature from existing geological studies from the Oslo Region when referring to Hadeland and its geology.

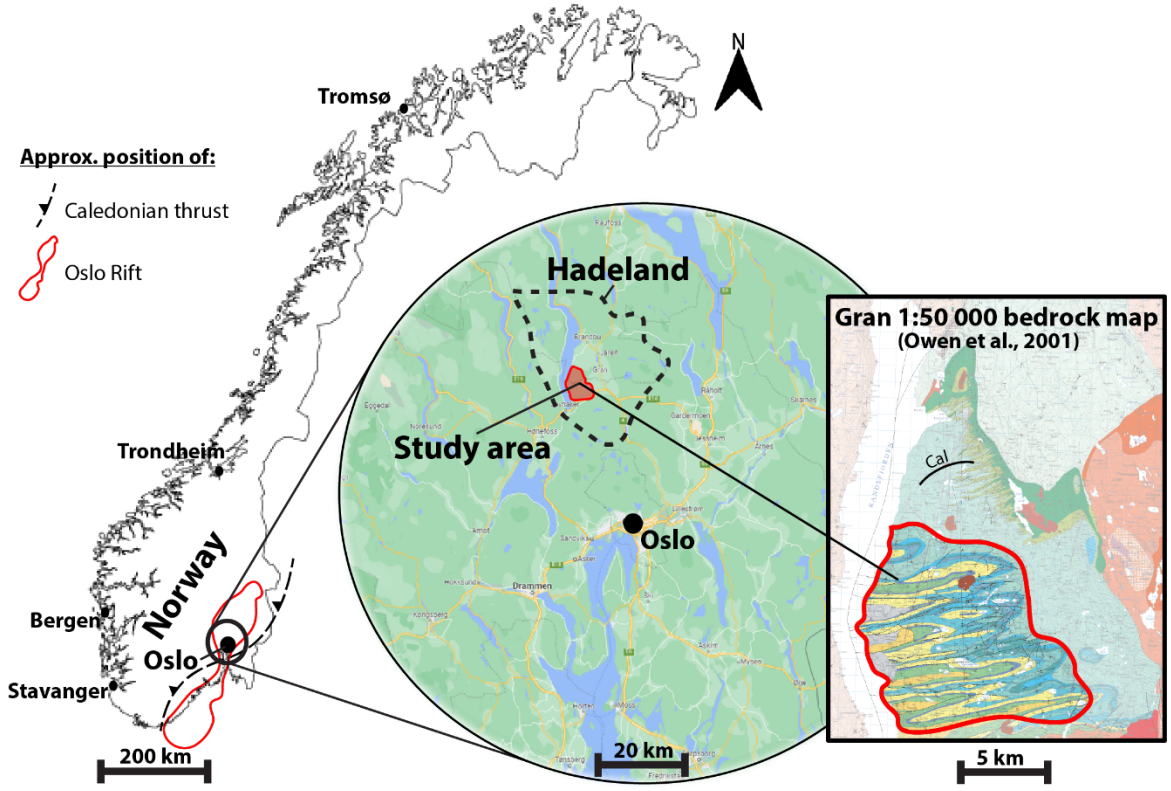

Figure 1.2: Study area in this thesis. "Cal" refers to the northernmost area where calcite samples were collected.

2 Geological setting

This chapter gives an introduction to the geological setting of the Hadeland area. Major geological events through time, earlier studies from the area, and the early Paleozoic successions found in the Oslo Region, as well as at Hadeland, are addressed.

2.1 The Oslo Region

The Hadeland area is situated within the northern part of the Oslo Region which is a graben structure accommodating fossiliferous rocks of Lower Paleozoic age in a 40-70 km wide belt extending 240 km from Langesund in the south to Lillehammer in the north (Figure 2.3) (Bruton et al., 2010). It is a non- genetic geographical term (Sundvoll and Larsen, 1994) first defined by Størmer (1953), covering about 10 000 km^2. The down-faulted successions are preserved from complete erosion by the Permian- made graben structure (Bruton et al., 2010), and are surrounded by a Precambrian basement terrain formed by crustal accretion between 1900- and 800 million years ago (Ma) (Heeremans et al., 1996). The following subchapters accommodates a brief introduction to the main tectonic events which have influenced and shaped the area to its present- day appearance through time.

2.1.1 The Caledonian orogeny (Late Silurian to Early Devonian)

The Swedish geologist Alfred E. Törnebohm first suggested vast thrusting of the Caledonian units as early as 1888 (Fossen, 2010). In his work "Det Centrale Skandinaviens Bergbygnad", (translated: The construction of the Central Scandinavian Orogeny), he described allochthonous transported units where younger sediments were overlayed by older sediments. Never before had thrusting of allochthonous units of distances more than 100 km been suggested, resulting in diverse receptions by the public (Bjørlykke, 2017). It would take several decades before his theory was recognized among Scandinavian geologists, but since the early 1900s, several geologists have mapped and explored the compound system of thrust- related structures throughout the orogen of the Caledonides (Fossen, 2010) where Törnebohm's theory of vast thrusting often constitutes the ground foundation.

In the Late Precambrian, rifting processes resulted in the formation of two paleocontinents; Laurentia and Baltica (e.g. Dewey, 1969). The main site of rifting, which at a later stage evolved into a passive margin, is assumed to have been orientated approximately parallel to the coast of present day Norway (NE-SW) (Morley, 1989). The Caledonian orogenic belt is a result of

convergent motions of Laurentia and Baltica in Ordovician and Silurian times, and the present architecture of the Scandinavian Caledonides (seen on Figure 2.2) also displays evidence of subsequent late- to post orogenic extension and profound erosion (Fossen and Dunlap, 1998; Hossack and Cooper, 1986; Fossen, 2010; Jakob et al., 2019). During the Paleozoic era, the Oslo Region was initially situated at the mid-latitudes, but an estimated rapid northward drift during the Ordovician resulted in a position near the equator during the Silurian (Perroud et al., 1992; Cocks and Torsvik, 2002; Cocks and Torsvik, 2005; Bruton et al., 2010).

The Caledonides were generated as a result of subduction of the Baltican margin, overlapped by the Laurentian margin of Greenland. The orogenic belt is branching from the Appalachian belt in the southwest and to the less prominent Polish Caledonides to the southeast (Fossen et al., 2017). The making of the orogeny in Norway is estimated to have occurred over a time span of 20 Myr, starting between 430-425 Ma, and can be referred to as the Scandian event or orogeny on the Baltic continent. This is one of four major orogenic phases from the Caledonides in Norway (Figure 2.1), in addition to a later extensional collapse (e.g. Roberts, 2003; Fossen et al., 2017).

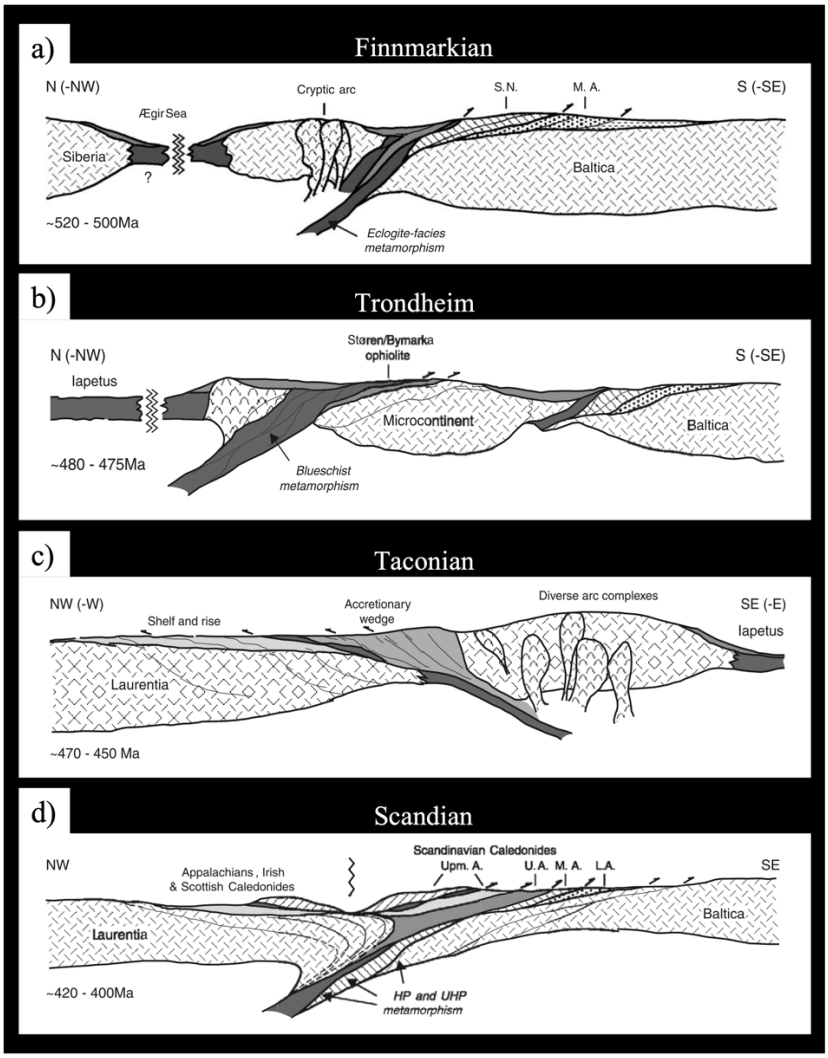

Figure 2.1: Schematic, composite profiles compiled from Roberts (2003) illustrating the four main orogenic phases of the Caledonides in Norway. (a) The Finnmarkian accretionary event in late Cambrian times. The profile spans from the northernmost parts of Norway and part of Sweden. S.N.- Seve Nappes; M.A.- Middle Allochthon. (b) The Trondheim event. This is related to mid-Norway around the Trondheim area. The Finnmarkian accretion nappes can be observed further S/SE and the Gula microcontinent is covered by the Gula complex. (c) The Taconian event. Subduction and accretion occurred along the continental margin of Laurentia, where some of these complexes later were detached and re-transported onto the nappes carpeting Baltica after the Scandian event. (d) The major Scandian collisional event between Baltica and Laurentia. Assemblage of numerous thrust sheets formed by earlier events. L.A., M.A., U.A. and Upm.A. - Lower, Middle, Upper and Uppermost Allochthons, respectively. All text and profiles from, and slightly modified after, Roberts (2003).

Deformation resulting from the collision continued into the Devonian, until uplift of the thrust belt occurred in phases. The rising orogen became exposed to widespread erosion, and continental sandstone deposits derived (Morley, 1983).

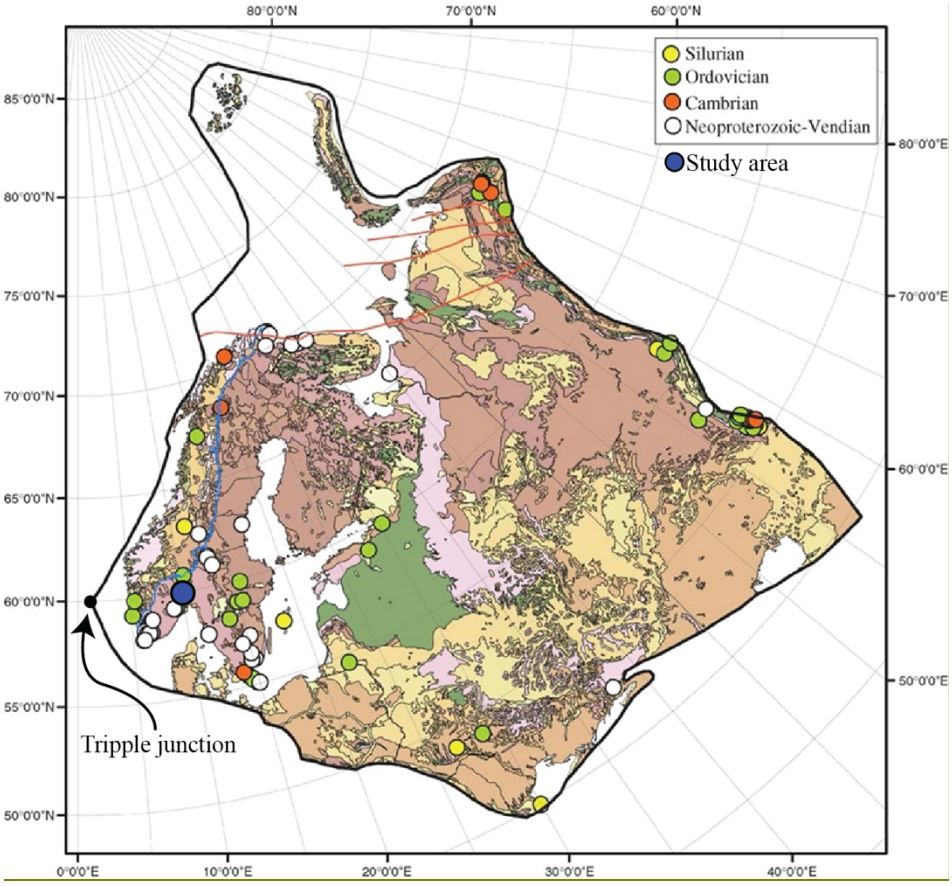

Figure 2.2: Baltica with today's geology. From Hearn (2003), simplified by Cocks and Torsvik (2005). Colored circles are areas selected for paleomagnetic data (not this study), and the blue line is the estimated position of the Caledonian front. From (Cocks and Torsvik, 2005).

In Figure 2.2, which is a map displaying Baltica with the present-day geology, a triple junction can be seen in the southwest. At this junction, Laurentia was located to the north and west, and the microcontinent Avalonia to the south. The suture between Laurentia and Baltica can be revealed by studying the complexities from the Caledonides (Cocks and Torsvik, 2005). Nappes found in Norway carry Lower Ordovician benthic faunas which have their origin at quite some distance from Baltica (Cocks and Torsvik, 2002), close to Laurentia or in the Iapetus Ocean. Sediments from post- rift continental margin deposits of Cambro-Silurian age and the foreland basin were deposited and incorporated in the advancing thrust sheet developed during the creation of the Norwegian Caledonides, as illustrated in Figure 2.1 (Nystuen et al., 2008). In the Oslo Region and the Southern Norway, deposits from the Late Proterozoic to Early Paleozoic are placed sectionally unconformable on either the Baltican basement or allochthonous crystalline rocks (Bingen et al., 2011).

Nappes

Nappes are large transported sheets of rocks, or deposit units, and they are a dominant structure in the Caledonides (Korja et al., 2008). One of the deposit units, the Osen-Røa thrust sheet, is the most external tectonic unit in the Southern Norwegian Caledonides, estimated to originally have covered more than 100 000 km^2 (Morley, 1989). The first nappe transition along the western margin of the Baltican shield is dated to approximately 430 Ma (Ogg et al., 2004; Bruton et al., 2010). Remnants of the Caledonides are tracible from the Stavanger area in west and northeastwards to Valdres, following to the northern parts of Mjøsa in the east and further into Sweden for up to 240 km from Oslo (Bruton et al., 2010). The width of the remnants are averaging at 200 km, with an maximum of 500 km and 1800 km in length (Roberts et al., 1985; Hossack and Cooper, 1986). In contrast to Törnebohm's, at that time radical theory of thrusted allochthonous units of some 100 km's, evidences have increased the estimates of nappe displacement distances to be at least 1000 km (Gee, 1978). The nappes are divided into lower, middle, upper and uppermost allochthones, where the lower units have been transported shorter distances relative to the upper ones (Korja et al., 2008).

The geometry and strain of the nappe units are generally extensive, thin, sheet or wedge-shaped, and show an overall thinning towards the west (Nicholson and Rutland, 1969; Zachrisson, 1969; Roberts and Sturt, 1980). They display extensive high strains, especially in the basal zones (Roberts and Sturt, 1980).

The Osen-Røa nappe

The Oslo Region is situated in the Osen part of the Osen-Røa nappe complex, structurally placed in the lower allochthone (Nystuen, 1981). The nappe derived from a fault bounded cratonic basin, and has accommodated a total displacement towards the SE between 100 km (Morley, 1986) and 200-400 km (Nystuen, 1983), which is still a matter of conjecture in the literature. The Osen-Røa thrust is the sole thrust on which the nappe complex rests. It is a blind thrust, and for most parts, its presence is indicated by folds and subsidiary thrusts in the décollement moved strata above (Nystuen, 1983).

The structural style of the strata overlaying the thrust is variable both laterally from north to south, and stratigraphically. The Cambrian to mid-Ordovician strata is deformed by closely spaced imbricates in the north, while triangle- pop- up- and imbricate zones are typical for the south. Strata from the mid-Ordovician and Silurian are deformed by buckle folding with less

lateral variations compared to the older strata (Morley, 1987a). Increased resistance to deformation by increasing amount of competent Ordovician units southwards and upwards (stratigraphically) are used as the main explanation for the changes in deformation style by Morley (1986; 1987a).

Structural outline

Recent and previous structural data on the Caledonian deformation in the Oslo Region was by Bruton et al. (2010) systemized in a general structural synthesis where the area was divided into four structural subareas. The subareas are separated by major thrusts, and they are characterized by distinct structural styles and intensity of strain. Each level is associated with fault ramps, duplexes, and fold trains. The Osen-Røa Nappe Complex reflects a similar situation, where the Osen-Røa thrust is equal to the thrust for structural level 1; the basal thrust system, which runs through the Alum Shales.

The second structural level is known as the middle thrust system. This level also comprises a lot of stain, often localized in fault zones or ramp and flat systems. It goes from the Ordovician all the way up to the Silurian successions, and deformation is characterized by reverse faults, imbricate thrust sheets, and folds, often asymmetrical. Most of the exposed folds are second- and third order structures. The regional detachment zone in relation to level 2 has not been observed, but multiple sub-horizontal thrust branches can be seen or inferred (Bruton et al., 2010).

Level 3 have faults that are probably linked to level 2. Ramps with a complex geometry and thrusts that flattens below the competent sandstones in the Ringerike Group (Gr.) with open folding in areas with no thrusting is characteristic (Bruton et al., 2010; Vlieg, 2015). The uppermost structural level, level 4, is closely related to thrusting in level 2 and 3. This level only occurs in a few areas where the thrust faults have ramped through the Ringerike Gr. (and its equivalents) (Bruton et al., 2010).

2.1.2 The Oslo Rift (Late Carboniferous to Early Triassic)

After the Cambro-Silurian strata in the northern and central parts of the Oslo Region were influenced by Caledonian folding and thrusting, a peneplanation followed due to erosion (Henningsmoen and Dons, 1978; Neumann et al., 1992).

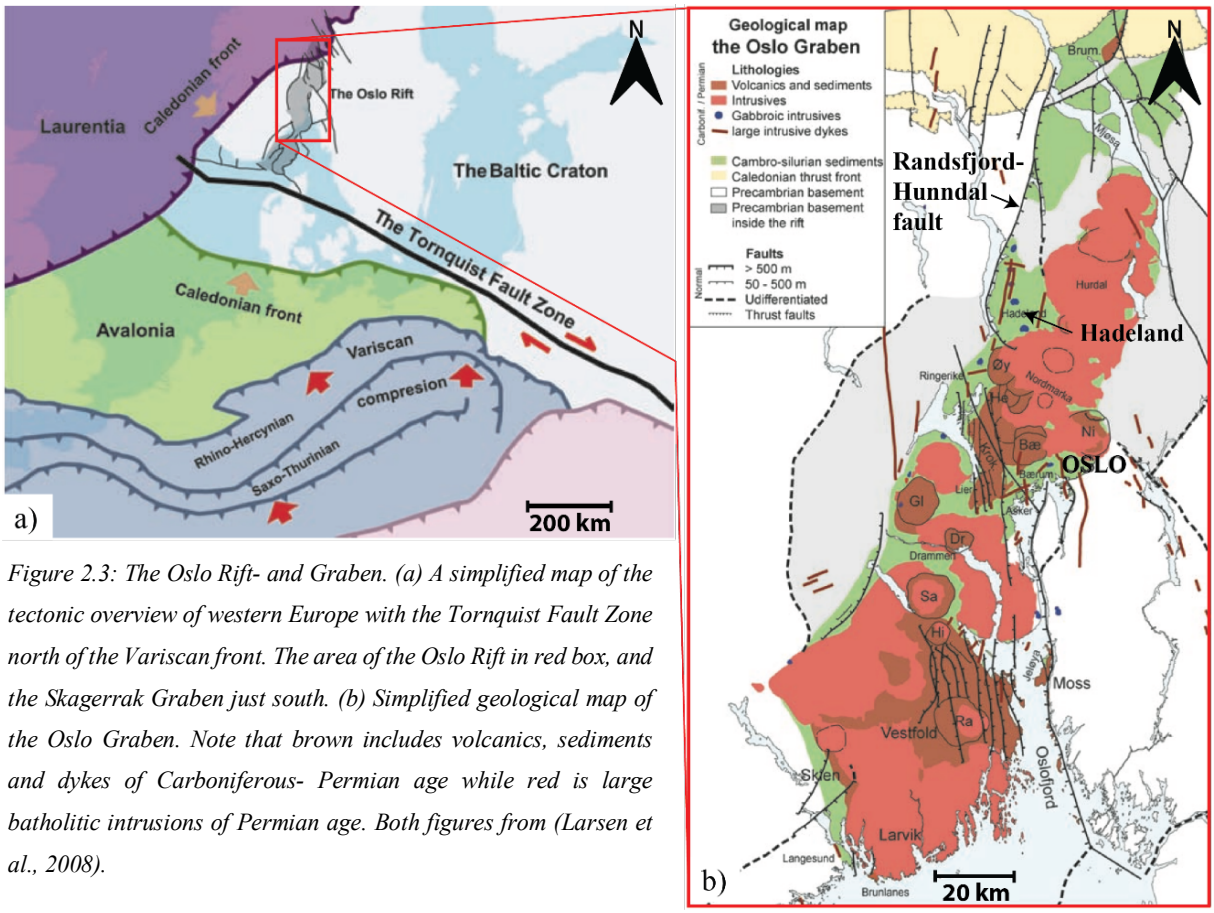

Figure 2.3: The Oslo Rift- and Graben. (a) A simplified map of the tectonic overview of western Europe with the Tornquist Fault Zone north of the Variscan front. The area of the Oslo Rift in red box, and the Skagerrak Graben just south. (b) Simplified geological map of the Oslo Graben. Note that brown includes volcanics, sediments and dykes of Carboniferous- Permian age while red is large batholitic intrusions of Permian age. Both figures from (Larsen et al., 2008).

The Oslo Rift (Figure 2.3a) is a Permo- Carboniferous graben system consisting of two main segments of Paleozoic rocks: the onshore Oslo Graben with a general N-S orientation and the offshore Skagerrak Graben with more of a NW-SE oriented strike (e.g. Ro and Faleide, 1992; Olaussen et al., 1994; Larsen et al., 2008). Volcanic intrusive- and extrusive rocks cover more than 75 % of the Oslo Graben (Figure 2.3b), which is characteristic and directly related to the tectonic evolution of the area (Ramberg and Larsen, 1978; Olaussen et al., 1994).

The evolutionary development of the rift was, by Ramberg and Larsen (1978), subdivided into six stages (Figure 2.4) where the large portion of magmatic rocks represents an important source of information (Neumann et al., 1992). The stages have later been revised by various geologists, including Sundvoll et al. (1990) and Larsen et al. (2008).

The oldest magmatic rocks in the Oslo Rift are dated to be 310 Ma, while the youngest are dated to 241 Ma. Six stages are still used to divide the general development of the Oslo Rift (Ramberg et al., 2007; Larsen et al., 2008):

1. The proto-rift forerunner to rifting.
2. The initial rift and first basaltic volcanism.
3. The rift climax, with rhomb porphyry fissure volcanos.
4. The mature rift, with central volcanos and caldera collapse.
5. The magmatic aftermath, with major syenitic batholites.
6. Rift termination, with the youngest small granite intrusions.

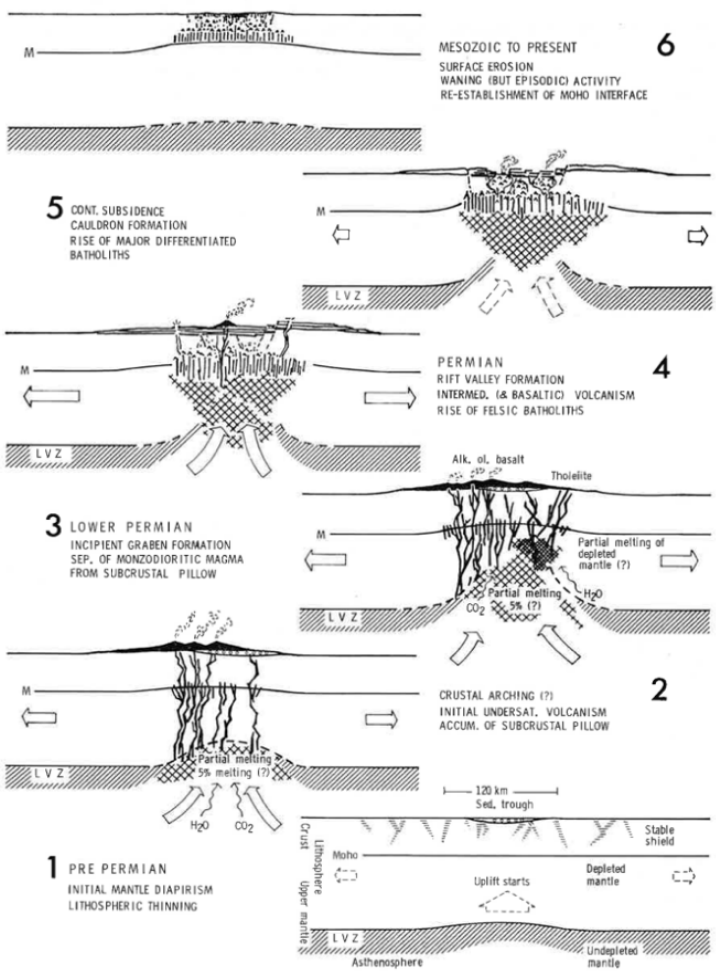

Figure 2.4: Cross-sections illustrating the originally proposed six stages of the development of the Oslo Graben. From Ramberg and Larsen (1978).

Rifting from stage 2 and 3 resulted in the major Randsfjord-Hunndal fault west of Hadeland in addition to normal faults at a smaller scale throughout the area. Five gabbro plugs are situated side by side from north to south in a relatively straight line. They are from stage 4 in the development and had relatively small basaltic magma chambers compared to the larger volcanos that later resulted in calderas and volcanic-dominated rocks, seen in Figure 2.3 (Ramberg et al., 2007).

2.2 Lithostratigraphy and evolution of the Oslo Region

The lower Paleozoic sedimentary successions found in the Oslo Region are well documented. They have since the 18th century been one of the major references for Norwegian geology due to its biostratigraphy which provides a time scale for dating the Caledonian tectonic events (Bruton et al., 2010). In later years, reworked and updated versions have been based on the foundation of the refined work provided by Kjerulf (1857), Brøgger (1882; 1887) and Kiær (1897; 1902; 1908). They presented an "etagen" (Eng.: level) nomenclature which is

predominantly based on lithostratigraphy and paleontological evidence through guide fossils, and originally consisted of eight divisions. The terminology was further developed and dilated to ten main "etagen" units with numerous sub-units and "shorthand symbols" of Arabic numerals succeeded by Roman and Greek letters (see Figure 2.5) by subsequent workers before the modern nomenclature was suggested (Henningsmoen, 1982). This newer division is a result from stratigraphic and sedimentological studies from the 1970s- and 80s. Different parts of the successions can be observed on a diverse set of locations within the Oslo Region, including Hadeland, where it accompanies Precambrian gneisses and Permian intrusive rocks (Owen et al., 1990).

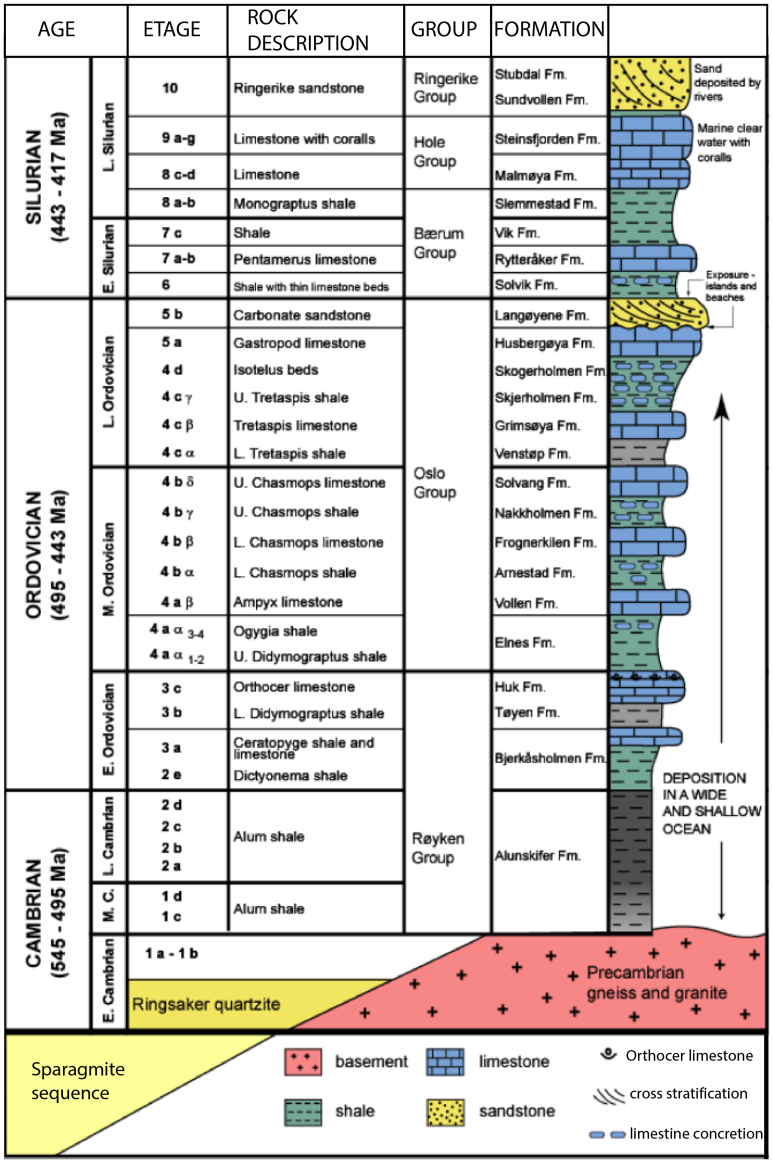

Figure 2.5: The stratigraphy of the Lower Paleozoic successions in the Oslo Region with both the old and newer nomenclature. Note that the lower parts of mid-Ordovician is divided in even smaller numerical sub-scripts, which is according to fossil content. From (Bjørlykke, n.d.).

2.2.1 Cambrian

In the transition from Early- to mid-Cambrian there is an unconformity, clearly seen on Figure 2.5. The Sub-Cambrian Peneplain with Precambrian gneisses and granites was submerged during a transgression, and sediments of mid-Cambrian age were deposited in an ocean with relatively low oxygen levels and high sulfur levels resulting in an anoxic environment and deposition of the Alum Shale Formation (Fm.). The peneplain is recognized by its moderate to

high degree of weathering, and it is modified by a series of events: Caledonian and post-Caledonian faulting, uplift, and subsidence. In the Oslo Region and Southern Norway, it is well preserved away from the Caledonian erosional nappe front, as well as in tectonic windows (e.g. Kiær, 1917; Spjeldnæs, 1955; Skjeseth, 1963; Nystuen, 1981; Gabrielsen et al., 2015). It is within the Alum Shale Fm. that the sole thrust of the Caledonian nappe duplex commonly detaches, linking the Sub-Cambrian Peneplain and its overlying sedimentary strata (e.g. Nystuen, 1981; Nystuen, 1983; Morley, 1986; Bruton et al., 2010; Gabrielsen et al., 2015).

2.2.2 Ordovician

The thicker Ordovician succession is a cyclic sequence consisting predominantly of shales, but with nodular layers of limestones and variable portions of thin beds consisting of sandstone (Brenchley and Newall, 1977; Owen et al., 1990). It is a shallowing sequence with tidal bars on the top (Bjørlykke, 1974; Brenchley and Newall, 1975; Morley, 1987b), and the period made its appearance with a worldwide transgression (Bruton et al., 2010). Generally, the sequence is characterized by a marine, epicontinental and subtidal depositional environment (Ballo et al., 2019), and is assumed to have an average thickness of around 470 m (Brenchley and Newall, 1977). In the Oslo Region, however, high sedimentation rates in the Upper Ordovician have resulted in local successions where the thickness is approaching 1 km (Owen et al., 1990; Bruton et al., 2010). The different formations can often be defined by cyclic variations in sediment composition. Faulting as a result of basement tectonics is considered to be an important factor for the considerable amount of siliciclastic material introduced during the Late Ordovician, but this assumes a tensional regime which at this point in time does not match well with the position of Baltica. The details are probably more complex (Brenchley and Newall, 1980; Braithwaite et al., 1995).

2.2.3 Silurian

Deposition of the marine rocks in the Silurian succession occurred in a similar environment as the Ordovician succession, in the foreland basin of the rising Scandian orogeny (Bruton et al., 2010). A widely recognized glaciation at the end of the Ordovician resulted in a fall of the sea level between 50 and 100 m (Brenchley and Newall, 1980). The transition into Silurian is marked by an abrupt transgression to deeper water with ice- melting on a global scale, and an eminent hiatus in selected areas in the region can be observed (Bruton et al., 2010). This disconformity is accompanied with a marked change in fauna, with the Ordovician retaining a

higher degree of provincialism compared to the more cosmopolitan faunas from the Silurian (Berry and Boucot, 1973; Sheehan, 1973; Baarli and Harper, 1986). The thickness of the succession reaches 650 m, and displays an immense diversity of both clastic- and carbonate richer facies (Worsley et al., 1983).

2.3 Geology of the study area – Hadeland

2.3.1 Overview

Hadeland is an area located about 50 km north of Oslo (Figure 1.1). Caledonian folding and thrusting of Cambrian to Silurian sedimentary rocks, combined with the stratigraphical and paleontological conditions, results in Hadeland being of particularly high interest. The complexity of the area is strengthened by numerous intrusions of Permian age, both as relatively large and eroded volcanic plugs and multiple dikes and sills throughout (Størmer, 1943; Morley, 1987b; Braithwaite and Heath, 1996). A map of the main geological units in a 250:000 scale from (Nordgulen, 1999) can be seen in Figure 2.6, displaying how the sedimentary successions contacts the surrounding plutonic granites and syenites east- and southwards, while 1500 Myr gneisses and amphiboles makes up the Precambrian bedrocks to the west and north. The western boundary is marked by the N-S oriented Randsfjord-Hunndal fault of Permian age (Lauritzen, 1973).

The structural style between northern and central/southern parts of Hadeland varies substantially. These variations are not a result of lateral-, but rather vertical variations where erosion has led to exposure of older Cambrian to mid-Ordovician rocks in north, similar to the rocks in northern Ringerike of same age.

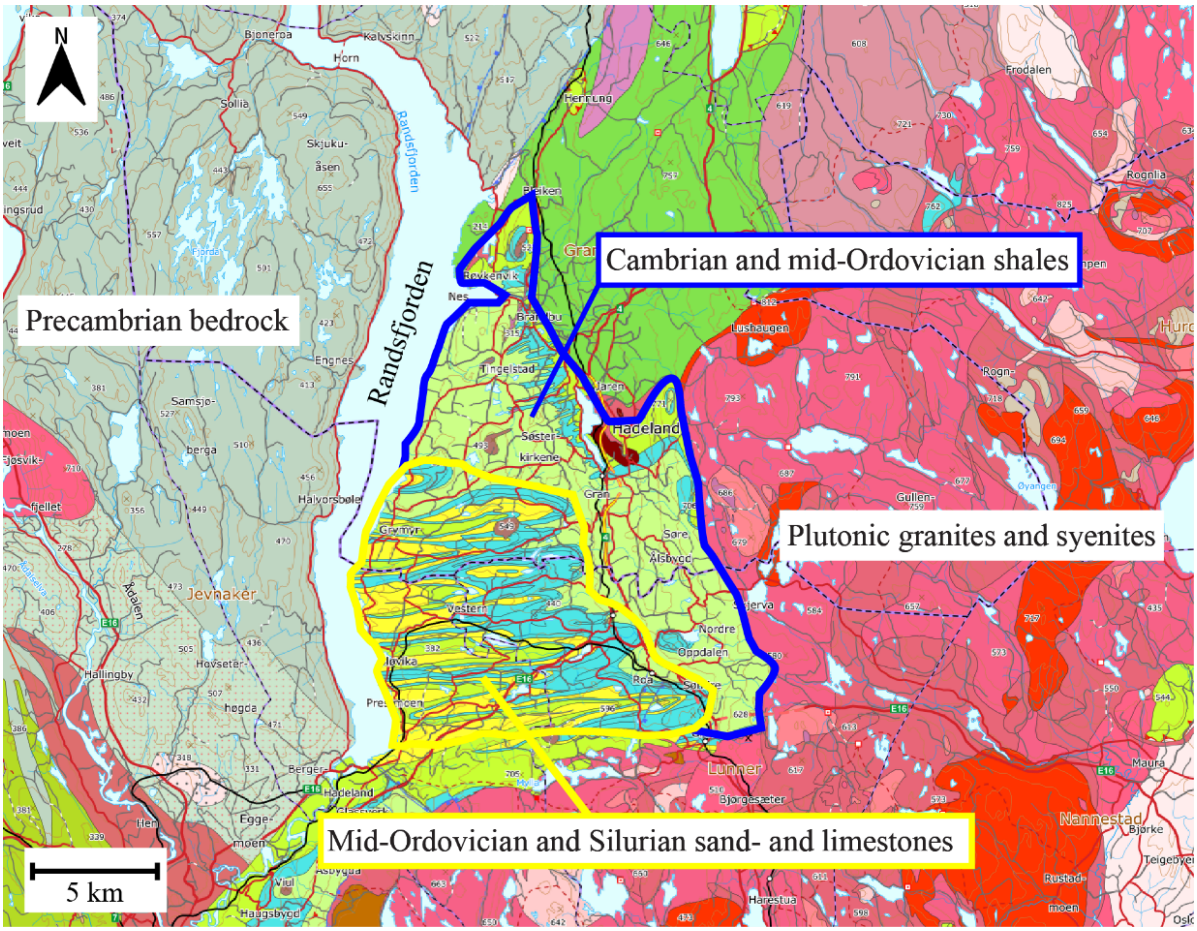

Figure 2.6: 1:250 000 bedrock map from Nordgulen (1999). Blue area marks where Cambrian and mid-Ordovician shales are situated north of the mid-Ordovician and Silurian sand- and limestones further south (in yellow, which is the area of focus in this thesis).

2.3.2 Earlier studies

The Cambro-Silurian successions in Hadeland has been known since the work of Kjerulf (1862; 1879) who published simple maps and profiles showing the more general folding of the area. Th. Münster further improved the mapping, serving as the basis for Kiær (1908) and later Holtedahl and Schetelig who published their map in 1923, pointing out the interesting relationship between the differences in north and south (Størmer, 1943).

Morley (1983) published an impressive work on the structural geology of the southern Norwegian Caledonides, where research at Hadeland were conducted in an attempt to construct a continuous balanced cross-section of the Cambro-Silurian rocks in the Oslo Graben. This later resulted in a more extensive publication focusing on the structural geology of north Hadeland (Morley, 1987b). To obtain a fuller understanding of the Hadeland area, Morley based his map on an unpublished thesis from A. W. Owen, which is also one of the main contributors for the current 1:50 000 bedrock map covering Gran today (Owen et al., 2001). Several other

publications from the area can also be found, many of which focuses on the stratigraphy and biota in the successions in the area (e.g., Størmer, 1945; Lauritzen, 1973; Braithwaite et al., 1995; Braithwaite and Heath, 1996).

2.3.3 Lithostratigraphy of Hadeland

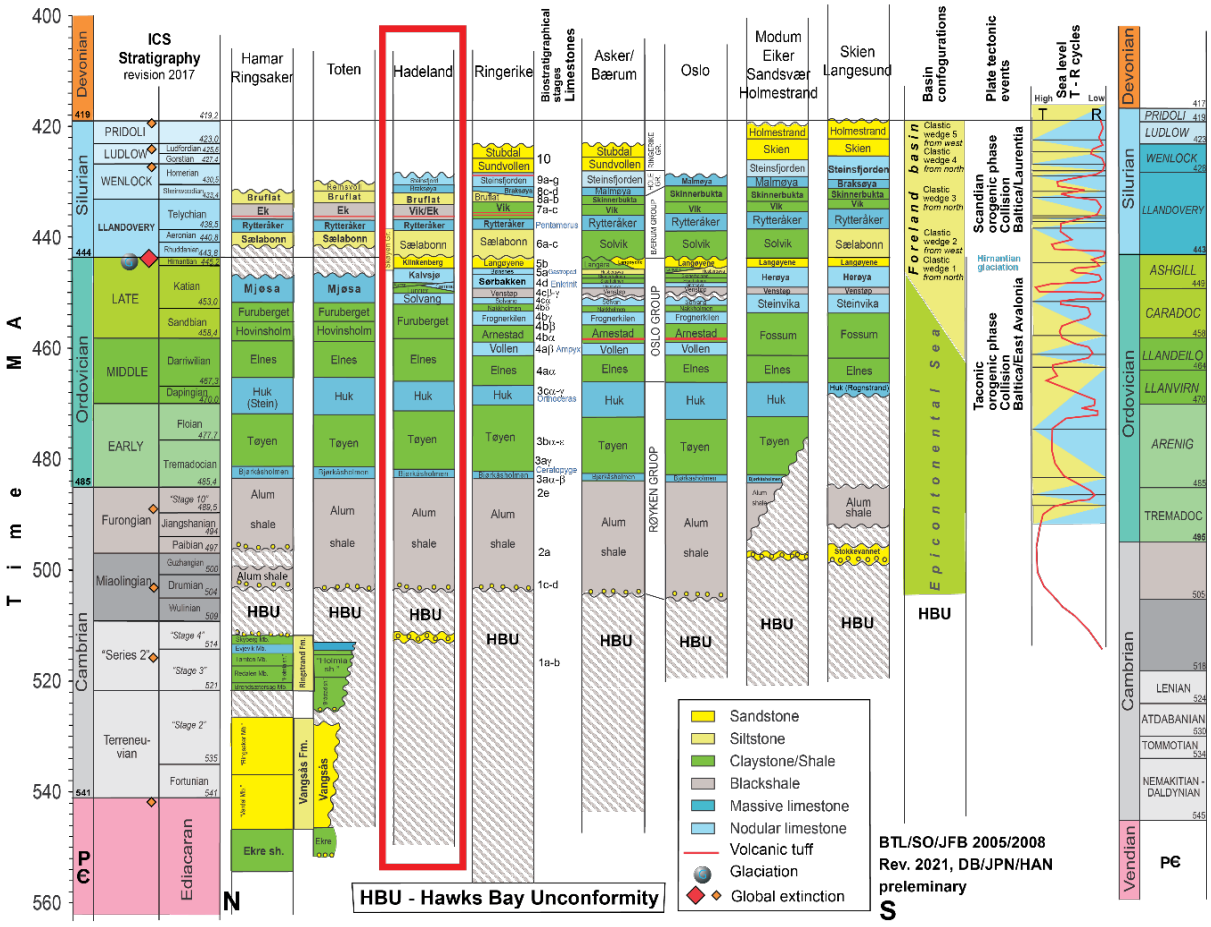

Figure 2.7: Lithostratigraphy of the Cambro-Silurian succession in the main areas of the Oslo Region from N to S. Hadeland is outlined in red box. The figure is preliminary made by Bjørn Tore Larsen, Snorre Olaussen and Joahn Petter Nystuen, rev. 2021.

The modern division for the successions found in the Oslo Region was established by Worsley et al. (1983) and Owen et al. (1990). These publications have been used to identify the different units and to map out the area, and they should be consulted for more comprehensive descriptions of the highly detailed stratigraphic column. An increase in competent sand- and limestone dominated formations when moving stratigraphically upwards at Hadeland can be seen in Figure 2.7. Some of the neighboring units found at Hadeland show similar features and are difficult to separate without a comprehensive knowledge about paleontological features. Hence, this study has combined some of the formations. A short summary of the main characteristics of the different units at Hadeland follows:

The Alum shale Formation

The Alum shale is present over a large part of the Baltoscandian shield with a thickness varying between roughly 30 to 100 m (Bruton et al., 2010). It has a very low $CaCO_3$ content and is enriched in different trace elements, for example uranium and vanadium. Black, organic rich shales are the main component, while dark bituminous limestone (also called stinkstone) in discontinuous beds and concretions up to meters in size is typical for the formation (Owen et al., 1990). The origin of Alum shales exposed in the Vigga valley in Gran, and at the Kistefoss area in Jevnaker, have been studied by Morley (1983; 1987b). The main basal thrust between the Pre- Cambrian bedrock and the sedimentary succession is constricted to the Alum shale Fm., resulting in a high degree of deformation above a basal conglomerate and an autochthonous less deformed thinly layered alum shale succession.

The Bjørkåsholmen Formation, the Tøyen Formation and the Huk Formation

As with the existing map of Gran (Owen et al., 2001), these three formations have been grouped together in this thesis. Bjørkåsholmen Fm. starts with an abrupt change from the Alum shale into a pale and weathered nodular limestone. It is about 1 m in thickness, and it is intercalated with thin shales. The transition to the overlying Tøyen Fm. marks an abrupt change with higher shale content. The Tøyen Fm. is measured to be 15 m thick at Hadeland with subordinate horizons of limestone in pale gray and black silty shales. Due to lack of fauna, it is not easily dated. The Huk Fm. succeeds with graptolitic shales of the Tøyen Fm., and has been measured at Hadeland to be approximately 7 m. It possesses three distinct limestone members, which are characteristic (Owen et al., 1990).

The Kirkerud Group (the Elnes Formation and the Furuberget Formation)

The Elnes Fm. is dominantly a shale unit. Due to it being less competent compared to underlying and succeeding units, deformation has resulted in a great number of folds and thrusts. Its thickness can therefore only be estimated, and faulted repetitions of the sequence can lead to overestimations. Suggestions have estimated between 60- and 120 m. In Hadeland, rusty and brown limestone nodules are present in the lower part of the unit, while in the middle part, 20 cm thick shale horizons are separating limestone nodules of 8 cm (Owen et al., 1990). The Furuberget Fm. has a base marked by 2 m calcareous sandstones at Hadeland. It is dominantly a shale unit with limestones and calcareous siltstones (Owen et al., 1990). It is within the Kirkerud Gr. that the second, upper detachment is interpreted to be located (Morley, 1983).

The Solvang Formation

The Solvang Fm. is a limestone unit containing interbedded calcareous shales in a varying amount. It is in the middle of two shale dominated units. Thickness measurements at Hadeland exhibits great variations between 70 m in central Lunner and down to 17 m on Tønnerud (Owen et al., 1990).

The Gamme Formation, the Kjørrven Formation and the Lunner Formation

The Gamme-, Kjørrven-, and Lunner Fm. constitute a relatively complex part of the stratigraphic column in Hadeland. Without biostratigraphic verifications in the field, these formations were deemed unfavorable to divide from each other when sedimentary facies are the main controlling factor of the lithostratigraphy. As a result, they are in this thesis combined in one unit. The Gamme Fm. is composed of nodular limestone with thicknesses up to 20 cm and little to no intervening shales. It is found to have a maximum thickness of 85 m near Grinda and is thinning towards north to about 50 m, tapering out southwards within the shales of the Lunner Fm. (Owen et al., 1990).

The Kjørrven Fm. comprises beds of limestone and calcareous siltstone up to 20 cm thick with a varying thickness of alternating silty shales between 16- and 60 cm. The limestone horizons become more common towards the top of the formation, and the total thickness is about 100 m (Owen et al., 1990). It is not found in the northernmost parts of the mid-Ordovician and Silurian successions at Hadeland.

The Lunner Fm. is a shale dominated unit with a thickness up to 200 m with thinning towards the northwest. Siltstone horizons occur at various levels, and nodular bedded limestones can be found in the lowest and uppermost parts but are rare to find in the southeastern parts of the formation. These two nodular limestone beds are called the Gagnum Member and the Grinda member, respectively (Owen et al., 1990).

The Kalvsjøen Formation

The Kalvsjøen Fm. (Figure 2.8) is mainly composed of nodular and bedded bioclastic limestones alternating with thin shales. Local accumulations of carbonate blocks up to 20 m thick can also be found locally. The formation thickens from about 60- to 80 m southwards, and overlies the Kjørrven Fm. in the south, the Lunner Fm. in the central parts and the Gamme Fm. in north Hadeland (Owen et al., 1990).

Figure 2.8: Nodular bedded limestone with thin alternating shales in the Kalvsjøen Formation. Beds are ranging between 8 and 20 cm in thickness. Loc: 60.3113056, 10.3868495.

The Skøyen Group (the Klinkenberg Formation and the Sælabonn Formation)

The Skøyen Gr. is a sandstone- and shale dominated unit that first was suggested to be defined as the Skøyen Sandstone Unit by Owen (1978) with a gradational base and top to the Kalvsjøen Fm. and the Rytteråker Fm. When the succession was revised by Worsley et al. (1983), it was found that the upper part correlates with the shale rich Sælabonn Fm. from Ringerike. The lower parts have by later publications been assigned as the sand-dominated Klinkenberg Fm., which is lithological variable with an important change in sedimentological development in Late Ordovician (Worsley et al., 1983). This glaciation can be seen as an unconformity between the Sælabonn- and Klinkenberg Fm., which both possess a high degree of consolidation. The total thickness of the Skøyen Gr. is assumed to be close to 200 m (NGU, 2021b). At Buhammeren, however, its thickness is closer to 80 m (R. Knarud, personal communication, August 10, 2021). It extends into the lowest Silurian (Owen et al., 1990).

The Rytteråker Formation

Earlier called the "Penramerus Limestone", the Rytteråker Fm. (Figure 2.9) is a limestone unit with an approximate thickness of 50 m. The basal stratotype displays a gradational development, with interbedded thin to medium siltstones and shales immediately overlying the Sælabonn Fm. at the base. It has increasing amounts of limestone beds upwards; described as a shallowing upward sequence of approximately 10 meter in thickness. The limestones consist of rock forming pentamerids and grade upwards with thickly bedded biosparites. The uppermost part of the formation has an increasing content of shale towards the contact with the overlying Vik Fm. (Worsley et al., 1983).

Figure 2.9: Example of "Pentamerus Limestone" with pentmerids and crinoids in the Rytteråker Formation. Loc.: 60.3370631, 10.4462499.

The Vik Formation

The Vik Fm. (Figure 2.10) is widespread but discontinuously exposed in the Ringerike district. It is around 80 m thick, and shows a tripartite development with varying portions of red, greenish and gray shales, marls and limestones (Worsley et al., 1983). At Hadeland, the description of shales in some locations overall corresponds better with the Vik Fm. described at Ringerike and is, therefore, also included in this thesis at Hadeland, as well as in the 1:50 000 bedrock map (Figure 5.1).

Figure 2.10: The Vik Formation with distinct red colored shales. Loc.: 60.3322834, 10.4362634.

The Ek Formation

The Ek Fm. (Figure 2.11) is dominated by greenish- to dark grey shales, often graptolitiferous. It is approximately 95 m thick, and from Hadeland to Ringerike there is a transitional development to the Vik Fm. A satisfactory definition of the formation is found difficult to come up with due to poor exposure and complex tectonics (Worsley et al., 1983).

Figure 2.11: Shales in the Ek Formation. Loc.: 60.3339849, 10.4418082.

The Bruflat Formation

The Bruflat Fm. has no single type section because of incomplete exposure and complex tectonics, but a thickness of 400- to 550 m is suggested. At Hadeland, approximately 125 m of the formation is exposed, but neither the top nor bottom of the unit is preserved. The formation composes varying proportions of sandstones, siltstones and silty shales with large internal variations. Many sandstone layers have erosive bases, and the lower parts consists of medium to thickly bedded very fine calcareous sandstones and silty shales. The base is defined by the first occurrence of sandstone (Worsley et al., 1983). Recent road work south of Jevnaker exposes the Bruflat Fm. and enables for new studies on facies and thickness of the formation at Hadeland, but this is not carried out in this thesis.

3 Theoretical background

This chapter presents some theoretical background and terminology relevant for further reading in structural elements, LiDAR data and U-Pb dating of calcites.

3.1 Structural elements – some basic terminology

3.1.1 Thin-skinned foreland basins

Foreland basins develop in the front of active thrust belts. The direction of tectonic transport is towards the evolving basin, and because the thrust load is inherently mobile, the foreland basin itself becomes involved in the deformation process (Johnson et al., 1986). Thin-skinned tectonics (Figure 3.1) are related to thrust sheets where the sedimentary cover is detached from its crystalline substratum along a detachment layer that consists of mechanically weak rocks. The thickness of cover sediments is often in the order of 1 to 10 km (Pfiffner, 2017).

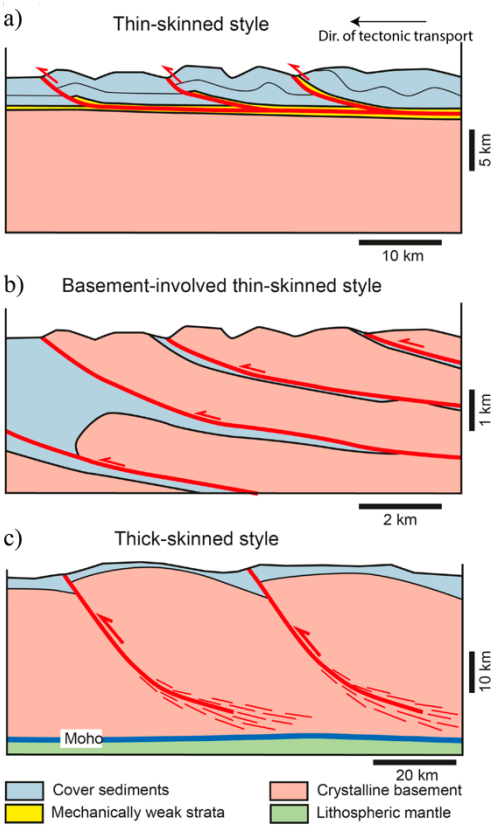

Figure 3.1: Schematic cross-sections showing the basic styles of thin- and thick-skinned tectonics. (a) Thin-skinned style (relevant for this thesis). (b) Basement-involved thin-skinned and (c) Thick-skinned style. Modified after Pfiffner (2017).

3.1.2 Folds

A fold is a bend due to deformation of the original shape to a surface, and a syncline is a fold that concaves upward with the younger beds in the center. Folds are characterized by a set of domains, and their structural style is controlled by the mechanical stratigraphy as well as by the direction of applied forces (Groshong Jr, 2006). They can be classified after Ramsay (1967) based on dip isogons and based on interlimb angles after Fleuty (1964). These, in addition to common terminology, can be seen in Figure 3.2.

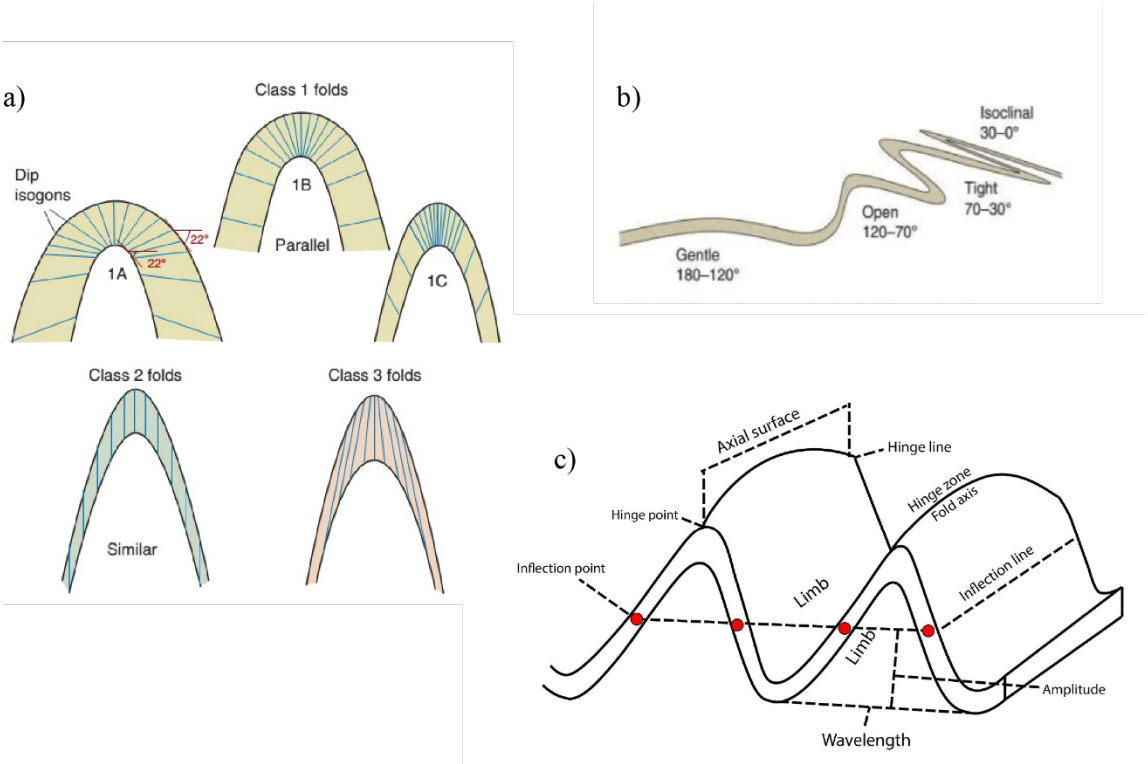

Figure 3.2: Fold classifications and terminology. (a) Classification based on dip isogons after Ramsay (1967). (b) Classification based on interlimb angles after Fleuty (1964). (c) Commonly used terminology for description of folds. a) and b) from Fossen (2016), c) modified from Fung (2016).

3.1.3 Faults

A fault can be defined as a surface or zone where there has been relative displacement between the two sides parallel to the zone (Bates and Jackson, 1987). Displacement is the relative movement of the two sides to a fault and can be measured in any direction. A normal fault has the hangingwall displaced down with respect to the footwall, common in extensional regimes. Reverse fault is used to describe a fault where the hangingwall moves up with respect to the footwall, more common in compressional regimes (see example in Figure 3.3).

In geological terminology, a thrust fault is a low angle reverse fault, but they can also be steeply dipping due to folding or rotation caused by imbrication. Thrust faults cut up section in the direction of tectonic transport in a thin-skinned foreland basin and are used as the main terminology for faults in this thesis. Second- and third order thrusts are the dominating orders of thrusts in a thrust sheet, and they can dip up to 60 degrees in the top while flattening out closer to the underlying detachment horizon. Second order thrusts branch of first order thrusts (largest thrusts and detachments), and have displacement in tens of meters with strike up to 3 km, while third order thrusts have displacement of less than ten meters and strike lengths less

than 500 m (Morley, 1983). They can be fore- or hinterland verging in regard to the regional tectonic direction of transport, referred to as forethrusts or backthrusts.

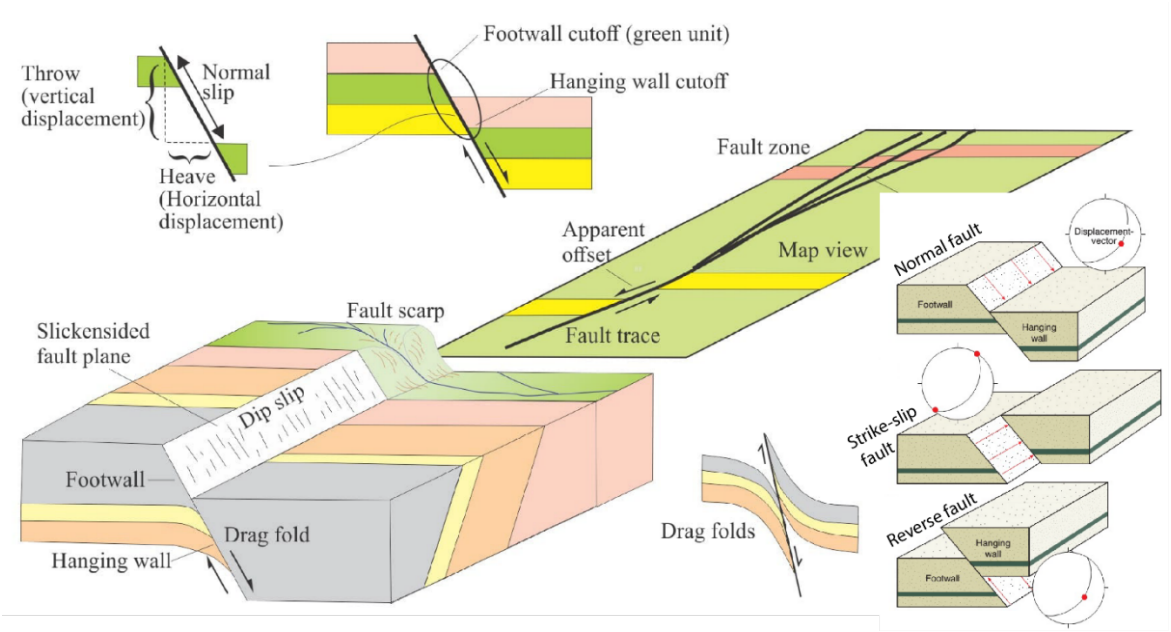

Figure 3.3: Terminology for faults composed of illustrations modified from Ricketts (2021) and Fossen (2016).

3.2 LiDAR data and its use in geological mapping

3.2.1 What is LiDAR?

LiDAR (Light Detection and Ranging) data is a technology used to produce high-resolution digital elevation models of the ground with a vertical accuracy up to 10 cm. The data used in this study is collected as point clouds from laser scanning with an airplane flying over an area, but terrestrial laser scanners and other techniques can also be applied for geological outcrops (Buckley et al., 2013). A platform with known position and altitude, determined from a GPS, acquires the distance from the sensor to the ground in a series of points measured approximately perpendicular to the direction of flight, as seen in Figure 3.4 (Dowman, 2004). Because the scanners can record

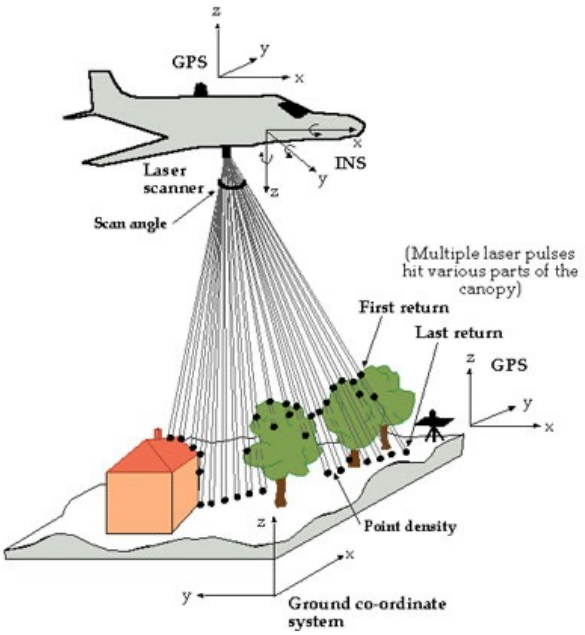

Figure 3.4: Schematic illustration of how LiDAR data can be collected. From Dowman (2004).

multiple different returns, a pulse or return from for example trees or buildings will be recorded as first returns. In this way, the bedrock of an area can be exposed by removing early returns, revealing structures that normally are covered with for example soil, acers, or infrastructure.

The most widespread application of airborne collected LiDAR data for geoscientists is to document coastal changes and mapping of geomorphic features like landslides, alluvial fans, stream channels and fault scarps (Pavlis and Bruhn, 2011). A Digital Terrain Model (DTM) can be used to produce hillshade images, which is an artificial shade produced by a sun source placed at a desired azimuth and altitude. Azimuth is the cardinal direction from where the artificial light is shining (between 0 and 360 degrees), and altitude is the "height" of the "sun" (artificial light) (from 0 to 90 degrees). N-S oriented structures will create the best shading and be most easily identified with an azimuth of 90 or 180 degrees, while perfectly E-W oriented structures will create no or poorly visible shade from this azimuth. Figure 3.5a shows the effect of changing the azimuth, and Figure 3.5b shows how the bedrock can be exposed in different altitudes.

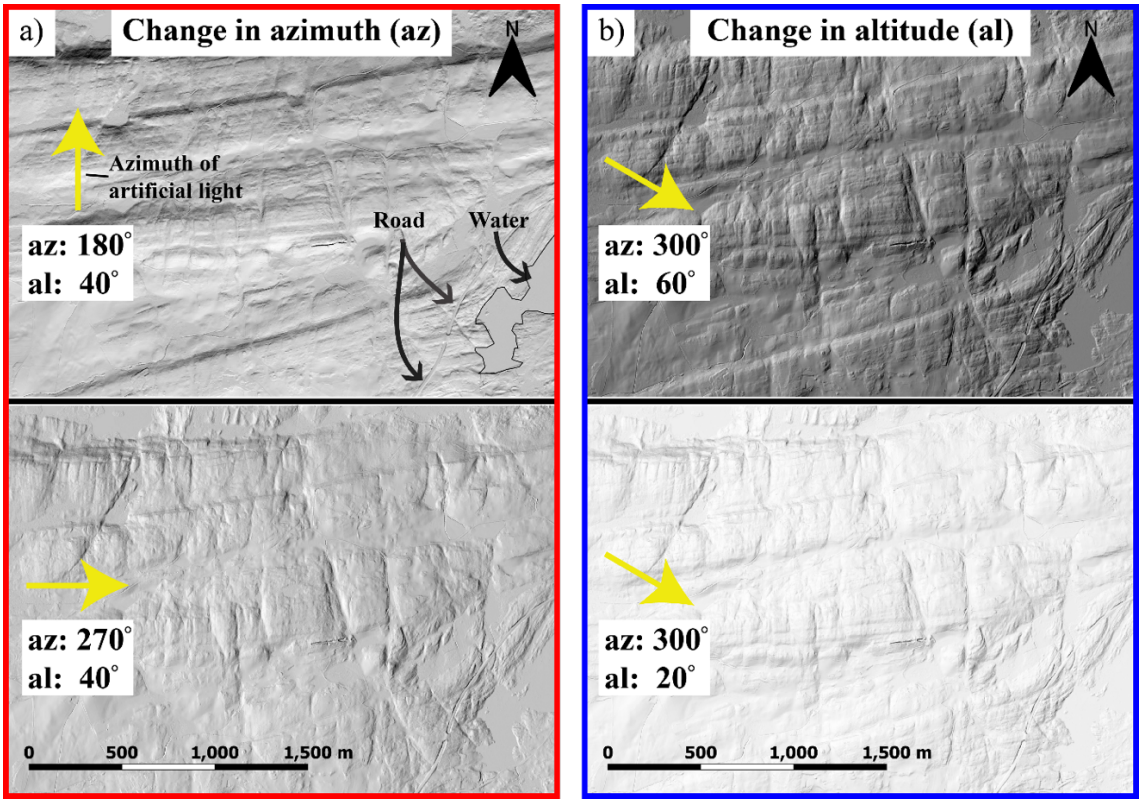

Figure 3.5: Same area (in all four pictures) with change in different parameters of LiDAR hillshade images. (a) Change in azimuth from 180 degrees (top) to 270 degrees (bottom). Arrows points at examples of how roads and water are displayed on hillshade images. (b) Change in altitude from 60 degrees (top) to 20 degrees (bottom).

3.2.2 LiDAR data in geological bedrock mapping

Large scale landforms as end moraines and drumlins show up clearly in LiDAR DTM, as well as mesoscale landforms that are smaller than the resolution of topographic maps. Johnson et al. (2015) concluded that in general, LiDAR DTMs provide for a less expensive, quicker, and higher quality mapping of Quaternary maps. The Geological Survey of Norway (NGU) have estimated that their basic Quaternary maps at the scale of 1:50 000 now are of a quality corresponding to 1:35 000, while the time of mapping is reduced between with 20-40 % compared to pre LiDAR mapping (Johnson et al., 2015). In another paper by Pavlis and Bruhn (2011), the application of LiDAR-derived topography to delineate bedrock structure in a poorly exposed area was tested. It was concluded that LiDAR data has a significant potential to map out structural geology and geomorphology, and when combined with computer graphic software and real time GPS recording on a field computer, LiDAR data sets can be used to map out faults, folds, and bedding. They note that in areas where bedrock exposure is poor, their suggested workflow on how to implement LiDAR data should yield major new insights for future field studies. This strengthens the credibility of the LiDAR data to be used and leading in the update of the existing Gran 1:50 000 map in this study, even when the area and geology in the two studies does not compare. As with Johnson et al. (2015), Pavlis and Bruhn (2011) note that the use of LiDAR data to analyze bedrock structures is an application that has not previously been appreciated to their knowledge.

3.3 U-Pb dating of calcite

Absolute dating of carbonate minerals, calcites in particular, is performed using Laser Ablation Inductively Coupled Plasma Mass Spectrometry (LA-ICP-MS) U-Pb (Uranium-Lead) geochronology. This is a dating method that rapidly gains popularity over traditional isotope dilution methods (Roberts et al., 2020). Direct dating of calcite utilizing the U-Pb relations is a vital tool to constrain the timing of processes such as fault activity and hydrothermal mineralization (e.g. Roberts and Walker, 2016; Nuriel et al., 2017; Drost et al., 2018) making it particularly suitable for dating of precipitated calcite in the Hadeland area.

As with all dating methods, U-Pb dating carries a set of limitations. The locating of zones with sufficiently high U concentrations can be time-consuming and a “hit or miss” procedure. Low U concentrations and/or high amounts of initial Pb in addition to presence of different generations of carbonate minerals and local open system behavior of the U-Pb system often

obstruct extraction of a reliable age information. Prerequisites that are important for a successful U-Pb dating of carbonates are a closed isotopic system, a homogeneous and initial "common" Pb composition, and a sufficient spread in the parent/daughter ratio (Rasbury and Cole, 2009). A perfect U–Pb chronometer demands the incorporation of U (parent isotopes ^{238}U and ^{235}U decay to ^{206}Pb and ^{207}Pb respectively) as well as zero or low concentrations of initial Pb during its formation. This is often expressed as the ratio of parent uranium to initial Pb – $^{238}U/^{204}Pb$ or μ. Ideally, the parent and daughter isotopes remain in a closed system from formation until dating (Roberts et al., 2020). Strategies, progress and limitations of the method is discussed in detail by Roberts et al. (2020), and Drost et al. (2018) goes in detail for the approach similar to the one used in this thesis to extract ages of the sampled calcites.

4 Data and methods

This chapter describes collection of data and the method used to produce the results in this thesis.

4.1 Field work

In order to update and improve the already existing map at Hadeland, focusing on the central and southern parts, a field campaign was carried out between the 8th and 24th of August 2021. The field work had two main purposes; determine and collect strike/dip measurements covering the area and collect samples of calcite for U-Pb dating. In addition, general structural observations and notes on the different lithological units were taken. After the fieldtrip, preparation and sending of the calcite samples was carried out, before the collected data was imported and compared to earlier bedrock map and LiDAR- data in the area using *QGIS 3.16.11- Hannover* (QGIS.org, 2021) (see also Figure 4.1).

4.1.1 Mapping equipment

To achieve field efficiency and higher measurement accuracy, the application *Fieldmove Clino* by Petroleum Experts Limited (version 2.5.0) on an iPhone 10s was used. *Fieldmove Clino* is a digital compass- clinometer designed for simplifying and structuring field work. It allows for large amounts of measurements, improving the statistical validity of the data, and is the most common software among field researchers today (Bubniak et al., 2020). Multiple recent articles have tested the accuracy and validity of *Fieldmove Clino* as a replacement for traditional compass, e.g., Novakova and Pavlis (2017); Novakova and Pavlis (2019); Bubniak et al. (2020); Wang et al. (2020). Their general conclusion is that the application works best on an iOS device, and if tested and compared to a traditional compass before and regularly while in use, it provides a reliable alternative for the traditional compass. Thus, a Silva Compass Expedition S was frequently used in this study as a confirmation on the results from the application, never displaying significant deviations. The application also allows for georeferenced digital photographs and text notes to be taken in the same project. This makes the process of connecting measurements and field observations in a large area and short amount of time possible when processing the data. Declination was set to 4.0° and the angle convention was set to dip/strike, using the right- hand rule (RHR).

Another application, *Avenza Maps* (version 3.14.1), was used during field work allowing for GPS- oriented positioning on a beforehand imported TIFF- file of the LiDAR data and a SHAPE- file of the lithological boundaries of the already existing geological bedrock map of *GRAN 18151, M 1:50.000* (Owen et al., 2001). Tracking of position in relation to the LiDAR- and existing bedrock map while taking measurements and observations functions as a support if confusion and uncertainty appears, and either the lithological unit or orientation of the structures doesn't add up with immediate in- field interpretations. It is important to note that it should not affect nor implement the final observations conducted, but rather help to avoid severe misinterpretations due to the comprehensive division of lithological units.

Plotting of field data

All stereoplots in this thesis are created in *Stereonet* by Allmendinger (2021). Scientific algorithms in the program are described in Allmendinger et al. (2011) and Cardozo and Allmendinger (2013).

4.1.2 Workflow in field and processing

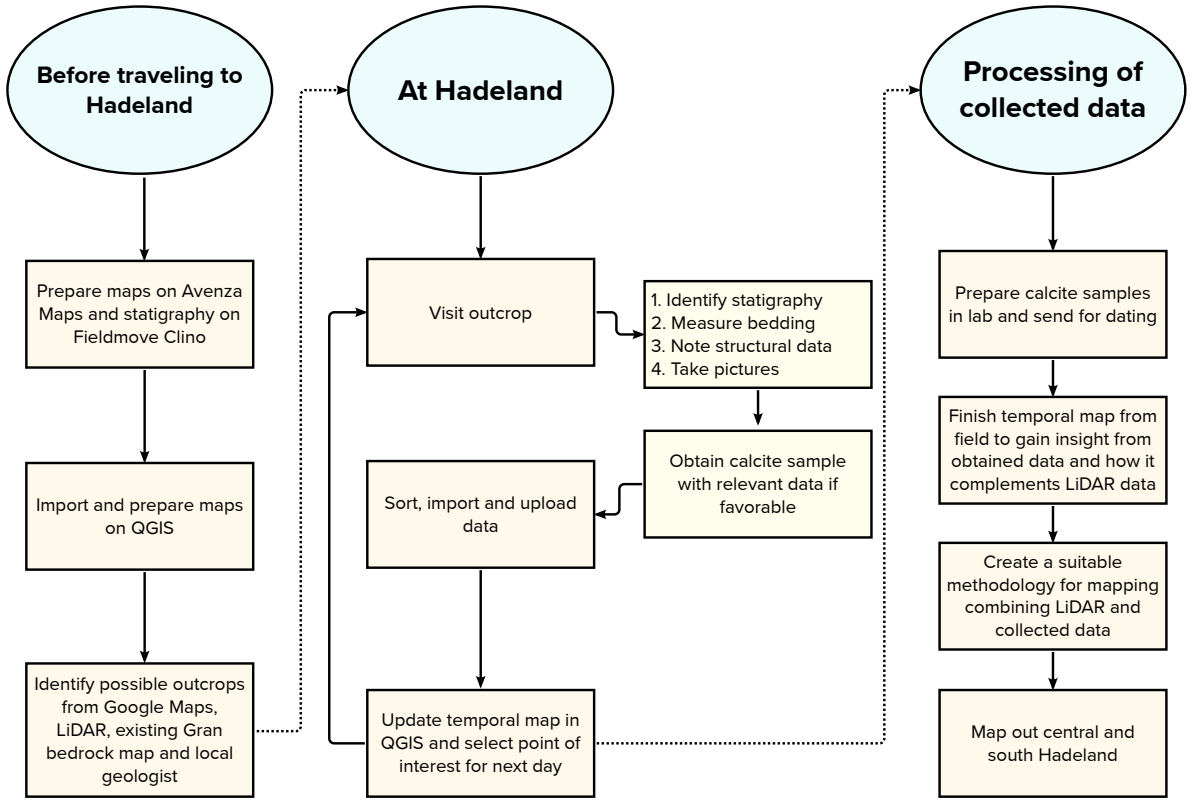

Figure 4.1: Workflow used to obtain data from the field and further processing of collected data.

4.1.3 Bedding and lithology

Obtaining measurements of bedding as well as identifying the lithology of exposed outcrops were one of the main purposes with the field trip. It was desirable to cover a large area to have a great number of measurements to compare with the LiDAR data. At Hadeland, the exposed outcrops often have peculiar features; outcrop quality, bedding direction and lithological characteristics varies greatly. Therefore, confidence levels for both strike/dip measurements and identified lithological units were rated on a scale from one to four, where a higher number represents a higher level of confidence. High level confidence measurements should be used to a greater extent than low confidence measurements if contradicting each other when mapping out the area. A 30 % hydrochloric acid was used to identify carbonate rich rocks, and in areas where the beds were turned into nearly vertical positions, both sedimentological criteria and structural understanding were used to determine the right stratigraphic way up.

4.2 Mapping with LiDAR and GIS

LiDAR data used in this study is provided by Kartverket (2015), and the Digital Terrain Model (DTM) is downloaded from hoydedata.no as LAZ files in the UTM zone 32N projection. Data covering the study area is mostly from the year 2007, with some supplying collections from 2010 and 2015. The resolution of the data is 1 m. These files were imported to *QGIS*, where layers of hillshades with different azimuth and altitude were produced using the plugin "Batch Hillshader".

The existing bedrock map in the area was downloaded from NGU (2021a) as shapefiles in CRS UTM zone 32N projection. The data includes lithology both as polygons and boundaries only, as well as faults and strike/dip measurements. Field data that was collected on the *FieldMove Clino* app was imported to *QGIS* and transformed from .kmz file to .shp file and further sorted in different groups based on type of information. This made mapping of central and south Hadeland with a combination of existing map, LiDAR data and self-obtained field data possible.

An azimuth of 300 degrees and altitude of 40 or 60 were mainly used while mapping. This was found to be the most efficient hillshade combination to use on the geology at Hadeland due to its notable E-W trending structures. When mapping out N-S oriented lineaments, azimuth of 90 and 270 degrees were used.

4.2.1 Terms for this thesis

"Packages"

The expression "package" in this thesis refers to a well-defined and seemingly coherent and laterally continuous geological unit exposed on the hillshade images, see examples from Figure 4.2. In the study area, the packages have a general E-W orientation and vary in apparent thickness (measured from map view) up to 700 m. Most of the packages terminate in the Randsfjord with soils and bedrock coverage in the west. To the east, their prevalence also gradually becomes less distinct.

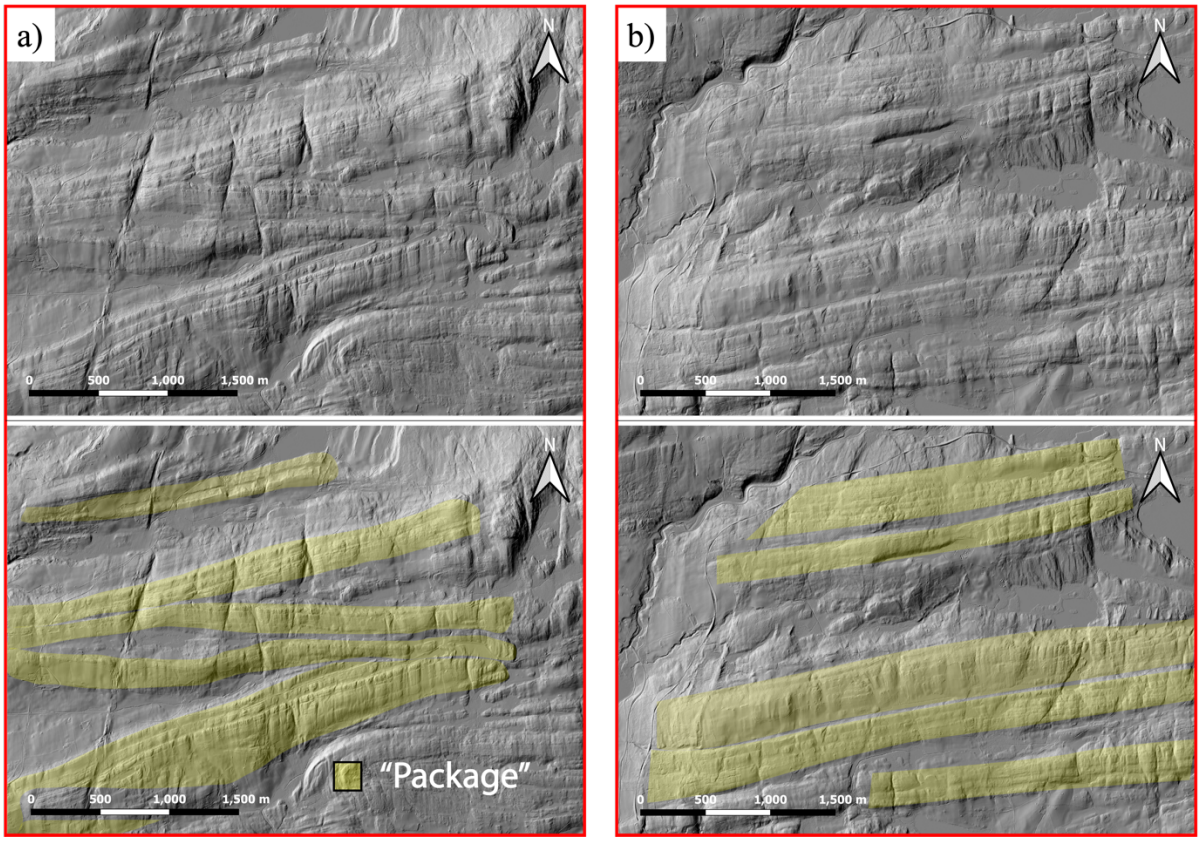

Figure 4.2: Example displaying how packages emerge on the hillshade images from LiDAR data in two separate areas from the study area. (a) and (b): top picture is only hillshade images with azimuth of 300 degrees and altitude of 60 degrees. Lower pictures are corresponding areas but with structures that can be defined as "packages" outlined in yellow.

Fault zones

Fault zones are lithological heterogenous and structurally anisotropic discontinuities in the upper crust with distinct components like a fault core and an associated damage zone. Fault cores accommodate most of the displacement, while the damage zone is mechanically related to the growth of the fault zone (Caine et al., 1996; Childs et al., 1997). They vary in size and architecture. In this paper, fault zones are used for greater areas that surround the exact trace of a fault from traditional geological maps. In fault zones, the LiDAR data displays a chaotic or

plane pattern, often between packages, resulting in final positioning of the faults to be difficult to determine, see example in Figure 4.3. Fault zones are always determined in a combination of field measurements and LiDAR data, and not every fault is situated in fault zones that are visible on the scale of mapping. The final and exact trace of a fault cannot be determined in all cases at the current level of mapping, but the implementation of fault zones ensures that areas affected by faulting are outlined, and a final line to indicate the position of a fault can further be inferred for a final geological map.

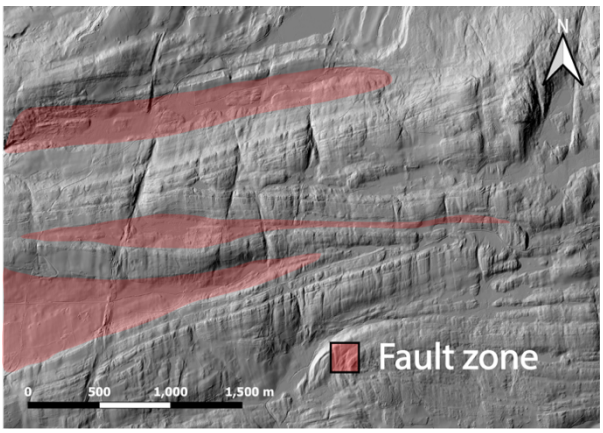

Figure 4.3: Example of area where fault zones can be interoperated solely on LiDAR data and with no field observations. Note that this is not the final map, but only an example of how fault zones can emerge on the hillshade map between "packages" (see Figure 4.2).

4.3 Cross-section

4.3.1 Construction

The first step in the construction of the main cross-section of central and south Hadeland was to select the placement of the section line which should not deviate more than five degrees form the main tectonic transport direction in the area (Woodward et al., 1989). The selected section line was placed on top of the polygons in the new map from this thesis in *QGIS*, and the plugin "qProf" was used. This plugin creates the framework for the cross-section with the topographic profile using the DTM and the position of layer boundaries between the geological units interpreted on the new map are highlighted. Also, bedding from the field is included using the strike and dip of the points imported to *QGIS*. These tools both simplify the process and improve the quality of the final result. No vertical exaggeration was used.

When drawing detailed cross-sections on these scales, local strike and dip measurements obtained in the field must be combined in a reasonable way to best determine the bedding for the different structures on a larger scale. In this study, averages from bedding data within the same package were calculated, and high level confidence measurements (see chapter 4.1.3) were prioritized. If the general strike was deviating more than five degrees from the bearing of the section line, the apparent dip was calculated (Equation 4.1). Due to the placement of the section line, few areas of the profile had no bedding measurements, but, if needed, the geometry

and dip were interpreted to be as geologically reasonable with surrounding structures as possible.

$$tan(\alpha_{apparent\ dip}) = tan(\alpha_{true\ dip})\ x\ sin\ (\alpha_{strike\ measurement} - \alpha_{section\ line})$$

Equation 4.1: Equation to calculate apparent dip if strike was deviating more than five degrees from bearing of section line. α = angle. Found in e.g., Gabriel and Miller (1952).

Progressive deformation structures in thin-skinned foreland basins are often complex, and without seismic data and detailed thickness measurements on formations found in the area, the depth to the postulated upper detachment from Morley (1983) was not calculated.

4.3.2 Calculation of shortening

To estimate total shortening of the mid-Ordovician and Silurian succession, the sinuous- bed method described by Woodward et al. (1989) was utilized. If bed lengths are properly portrayed in a cross-section, the cutoffs will match up when unfolded and unfaulted, and extend into the original and undeformed stratigraphic wedge. Originally, defined by Dahlstrom (1969), sinuous- bed balancing requires a consistency of bed length in the restored thrust sheet. Eroded parts of the layer have to be interpreted with rational variations (see Figure 4.4) (Woodward et al., 1989).

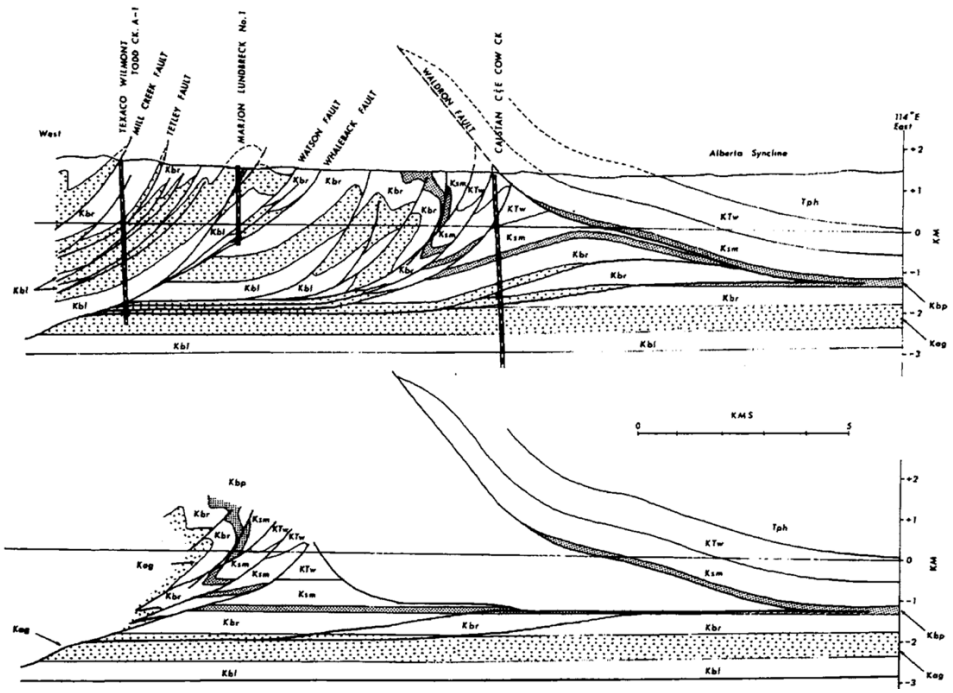

Figure 4.4: Illustration of sinuous- bed length restoration. The most important criteria when drawing a restorable section is that the interpreted eroded shapes of the hanging wall match with the measurable shapes of the footwall seen at surface. In this figure, the dark layer has been used as key bed. From Woodward et al. (1989).

In thrust terrains, as in the case of this study, large portions of the synorogenic sediment are deposited on an already shortened strata. Only pre- orogenic sediments will be fully restorable, and syn- orogenic sediments will usually be shorter than the restored length of pre- orogenic sediments (De Paor and Anastasio, 1987; Woodward et al., 1989).

Having the section drawn in *Adobe Illustrator* enabled for precise measurements for estimations in this thesis. The total shortening (e) was found by using the calculated original length (L_0) of the chosen key layer and the length of the same layer with present deformation (L_1) using Equation 4.2.

$$e = (L_0 - L_1)/L_0$$

Equation 4.2: Equation used to calculate total shortening (e). L_0 = original length and L_1 = present length of key layer. Found in e.g. Morley (1986).

Assumptions needed to balance the section are:

1. Transport direction is parallel to cross-section.
2. Strain compatibility: no holes or cavities before or after deformation in the section.
3. Plane strain: all motion has been parallel to the cross-section and there has been no change in volume.

4.4 U-Pb dating of calcite

4.4.1 Sampling in the field

In order to temporally constrain deformation and fluid events of Caledonian contractional structures, as well as Permian extensional structures, U-Pb dating of calcite mineralization in faults and veins from the Hadeland area were conducted. The amount of calcite precipitation in the area is relatively low, and the number of calcite samples collected and prepared for dating was limited due to economical and temporal reasons. Observed minerals thought to contain datable calcite thus had to be selected with care, and a priority list was made (Table 4.1) where calcites with slickensides oriented N-S or E-W were prioritized. Acquiring samples from different geographical locations within the studied area was also targeted, allowing the possibility of comparison of results within the area. The same applies for samples with origin in different lithological units, but neither of these should confine nor restrict the sample quality due to low rate of calcite precipitation.

Table 4.1: List of prioritization for calcite samples found in the field. Level 1 is of highest interest while level 4 is of least interest.

Level of prioritization	Slickenside indicating relative movement on, or in immediate proximity of the calcite	N-S or E-W oriented structure
1	YES	YES
2	YES	NO
3	NO	YES
4	NO	NO

Each sample was orientated by compass (*FieldMove Clino*), and all relevant information was noted before coordinate- fixed and cardinal- oriented pictures were taken at different scales. Relevant information includes sample name, strike/dip (RHR) with marker symbol on sample, slickensides (plunge/azimuth), host rock type, host rock age and other relevant comments like probable local field of stress and slip movement. This information may assist when making decisions while dating the samples and can be crucial for discussing and interpreting the end results. A total of 29 samples were collected between 8th and 24th of August mainly in central and south Hadeland. Six samples were from north Hadeland to compare age between the shales and the more competent sand- and limestones, as well as geographical distribution (positions seen in Figure 4.5 and coordinates in Appendix A).

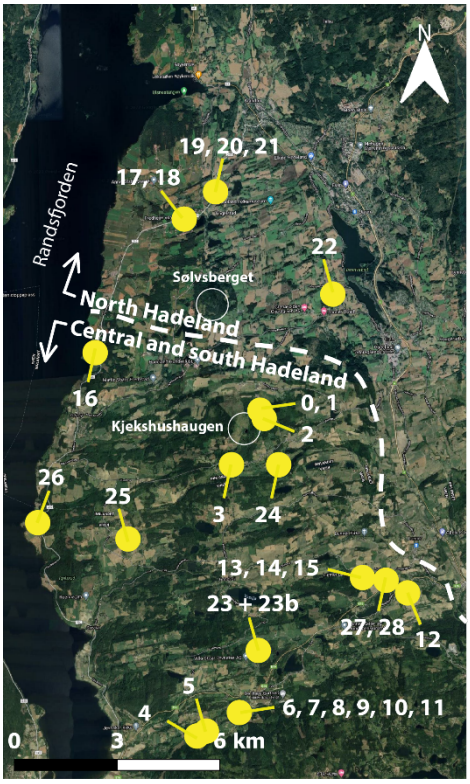

Figure 4.5: Overview of positions for collected calcite samples.

4.4.2 Lab and mount preparation

The collected samples were closely studied before cutting took place. Some of the samples had calcite participated as few µm to mm thick surface layers, while others consisted of veins and coarser crystals. To allow for analyzation for both rim- core zonation and on the slickensides located on the surface, some of the samples were divided into two separate mounts (a and b).

Cutting was conducted using a diamond saw and should be as straight as possible to provide for an even exposure contact on polished mount.

After cutting, the samples were placed in round mount blocks with a diameter of 25 mm. Epoxy were slowly mixed in a relation of 2.5 to 1 with spesifix- resin and spesifix- hardener, respectively. The mixture was carefully poured in the mounts, and solidification time is 12 hours in room temperature.

Each sample was taken out of the mount upon solidification and prepared for polishing. All remaining epoxy was grinded away between the surface and the sample using MD Piano #220 diamond naps with water for cooling. Samples with a limited amount of calcite were grinded by hand using #220 and #1000 grit sandpaper to better control the level of calcite exposure. Polishing was performed in a Struers Tegramin-30 at four different levels: 9, 3, 1 and 0.25 µm, with water- based diamond suspension as polishing agent. Before the analysis, the samples were screened to detect suitable areas for further investigation.

A total of 34 mounts were sent for analysis, with 20 being selected as high priority and the remaining 14 as backup samples if the prioritized samples turned out to not be suitable for further analyses due to lack of U or unfavorable U/Pb relations.

4.4.3 Dating

The dating was done in collaboration with Trinity College Dublin at the Geology Department by Dr. Kerstin Drost. Data processing and analyzing of the prepared mounts is a comprehensive procedure which will not be explained in detail in this study. For a full account of the method, Drost et al. (2018) and Roberts et al. (2020) should be consulted, as well as information on analytic setup and operation conditions in Appendix A.

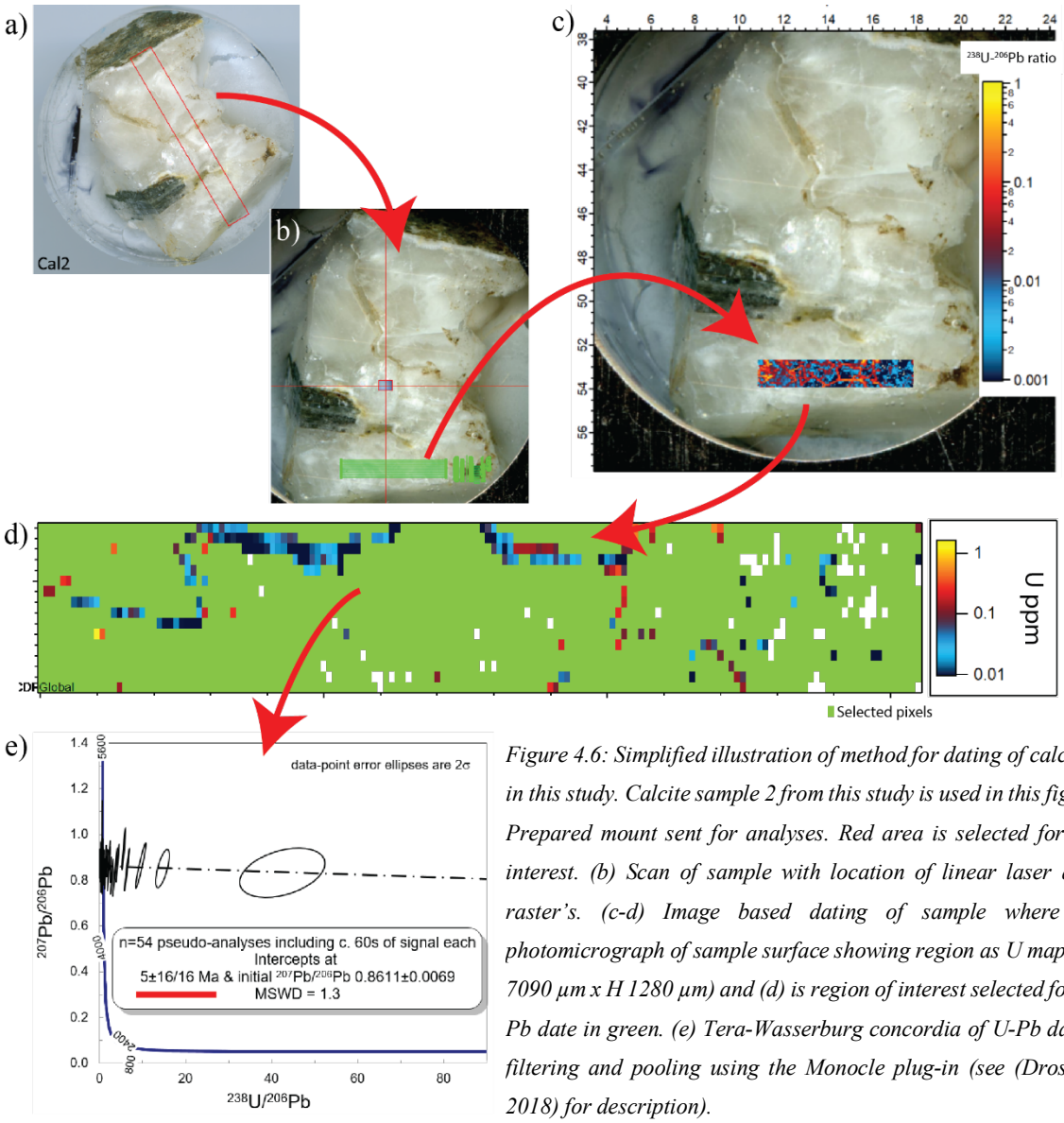

Figure 4.6: Simplified illustration of method for dating of calcite used in this study. Calcite sample 2 from this study is used in this figure. (a) Prepared mount sent for analyses. Red area is selected for special interest. (b) Scan of sample with location of linear laser ablation raster's. (c-d) Image based dating of sample where (c) is photomicrograph of sample surface showing region as U map (size W 7090 µm x H 1280 µm) and (d) is region of interest selected for the U-Pb date in green. (e) Tera-Wasserburg concordia of U-Pb data after filtering and pooling using the Monocle plug-in (see (Drost et al., 2018) for description).

After dating as illustrated in Figure 4.6 is completed, three different "age" calculation are presented for each sample: Lower Intercept Age, Isochron Age and 86-TW Intercept. In this thesis, the Lower Intercept Age (underlined with red in Figure 4.6e) is the primary age used for further discussions of the results.

5 Results

The results from this study are divided into three subchapters. First, the results and observations of LiDAR data and its use for bedrock mapping in the area are introduced, and how LiDAR hillshade images can influence the mapping of Hadeland. After this, the main structures of the area, both on a large scale from the map and cross-section, and on a smaller outcrop scale are presented. Last, the results from the attempted U-Pb calcite dating of Caledonian compression and Permian extension are presented.

The structural geology at Hadeland possesses a variety of different elements, both in structures and lithology. Field observations of deformation structures reflects the main components of the mapping scale, and the lithological units are influenced by a variety of stress regimes, resulting in faults and folds in order accommodate shortening of the area. In this thesis, preliminary analysis of the E-W related structures is interpreted to be related to the Caledonian orogeny, while N-S structures are primarily thought to be related to the later Permian extension. This is based on the many publications and studies carried out in the Oslo Region prior to this study (e.g. Størmer, 1943; Roberts and Sturt, 1980; Morley, 1983; Bruton et al., 2010; Sippel et al., 2010).

5.1 LiDAR and bedrock mapping

Due to the relatively few exposed outcrops at Hadeland, LiDAR data was used to improve the mapping of central and south Hadeland in the already existing *GRAN 18151, M 1:50.000* bedrock map from Owen et al. (2001). This subchapter presents the resulting map from this study with cross-section and balancing, and a comparison with the existing map.

5.1.1 New and existing map

A comparison of the map created in this study and the existing bedrock map (Owen et al., 2001) (hereby referred to as “existing map”) can be seen in Figure 5.1. As opposed to a finished and official bedrock map, these maps are presented with their lithological boundaries overlain on the in the LiDAR-based hillshaded terrain model. The two maps correspond fairly well when looking at the main structures and overall trends between the lithological units. Large scale folding and thrust faults are dominating the general geological expression in the area, but N-S oriented intrusions and lineaments can also be identified from the LiDAR data.

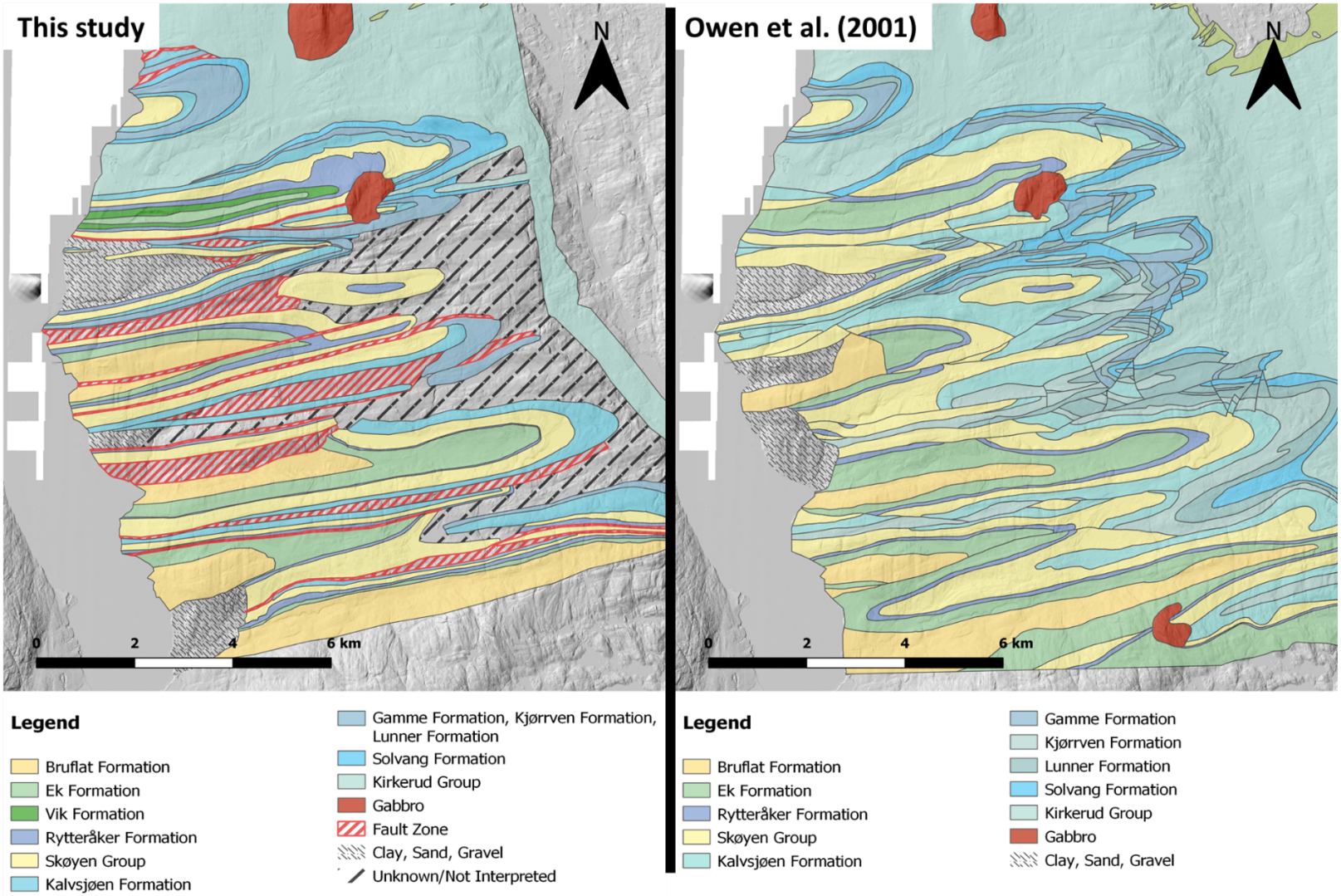

Figure 5.1: Comparison of formations in map from this study and existing map from Owen et al. (2001) covering the mid-Ordovician and Silurian successions of central and south Hadeland. Associated legends are used for all maps in thesis.

The legends for the two maps have some notable differences. While the existing map distinguishes between the Gamme- Kjørrven and Lunner Fm., the map from this thesis has included these as one stratigraphic unit. The Gamme- and Kjørrven Fm. are two limestone dominated units which at Hadeland are not continuous from the northern to the southern parts in the mid-Ordovician to Silurian succession (Owen et al., 1990). They are stratigraphically situated next to the more shale dominated Lunner Fm., which in the lower and uppermost parts includes nodular and gradually increasing amounts of bedded limestone horizons. Utilizing LiDAR data and focusing on the structural geology, it was found favorable to include these as one unit as they are found to not differ mechanically and are difficult to divide without excessive paleontological knowledge on the formations. Another difference is the introduction of the Vik Fm. in this study, which was observed with a distinct red color (see Figure 2.10). The legends "Fault Zone" and "Unknown/Not Interpreted" are also exclusive for the map from this thesis.

The most notable difference between the two maps is that the map from this thesis is more refined with higher layer continuity in the E-W direction and an overall more dominating E-W trend with few to no N-S oriented cutoffs or formation disruptions. Unknown/Not Interpreted are used whenever few or no measurements can be traced with a certain level of confidence, or if multiple measurements within stratigraphic units with kindred properties contradict each other. In the eastern most parts of the area, the existing map is cluttered with different units from the Solvang Fm. and up to the Lunner Fm. Few outcrops were found in the area, and LiDAR hillshade images does not provide traceable shades to determine the position for unit boundaries alone, resulting in the decision to not interpret the area in order to strengthen the credibility of the interpreted areas on the remaining parts of the map.

Table 5.1: Comparison of overlap between the map from this study and existing map (Owen et al., 2001) for central and southern parts of Hadeland. Colors are correlated to the values for each column: Red = no overlap (0 %), Yellow = intermediate (0.01 – 10 %) and Green = most overlapping formations (>10 %). Corresponding formations are highlighted diagonally. G/K/L Fm. = Gamme/Lunner/Kjørrven Formation. (a) Numbers in km^2. (b) Numbers in percentage with respect to map from this study.

a) **Overlap between formations in km^2**

Existing map (Owen et al., 2001) \ Map from this study	Gabbro	Bruflat Fm.	Vik/Ek Fm.	Rytteråker Fm.	Skøyen Gr.	Kalvsjøen Fm.	G/K/L Fm.	Solvang Fm.	Kirkerud Gr.	clay/sand/ gravel	Fault zone	Unknown/not interpreted	Total
Gabbro	0,59	0,00	0,00	0,03	0,04	0,01	0,00	0,01	0,00	0,00	0,00	0,00	0,69
Bruflat Fm.	0,00	5,65	1,17	0,21	0,12	0,00	0,00	0,00	0,00	0,63	0,08	0,00	7,86
Vik/Ek Fm.	0,00	3,18	6,19	1,22	0,64	0,00	0,00	0,00	0,00	0,66	1,43	0,00	13,32
Rytteråker Fm.	0,01	0,08	1,16	1,35	1,63	0,05	0,00	0,00	0,00	0,27	0,31	0,03	4,90
Skøyen Gr.	0,05	0,05	0,99	2,33	13,15	3,56	0,81	0,08	0,05	1,40	2,29	1,00	25,75
Kalvsjøen Fm.	0,04	0,00	0,00	0,30	3,75	4,50	1,22	0,93	0,20	0,13	3,29	2,11	16,48
G/K/L Fm.	0,00	0,00	0,00	0,10	0,77	2,47	2,62	0,67	1,00	0,00	1,93	8,54	18,11
Solvang Fm.	0,00	0,00	0,00	0,00	0,03	0,08	1,15	0,61	1,26	0,00	0,11	2,78	6,01
Kirkerud Gr.	0,00	0,00	0,00	0,00	0,00	0,20	0,66	0,57	7,15	0,00	0,39	4,42	13,39
clay/sand/ gravel	0,00	1,02	0,04	0,25	0,83	0,15	0,00	0,00	0,00	2,01	0,63	0,04	4,98
Fault zone	0,00	0,00	0,00	0,00	0,00	0,00	0,00	0,00	0,00	0,00	0,00	0,00	0,00
Unknown/not interpreted	0,00	0,00	0,00	0,00	0,00	0,00	0,00	0,00	0,00	0,00	0,00	0,00	0,00
Total	0,69	10,00	9,55	5,79	20,96	11,03	6,46	2,87	9,66	5,11	10,47	18,91	

b) **Overlap between formations in %**

Existing map (Owen et al., 2001) \ Map from this study	Gabbro	Bruflat Fm.	Vik/Ek Fm.	Rytteråker Fm.	Skøyen Gr.	Kalvsjøen Fm.	G/K/L Fm.	Solvang Fm.	Kirkerud Gr.	clay/sand/ gravel	Fault zone	Unknown/not interpreted	Total
Gabbro	85,94	0,00	0,00	0,59	0,17	0,09	0,03	0,23	0,04	0,00	0,02	0,00	87,12
Bruflat Fm.	0,00	56,55	12,22	3,60	0,57	0,00	0,00	0,00	0,00	12,42	0,76	0,00	86,12
Vik/Ek Fm.	0,00	31,85	64,83	21,00	3,06	0,00	0,00	0,00	0,00	12,98	13,63	0,00	147,36
Rytteråker Fm.	1,22	0,82	12,14	23,27	7,80	0,48	0,00	0,00	0,00	5,33	3,00	0,18	54,23
Skøyen Gr.	6,62	0,54	10,37	40,20	62,71	32,27	12,56	2,62	0,54	27,39	21,92	5,26	223,01
Kalvsjøen Fm.	6,21	0,00	0,00	5,20	17,88	40,79	18,92	32,56	2,08	2,53	31,42	11,17	168,75
G/K/L Fm.	0,00	0,00	0,00	1,76	3,69	22,41	40,52	23,42	10,33	0,00	18,47	45,15	165,74
Solvang Fm.	0,01	0,00	0,00	0,00	0,14	0,77	17,73	21,31	13,02	0,00	1,03	14,68	68,69
Kirkerud Gr.	0,00	0,00	0,00	0,00	0,00	1,85	10,25	19,85	73,99	0,00	3,69	23,36	132,98
clay/sand/ gravel	0,00	10,24	0,44	4,37	3,98	1,35	0,00	0,00	0,00	39,36	6,05	0,21	66,00
Fault zone	0,00	0,00	0,00	0,00	0,00	0,00	0,00	0,00	0,00	0,00	0,00	0,00	0,00
Unknown/not interpreted	0,00	0,00	0,00	0,00	0,00	0,00	0,00	0,00	0,00	0,00	0,00	0,00	0,00
Total	100	100	100	100	100	100	100	100	100	100	100	100	

In general, the two maps (from Figure 5.1) correspond well, but with notable differences in formation distribution. This is illustrated in Table 5.1 where the green boxes are situated in a diagonal line (outlined boxes), inferring that most of the mapped areas have the same formations at the same locations. Gabbro (volcanic plugs) and the Kirkerud Gr. are the most accurate mapped formations with an 86 and 74 % correlation, respectively. 23 % of the area identified as the Rytteråker Fm. in this thesis overlap with the Rytteråker Fm. of the existing map, while 40 % is assigned the Skøyen Gr. These are neighboring formations but easily distinguished in the field. Similarly, the Skøyen Gr. and Kalvsjøen Fm. overlaps 63 % and 41 %, respectively, with associating formations from the existing map. While these numbers are the highest compared with other formations in its column, they also reveal great differences between the two maps when studied in detail.

This comparison also reveals that most of the fault zones from the new map are situated in areas interpreted as the Kalvsjøen Fm., the Skøyen Gr. and the Gamme/Kjørrven/Lunner Fm. (31/22/18 % of total Fault Zone area respectively) by Owen et al. (2001).

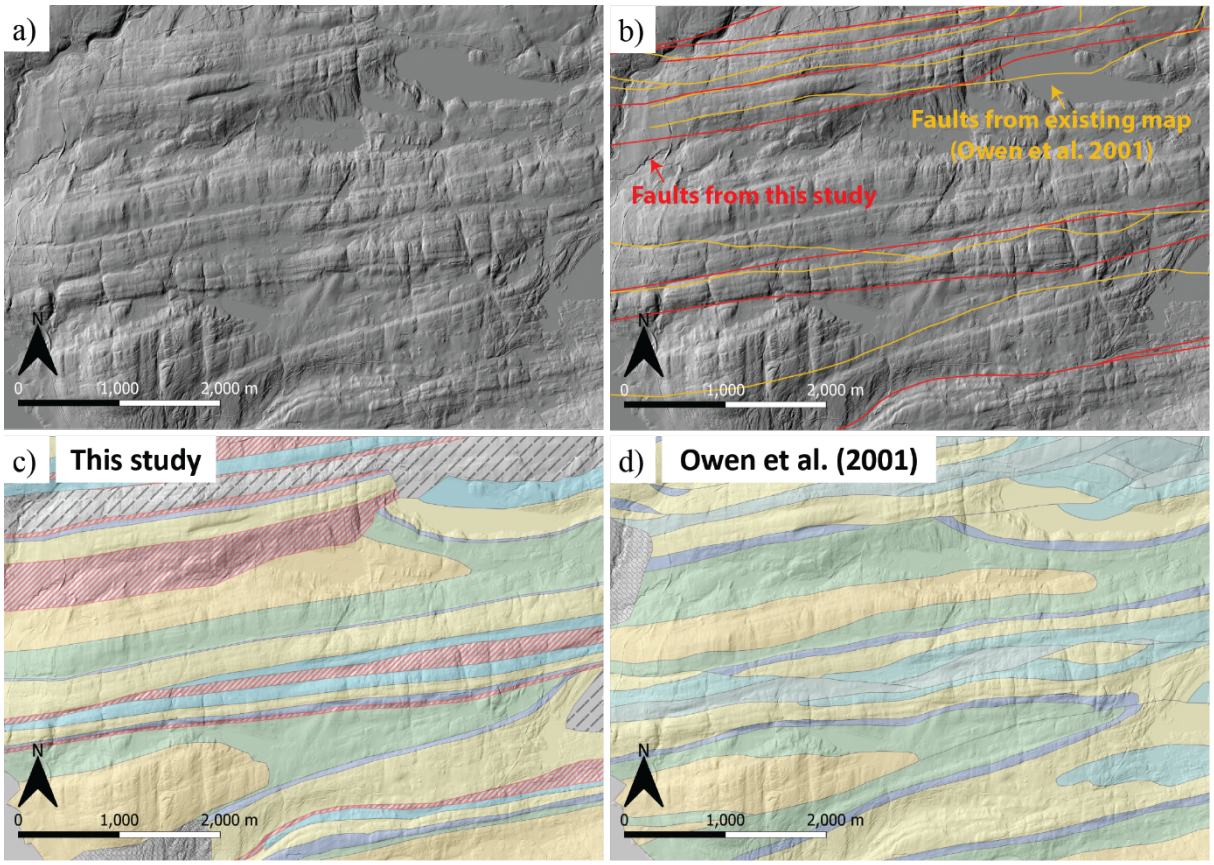

Figure 5.2: Comparison of the new map from this study and the existing map with LiDAR hillshade on a scale of 1:20.000. (a) Hillshade image for all areas in the figure. (b) Comparison of faults. Red lines: this thesis. Yellow lines: existing map. (c) The map from this thesis. (d) The existing map. Legends are the same as in Figure 5.6.

Placing the existing map on top of hillshade images shows that on a general basis, the existing map highlights the large-scale folds and structures enhanced by the hillshades reasonably well. But, when comparing the two maps to the hillshade on a smaller scale, as in Figure 5.2, the differences become more obvious. Faults from the existing map crosscut packages on the hillshade images, while faults from the new map follows the shades to a higher degree (see Figure 5.3). Further, most of the lithological boundaries from the existing map does not trace along with the structures from the LiDAR data when compared on a smaller scale. Short and local faults are often interpreted in order to make the map stratigraphically valid. These are not in correspondence to the shades from the LiDAR data.

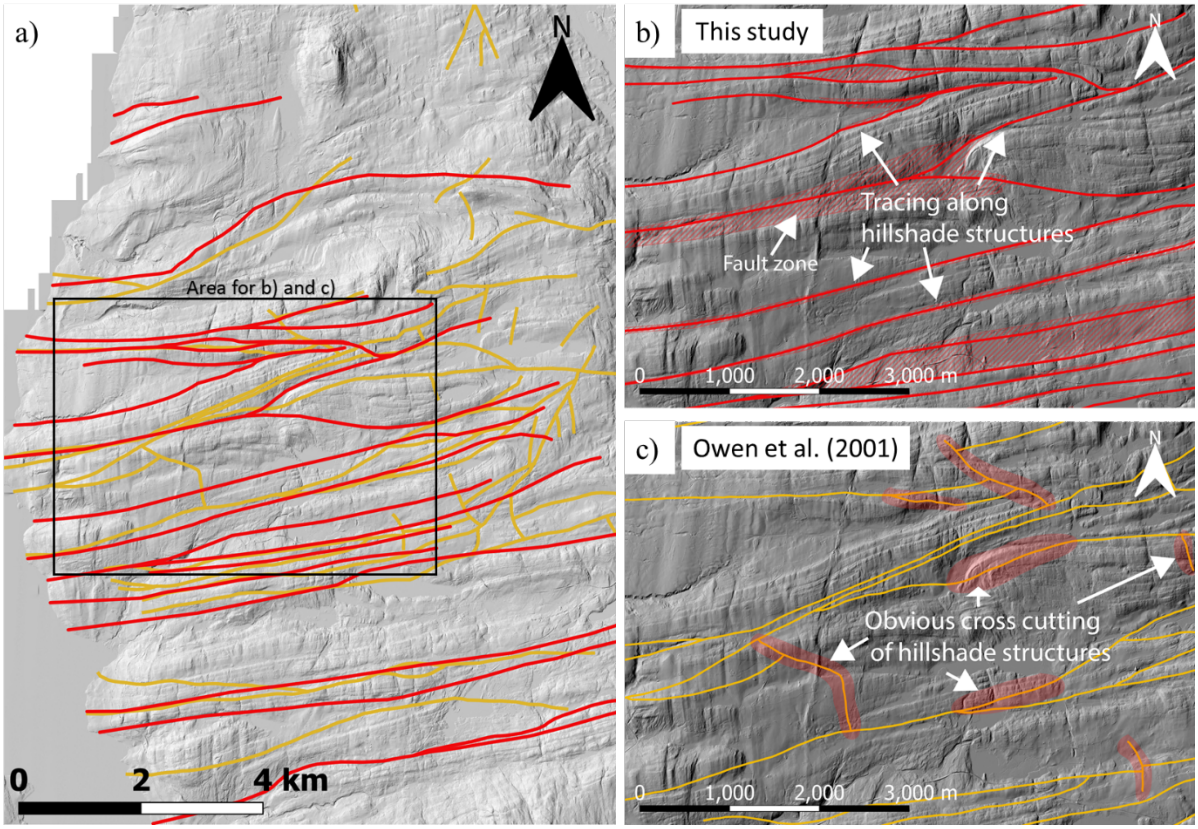

Figure 5.3: Faults interpreted in this study and from the existing map. (a) Red lines are faults from this study and yellow lines are from the existing map. (b) Zoomed in on area from (a), faults from this study can be observed to trace along the shades of the hillshade. (c) Faults from the existing map which can be observed to cut the structures enhanced by the hillshade. Some of the most obvious are highlighted in red color.

While mapping out the bedrocks at Hadeland, the LiDAR hillshade images are often (but not always) in correlation with field observations. Disconformities between structures from the LiDAR map can be observed separating field measurements that does not correlate between each other, either in the sedimentary sequence (assuming no break/hiatus) or strike direction. LiDAR hillshade images were used to draw the lithological boundaries between units, ground truthed by field measurements and observations. Due to poor exposure, large areas at Hadeland do not feature outcrops that reveals the geology. LiDAR hillshade images, especially in areas that are displayed as packages (defined in Chapter 3), enables boundaries to be traced following continuous E-W oriented ridges. Faults and fault zones are found between discontinuous packages or packages with different orientations. At this scale of mapping, faults are inferred where it causes a break in the continuity of the stratigraphic column (Groshong Jr, 2006). They are based on a combination of field observations and LiDAR hillshade images which originated in a pattern; if the field measurements did not display a consistent stratigraphic column, the hillshade map also exhibited an irregular pattern in the same area. This was also confirmed the other way around; if the hillshaded LiDAR images clearly display layer discontinuity between

two packages, field measurements largely confirmed that a fault is needed to make the map stratigraphically valid. An attempt to illustrate this can be seen in Figure 5.4 where non-correlating field observations are cut by the outline of the hillshade structures, inferring that structures identified from the LiDAR images correspond with field measurements. In short, the figure demonstrates that field observations and structures from the LiDAR data largely correspond with each other.

To take advantage of a methodology where LiDAR hillshade images provides as a leading or supplying tool for few field measurements/observations in a poorly exposed and large area, it is found important to always acquire an underlying awareness that single field measurements might deviate substantially from the geology on a scale of 1:50 000. Outcrop scale structures that remain unrecognized in the field can cause problems when mapping at this scale. Third order structures like these can obscure or complicate the interpretation at a later stage because bedding attitudes measured in small outcrops can derive from minor folds, minor fault blocks, or other structures, and does not need to represent the attitude of the formation boundaries. The connectivity of the contacts in the map is usually an interpretation, not an observation (also noted by (Groshong Jr, 2006)). Multiple measurements from each structure provided in the LiDAR hillshade image are therefore found important to acquire and sometimes also combine to ensure that aberrant measurements are not used as indicators for regional bedding on a larger scale.

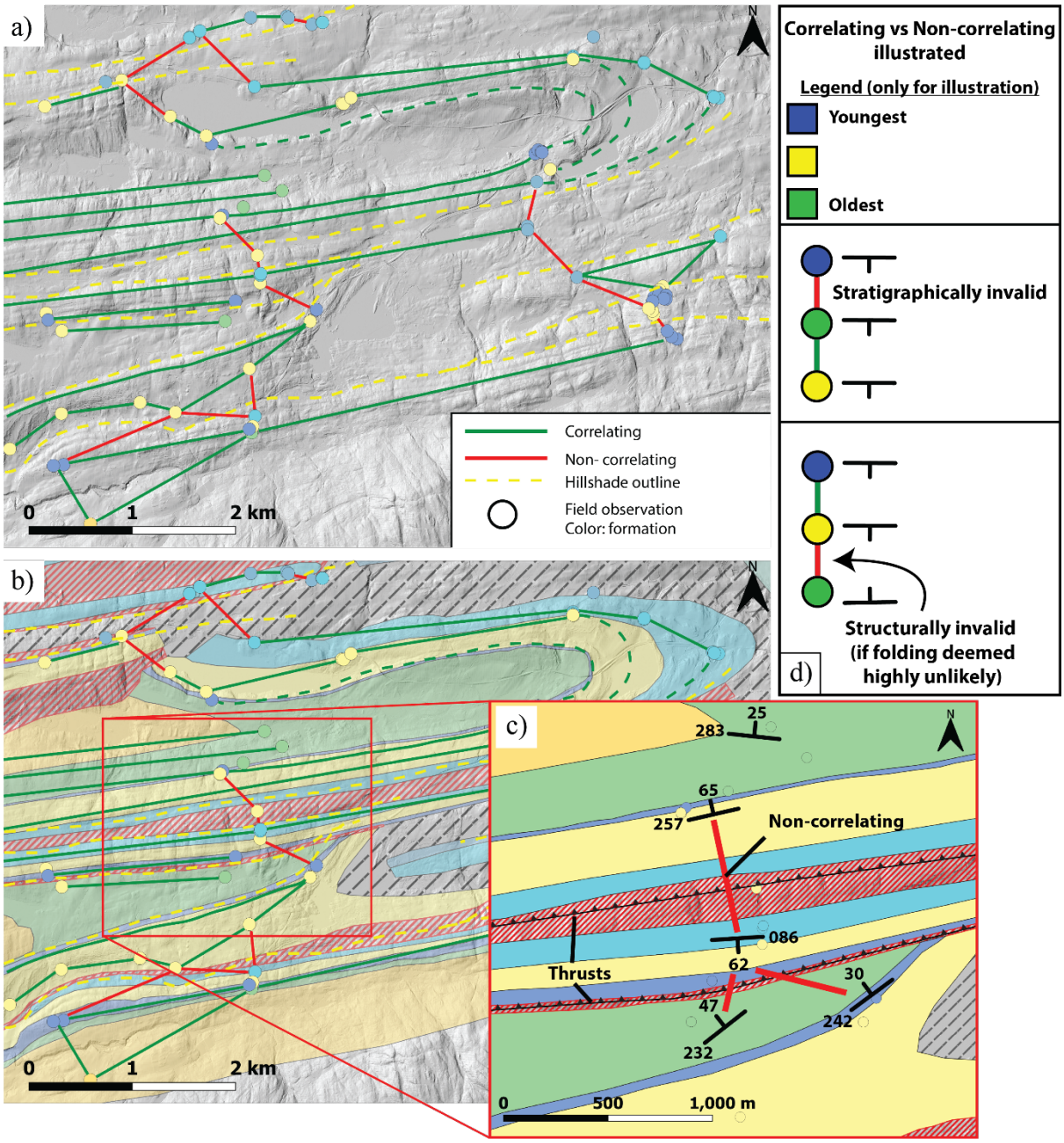

Figure 5.4: Correlation between field observations and how the appearance of the structures on LiDAR hillshade images generally display a change in structure where field observations contradict each other. (a) Green lines are drawn between field observations that are correlating between each other, both in bedding orientation and in the sedimentary sequence so that no fault must be interpreted in order to make the map stratigraphically valid. Red lines are drawn between field observations that does not correlate between each other, and the yellow stippled lines traces along some of the main structures from the hillshade image (as illustrated in (d)). Note that the circles that show position of field observations have the color of the corresponding formation interpreted in the field and are not necessarily correct. (b) Final map from this thesis. Fault zones are positioned between observations that are not corresponding with each other, and the hillshade outline has structures that display disconformities in the same areas. (c) Zoomed area in (b) with bedding measurements to demonstrate how the figure is built. (d) Simple illustration of how correlating vs non-correlating field observations is defined.

5.1.2 Cross-section and estimation of Caledonian shortening

Main cross-section

A main cross-section covering the central and south of Hadeland is created to display the folding and faulting on a larger scale, and to make estimates on the amount of shortening resulting from the Caledonian orogeny.

The section line for the cross-section (Figure 5.5) is perpendicular to the regional structural trends in the area and is based on average orientation of the main faults and trend of fold axes. Calculated average orientation for large scale faults in the map is 083-263 degrees (seen on rose diagram in Figure 5.15). Average trend for calculated fold axes is 265 degrees (seen in stereoplots from Figure 5.8). These correlate well and give a main direction of tectonic transport in the N-NNW to S-SSE direction (towards 175 degrees). The section is at a 1:1 scale with the topographic profile extracted from the LiDAR data.

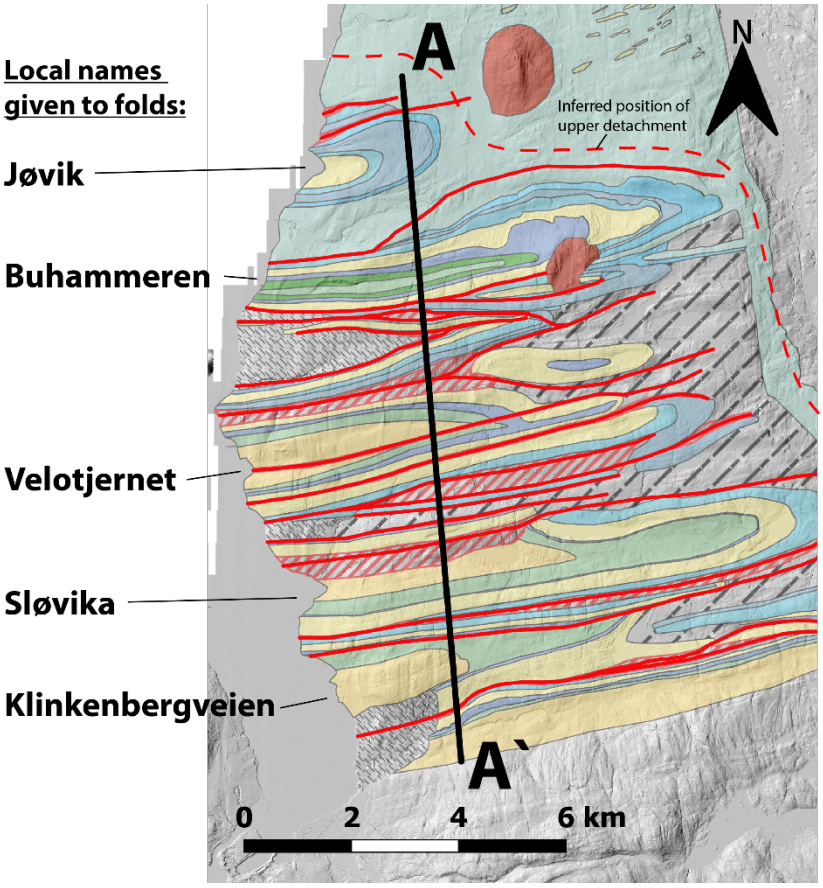

Figure 5.5: Map with placement of section line for cross-section A-A`. Inferred position of upper detachment is postulated from Morley (1983; 1987b).

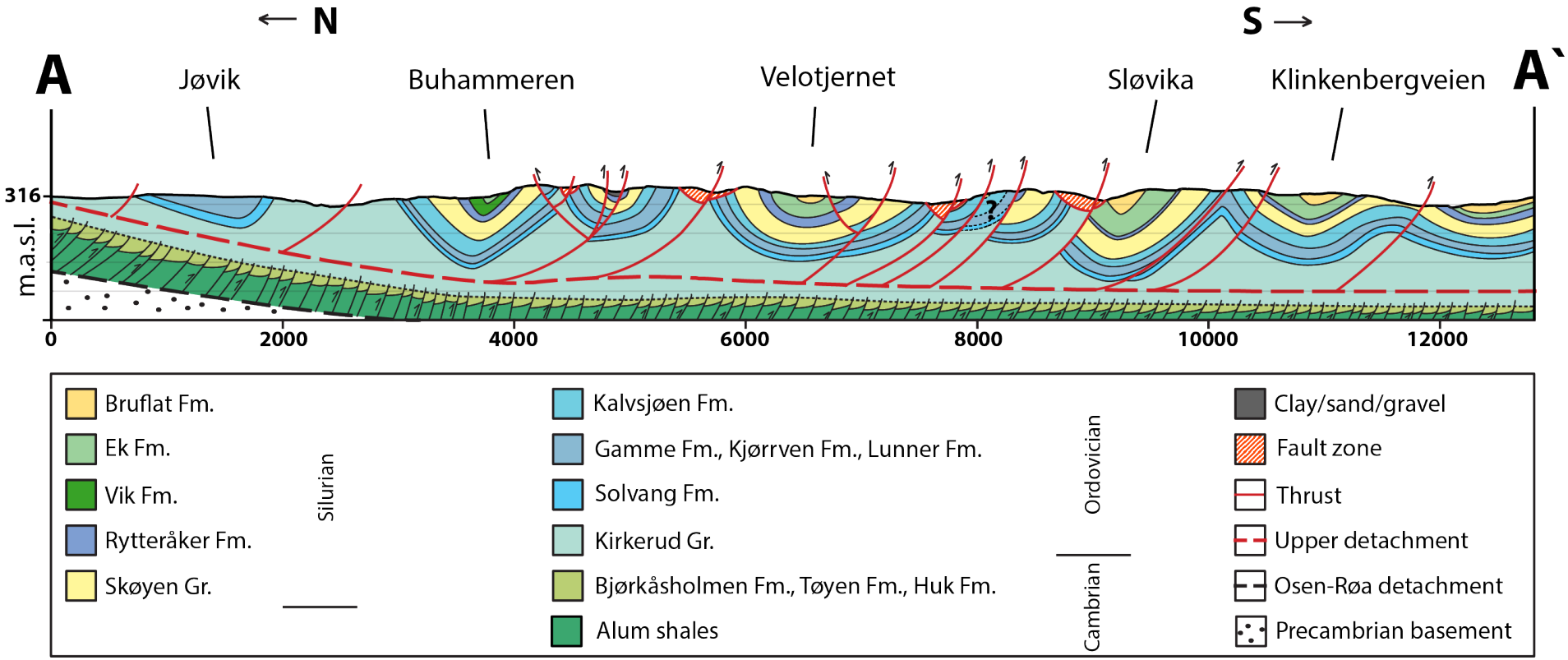

Figure 5.6: Main cross-section from A-A`. Position can be seen in Figure 5.5. The section displays how the difference between the shales from the Cambrian to mid-Ordovician exposed in north Hadeland from (Morley, 1983; 1987b) are separated from the more competent mid-Ordovician and Silurian succession with more lime- and sandstones. The postulated upper detachment in the Kirkerud Group and the Osen-Røa detachment are also included, but their relative depth might not be accurate. Forethrusts are the dominating type of faults, originating from or connected downwards to the upper detachment. Local names have been given to the five main folds that give a measurable fold axis.

The Cambrian to mid-Ordovician imbricated shale dominated units in the Alum shales and Bjørkåsholmen-, Tøyen- and Huk Fm., studied in detail by Morley (1983; 1987b), have not been in focus when producing the section and are therefore mainly drawn for illustrative purposes. The upper detachment postulated by Morley is situated within the shales of the Kirkerud Gr. and separates the Cambrian to mid-Ordovician and mid-Ordovician to Silurian units. As mentioned earlier, the thickness of the Kirkerud Gr. is challenging to determine due to immense deformation. In the profile, its thickness is reaching towards 750 meters which is an exaggeration of the 120 meters suggested by Owen et al. (1990) for illustrative purposes.

The thrusts in the profile are inferred as they cannot be observed directly in the field. In the cross-section they are foreland vergent (forethrusts) unless hinterland vergent (backthrusts) are needed to make the relative movement between formations add up and form a probable section. Faults that can be both fore- or backthrusts are interpreted to be forethrusts based on sandbox experiments, numerical models, and literature on faults in thin skinned foreland basins that have been consulted (e.g. Smit et al., 2003; Feng et al., 2015; Yan et al., 2016; Alania et al., 2017). This is mainly applicable for the two northernmost thrusts.

The fault zones are transferred from the map and LiDAR images. They are displayed as zones that penetrate the upper part of the section. In nature, these zones probably follow the fault core deeper towards the detachment. Relative movement is marked on thrusts with a measurable amount of displacement.

Bedding restoration and calculation of Caledonian shortening

The Solvang Fm. was found to be the optimal formation to restore in order to calculate the amount of Caledonian shortening. The formation is limestone dominated, and borders to the shale dominated Kirkerud Gr. in which the upper detachment is postulated (Morley, 1983; 1987b). Also, it is the formation with the least amount of eroded parts in the section which is desirable because it requires the least amount of interpretation.

When restored to original length (L_0), the area in the cross-section A-A` is stretched from 12.1 km today (L_1) to 17.4 km, which equals to a total shortening (e) of 5.3 km, or 30 %. This is calculated by removing the displacement caused by faults (without rotation of the layers) and then measuring the length of the remaining parts (the length of the Solvang Fm. in Figure 5.7b), assuming it has been constant throughout the event of deformation. Fault displacement

accommodate 31 % of the total shortening, while folds accommodate the remaining 69 %, see Figure 5.7.

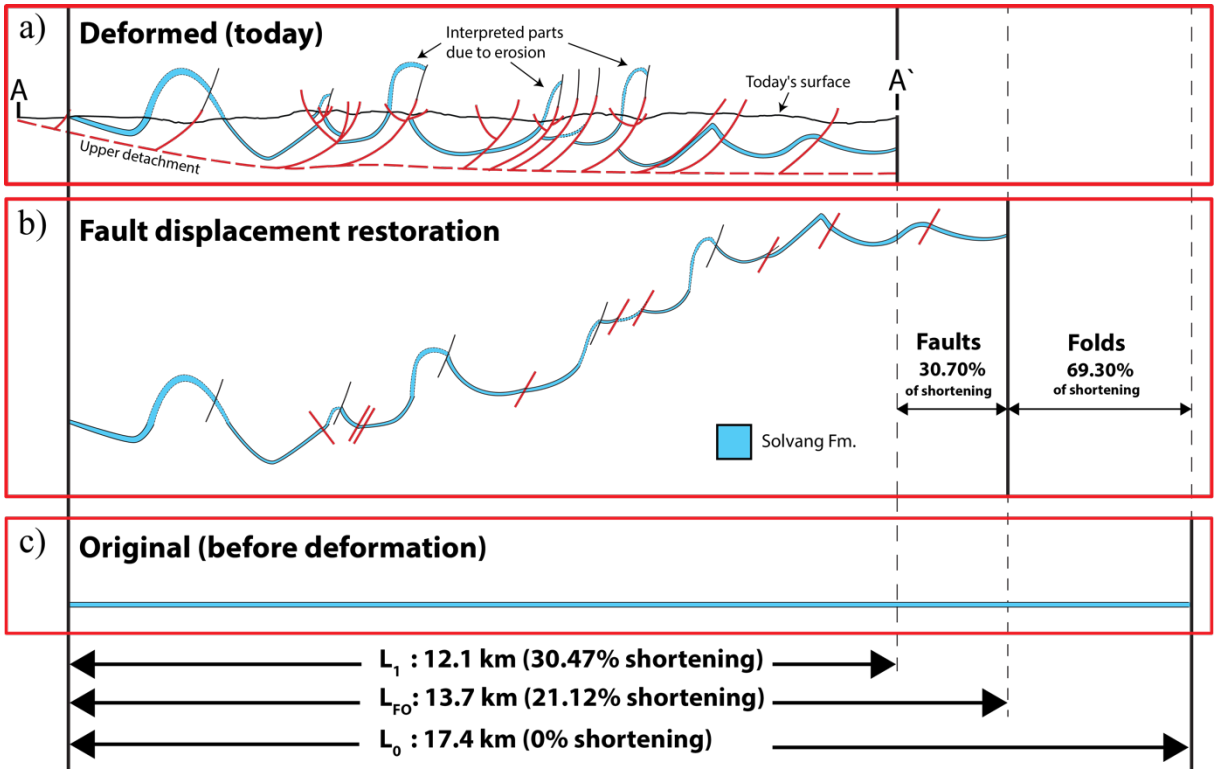

Figure 5.7: Schematic representation of sinuous- bed length restoration using the Solvang Formation as key bed. (a) The formation in its deformed state today with interpreted trace of eroded parts and faults. The formation is isolated from the cross-section in Figure 5.6. (b) Fault displacement restoration makes it possible to estimate and differentiate between shortening accommodated by faults and folds by connecting thrusted parts of the formation to each other. (c) Stretching the formation to its original length and comparing it to its current, deformed state results in a total shortening of 30.47 %. Note that this figure is for illustrative purposes only, and measurements were conducted in Adobe Illustrator.

Forethrusts (hinterland-dipping thrusts) account for 94 % of total fault displacement with backthrusts making up the last 6 %, or 1.5 % of total amount of shortening. This number, however, is likely too low to be representative for the entire succession because the Solvang Fm. is not cut by all of the backthrusts interpreted in the section.

5.2 Structures

This section describes the main deformation structures observed in the study area when travelling across Hadeland in search of outcrops for mapping of the area. The dominating and most prominent structures are interpreted to be of Caledonian age.

5.2.1 Folds

Map and profile

Folds, mainly synclines, can be seen on the map and the cross-section (Figure 5.1 and Figure 5.6) covering the central and south Hadeland to be one of the main structures to accommodate the Caledonian shortening of the successions. These folds have distinct characteristics, but common for them all is that thrusts attenuate one or both limbs with varying amount of displacement. An exception to this is the northernmost syncline, located in Jøvik, which is unaffected by thrusts with a coherent structure. It should be noted that the dominance of synclines is a result of erosion down to today's topography, and that the succession initial to erosion (assuming that erosion transpired post deformation, not syn deformation which is most prone) consisted of both syn- and anticlines as seen in Figure 5.7b.

The folds are symmetric to slightly asymmetrical with vergence towards both north and south, with upright to steeply inclined dip of axial surfaces. When focusing on the sand- and limestone dominated layers, the folds can be described as parallel with uniform thicknesses and interlimb angles in the range of 90-150 degrees (open to gentle after Fleuty (1964)), with the gentlest folds furthest south in the parts of Hadeland, where the competent Bruflat Fm. is to be found. The mechanically weaker and shale dominated Kirkerud Gr. in the lower parts of the stratigraphy is interpreted to fill up the spaces within the limbs of the overlaying folded layers, but this is a rational-based assumption that should be taken with care. The wavelength and amplitude of the folds are difficult to determine due to thrusting, but based on the cross-section and the restored Solvang Fm. from Figure 5.7b, wavelengths are reaching up to 2 km, but are commonly in the range of 1000 and 1500 m. The amplitude ranges between 240 and 600 m.

A general, large-scale trend of folds and their nature at Hadeland is that in the ENE direction, their hinge points can be observed inferring that the fold axes are plunging slightly in a WSW direction, and that the entire succession at Hadeland is tilted. Field measurements for five of the main folds allowed for fold axis calculations, seen in Figure 5.8.

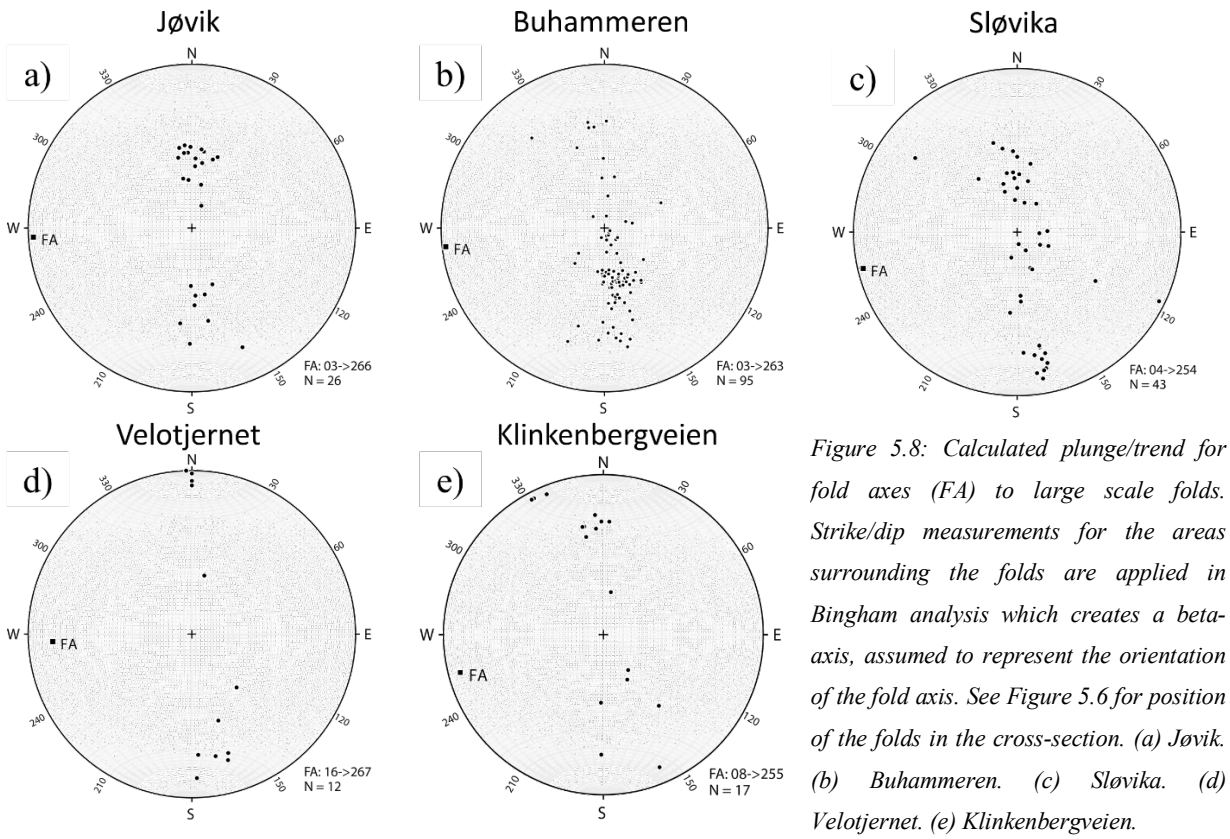

Figure 5.8: Calculated plunge/trend for fold axes (FA) to large scale folds. Strike/dip measurements for the areas surrounding the folds are applied in Bingham analysis which creates a beta-axis, assumed to represent the orientation of the fold axis. See Figure 5.6 for position of the folds in the cross-section. (a) Jøvik. (b) Buhammeren. (c) Sløvika. (d) Velotjernet. (e) Klinkenbergveien.

The stereonets, which assumes that the folds are cylindric within the area of measurements, reveal that the fold axes plunge between 3- and 16 degrees towards W and WSW. Two of the folds (Velotjernet and Klinkenbergveien) both have under 20 bedding measurements. These two also have plunging values notably higher than the other three, and the plunge of the fold axes seen as a whole are probably closer to four degrees. The plunge is also confirmed by drawing a crest line through the dip vectors, which would not go through the origin in any of these stereonets meaning a plunge of more than zero degrees. Conical folds would have measurements aligning in a curved crest line, which is not the case in these plots.

Field

In the field and on outcrop scale, folds can be observed in different lithological units with different characteristics. They are uncommon to observe compared to thrusts.

Outcrops with steep and pronounced dipping beds locally tend to be buckled parallel with bedding. An example of this can be seen in Figure 5.9a, where homogenous beds in the Bruflat Fm. with a strike/dip of 267/63 are gently folded. Multilayered folding like these are observed in outcrops that are displaying the structures in a N-S direction, and most often in areas with a

uniform bedding and relatively undeformed geology. The folds often have wavelengths in the meter scale. Figure 5.9b shows a similar type of folding in the same area as Figure 5.9a, but where one main fold is standing out and dominates over smaller and less pronounced folds with amplitudes between 10 and 20 cm.

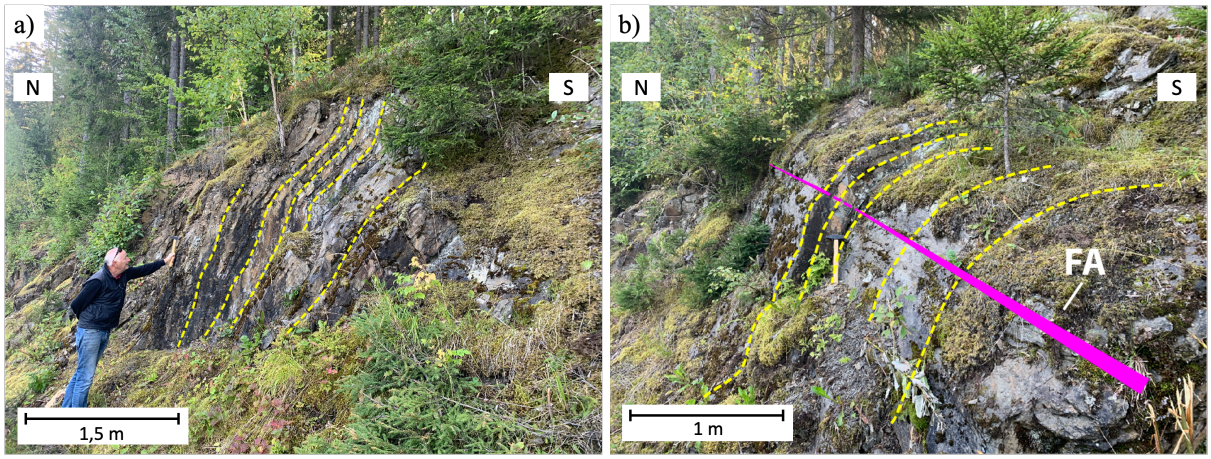

Figure 5.9: Bedding parallel shortening folds. Yellow lines follow selected beds to emphasize folding. (a) Example of outcrop with multilayered disharmonic folds in the Bruflat Formation. The folds are asymmetric and have interlimb angles close to 160 degrees, with few or no obvious faults close by. (b) Located 40 meters to the SW of (a), also in the Bruflat Formation. One larger, gentle, fold with measurable fold axis of 08/078. Loc.: 60.3015928, 10.3902061.

A similar style of folding can be found in the Skøyen Gr. In the outcrop on Figure 5.10, the layers have been thrusted to create an open anticline with an interlimb angle sub 90 degrees which is not observed elsewhere in a similar style of folding. This indicates that this type of folding can be a result of relatively ductile deformation and flexural slip of layers propagating towards the foreland of the basin with main direction of shortening orientated N-S which corresponds with the trend of the fold axis at 108 degrees (Figure 5.10).

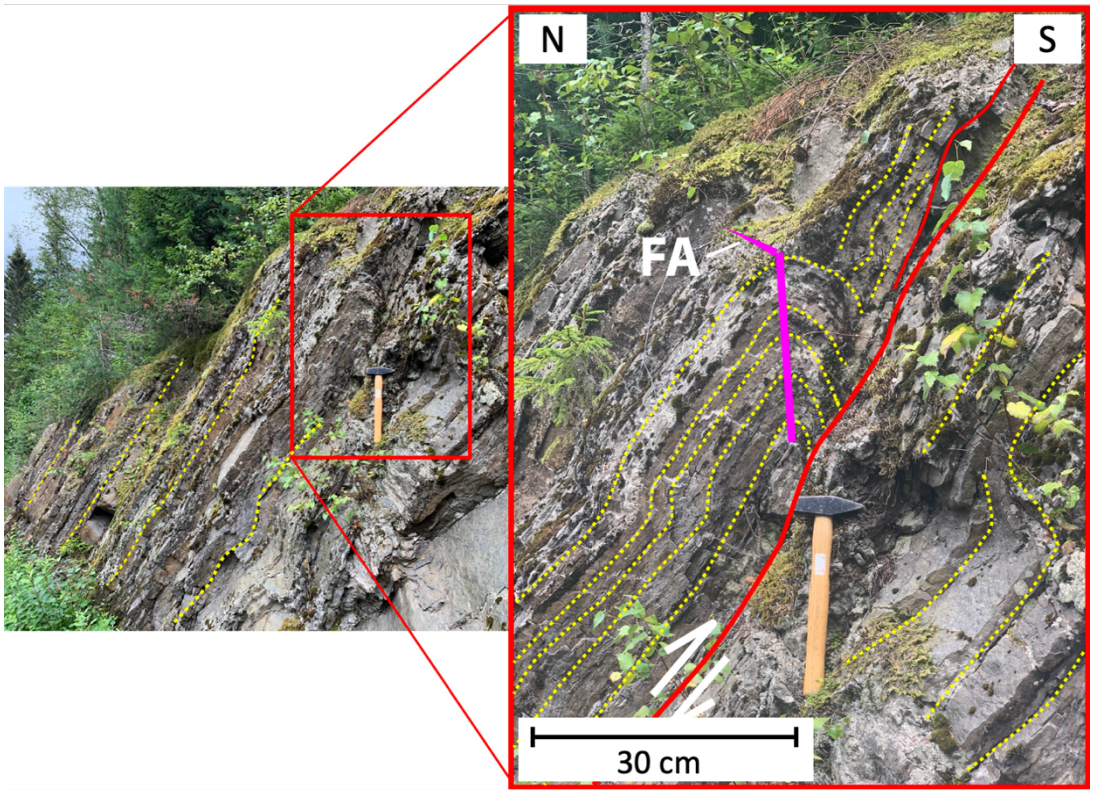

Figure 5.10: Open fold in the Skøyen Group with interlimb angle sub 90 degrees. Fold axis has a plunge/trend of 11/108, and bedding is 261/58. Wave riffles are found nearby and confirms bedding direction. A bedding parallel forethrust is separating the folded layer in the hanging wall from the footwall. Loc.: 60.3191428, 10.4238291.

Folds of greater wavelength (over 10 meters) are not commonly observed in the field. Still, some localities in the area retain folds which can be inferred to have wavelengths and amplitudes exceeding the outcrop scales. Figure 5.11 and Figure 5.12 are two examples of these, where a small section provides insight to hinge points in folds with measurable fold axes. The anticline in Figure 5.11 marks the change in strike direction with a small backthrust attenuating the forelimb. Measurements following the road section north and south of the fold suggests a wavelength greater than 100 m.

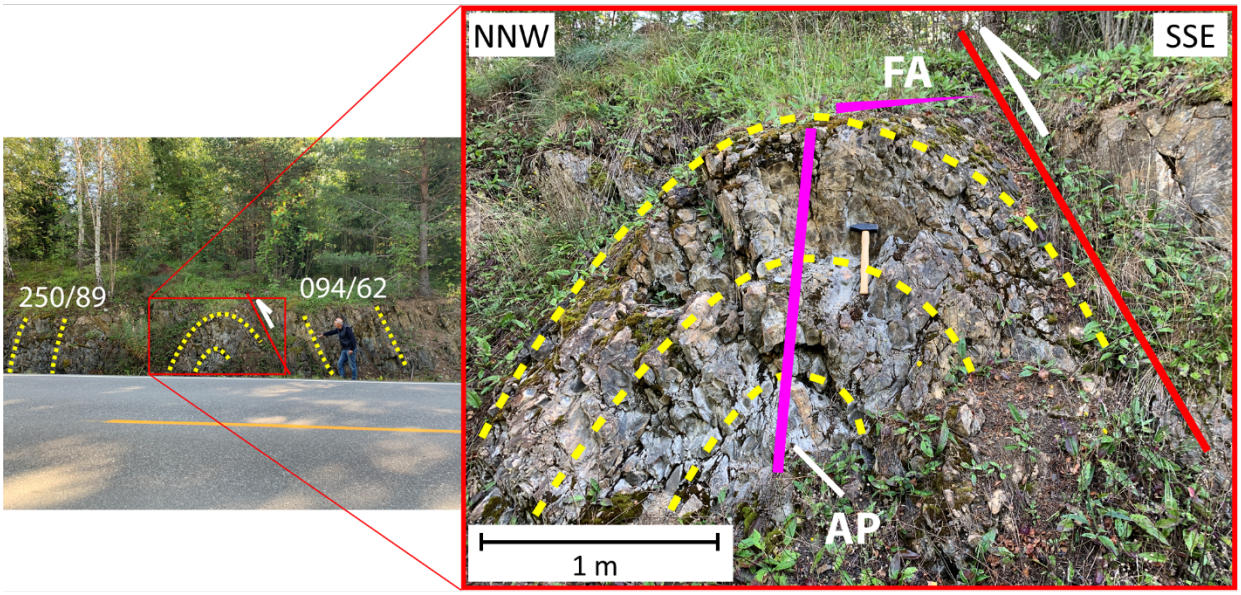

Figure 5.11: Tight (opening angle 65 degrees) anticline in the Gamme-, Lunner-, Kjørrven Formations. The fold is parallel, and the forelimb is attenuated by a small backthrust with immeasurable displacement. Bedding shifts from steeply dipping towards NNW to SSE, and fold axis is 34/238. Wavelength is close to 100 m based on bedding measurements on the map. Loc.: 60.3133276, 10.3845751.

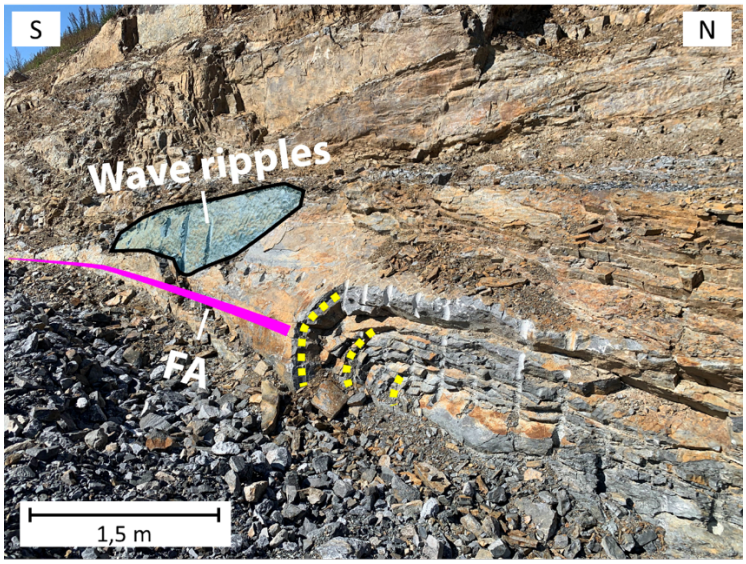

Figure 5.12: Horizontally inclined and parallel anticline with wave ripples in the Skøyen Group. Fold axis is 00/264, and the surrounding outcrops in the area displays a chaotic pattern, close to a fault zone on the map. This outcrop might represent an insight in a fold that is markedly larger than what can be observed. Loc.: 60.2676088, 10.4993745.

Most of the observed folds are in the upper and more competent formations, from Kalvjøen- to the Bruflat Fm., except in the less competent shales in the Ek- and Vik Fm. All of the folds can be classified as parallel 1B following the classification of Ramsay (1967) based on dip isogons. The stereonet of six measured fold axes (Figure 5.13) shows a general E-W trend, with a modest plunge up to 34 degrees. Wavelength ranges from dm scale and to some 100 meters, based on change in dip direction from the map.

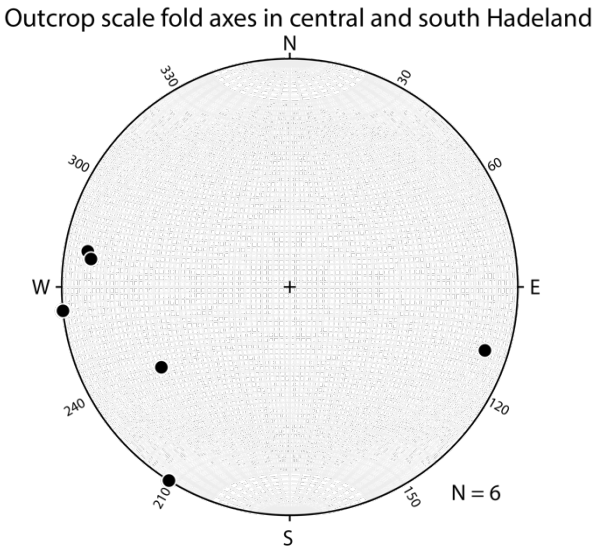

Figure 5.13: Fold axes of measured outcrop scale folds.

5.2.2 Thrusts

Map and profile

Thrusts on a large scale have been identified by structural observations and field measurements indicating stratigraphical impossibilities, combined with LiDAR hillshade images. Fault zones have been chosen to cover areas on the map where a fault is located, while LiDAR hillshade images display a significant and distinct area for where the exact and final trace of the fault might be located, as demonstrated in Figure 5.14. The main reason for this is to illustrate how LiDAR data can be applied when used in bedrock mapping, and to clarify its potential. In highly drift- covered areas like Hadeland, the final trace of a fault has to be postulated based on few observations and measurements, and a fault zone outlines this area with high certainty.

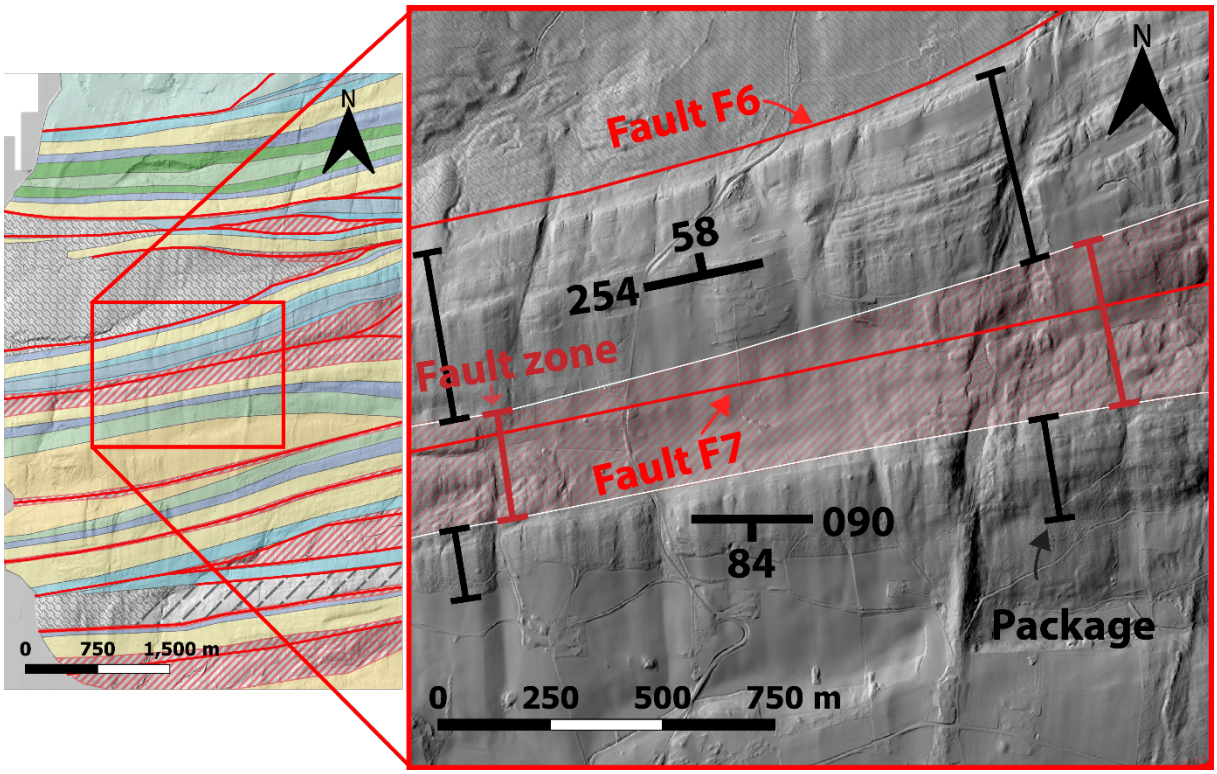

Figure 5.14: Fault zone for fault F7. To the left is the map from this thesis with lithological boundaries (legend in Figure 5.1), while the area projected in the red square to the right shows how the interpreted fault zone (marked with dark red) surrounds the fault. It is situated between two packages (marked with black) with opposite direction of strike. LiDAR hillshade clearly show E-W oriented structures in the packages and a more plane structure between the packages, where the fault zone is. Fault F6 in the top is on the northern rim of a package, and the boundaries for an alternative fault zone is therefore also not interpreted.

Most large-scale faults in central and south Hadeland are forethrusts connected to the upper bedding-parallel detachment in the Kirkerud Gr. as illustrated in the constructed cross-section from A-A` (Figure 5.6). The steepness of the thrusts cannot be verified without use of seismic surveys and should be regarded as conjectural in the cross-section where they have a dip between 35 and 50 degrees, flattening towards the detachment. None of the inferred backthrusts have their origin in the upper detachment, but they are nucleating from larger forethrusts in the upper part of the succession, close to today's surface. Backthrusts make up only 12.5 % of the total number of thrusts, and accounts for roughly 10 % of total thrust displacement which makes them relatively insignificant at Hadeland.

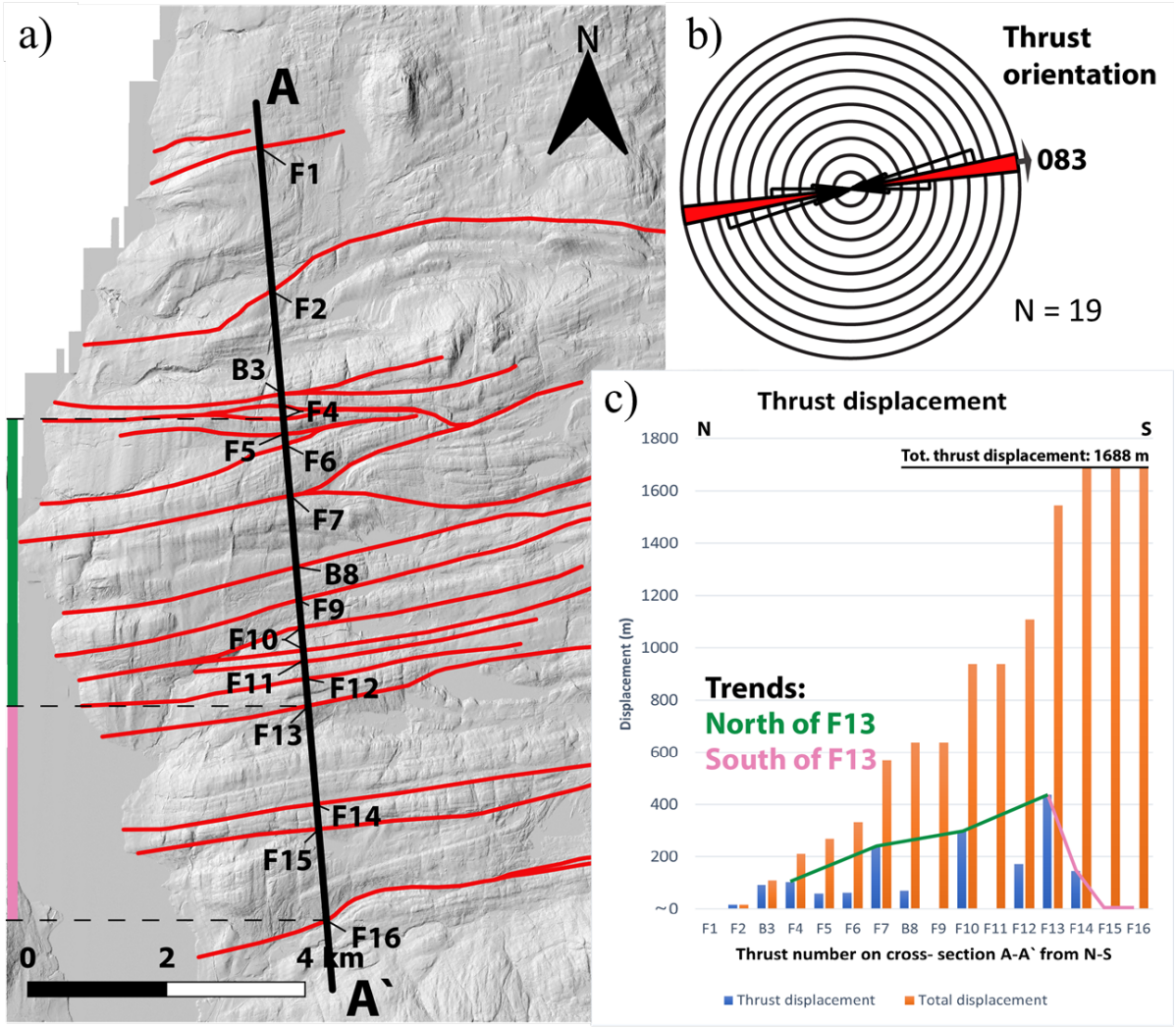

Figure 5.15: Faults from cross-section A-A` and associating statistics. (a) Section line for cross-section A-A` with labels to identify different faults. F is short for "forethrust" and B is short for "backthrust". (b) Rose diagram for orientation of thrusts. Red spoke is calculated average and have an orientation of 083-263 degrees. The diagram does not include weight on fault length, but if fault length is weighted for, the difference is not notable due to overall similar lengths originally. (c) Horizontal displacement for the identified faults. Blue bars are displacement for associating thrust and orange is total thrust displacement, going from F1 to F16. An increase in displacement between the most prominent faults is marked with green, north of F13, and a general decrease south of F13, marked with pink. The extent of these trends can also be seen to the left in (a). Displacement is measured in the key layer of the Solvang Formation with exception of B8 which originates stratigraphically higher and is measured in the Kalvsjøen Formation.

Based on the cross-section, the largest horizontal displacement accommodated by a single thrust is found to be F13 with more than 400 m (Figure 5.15), while the average displacement for a thrust is close to 100 m. From north to south, thrust displacement increases between the locally most displaced thrusts F4, F7, F10 and F13, as seen by the green trend line (Figure 5.15c). South for F13, thrust displacement decreases (pink line), with the two most northern thrusts (F15 and F16) having displacements of close to 0 m. This is also the area with the broadest

folds and the stratigraphically youngest units (Bruflat Fm.), distal relative to the Caledonian front syn- deformation. Spacing is relatively uniform from N to S, but increases south of F13. The orientation of the faults is widely uniform, as seen on the rose diagram (Figure 5.15b), with a main strike orientation going ENE-WSW.

There is no obvious relationship between thrusts and formations (hence layer competence) on this scale within the mid-Ordovician and Silurian strata. The first- and second order thrusts have been propagating seemingly unaffected by the competence difference between the formations towards the surface, and can be seen on the updated map to be situated in both shale-, sand- and limestone dominated formations. The evolution and development of the faults syn deformation is further discussed in Chapter 6, but at this point, everything but their position and extent on the surface remain as speculations and cannot be confirmed without seismic surveys.

Field

Thrusts are common to find in the field in the mid-Ordovician and Silurian successions at Hadeland compared to folds. Still, most of the outcrops does not display thrusts that have a measurable displacement, and they can be challenging to separate from bedding planes between layers in poorly exposed outcrops. Their orientation were found difficult to measure, but 27 of the observed faults had characteristics which allowed for relatively confident measurements.

Low angle thrusts associated with bedding parallel shortening are observed in the Bruflat Fm. (Figure 5.16a), the Kalvsjøen Fm. (Figure 5.16b), and in the Skøyen Gr. (Figure 5.16c). They are oriented sub-parallel to the bedding, often with angles deviating less than 15 degrees from the dip of the layer in which the fault is situated. Layers surrounding the shortened layer have bedding perpendicular cleavages, often concentrated within selected layers. In all of the bedding parallel shortening thrusts, the hanging wall has been transported south relative to the footwall.

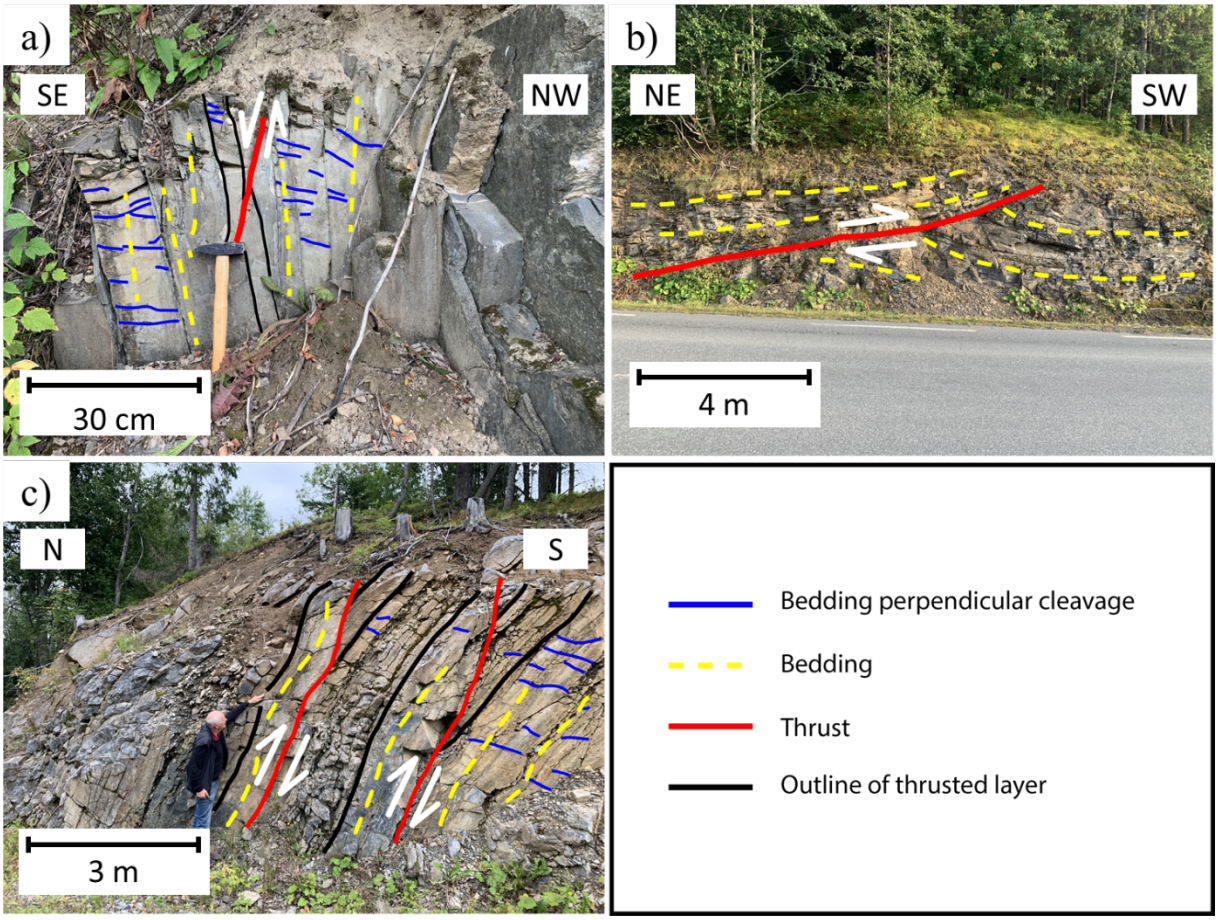

Figure 5.16: Thrusts related to bedding parallel shortening. (a) Vertical dipping beds in the Bruflat Formation with pronounced bedding perpendicular cleavages. (b) Thrust in the Kalvsjøen Formation. Less pronounced cleavages. Drag of foot block indicates direction of movement. (c) Two bedding parallel thrusts in the Skøyen Group. Trace of bedding (yellow stippled line) also shows that these layers have been gently folded. (a)/(b)/(c) loc.: 60.3086128, 10.4216089/60.2807412, 10.5802777/60.2754035, 10.5682910.

Figure 5.17 displays how the majority of the measured thrusts are observed in the field in outcrops that expose the geology parallel to the strike of the faults. A reason for this is that most of the road sections follow a E-W orientated topography at Hadeland, which again is a direct consequence of the folded and faulted geology in the area. These faults have displacement of some few centimeters, and they have strike and dip that enables them to be separated from more erosive-resistant layers in the formation that are standing out. They commonly extend horizontally through the exposed outcrop, and some also have calcite precipitated in the faults planes or calcite coated fault planes where slickensides, if present, can indicate the relative movement between the fault blocks (Figure 5.17c).

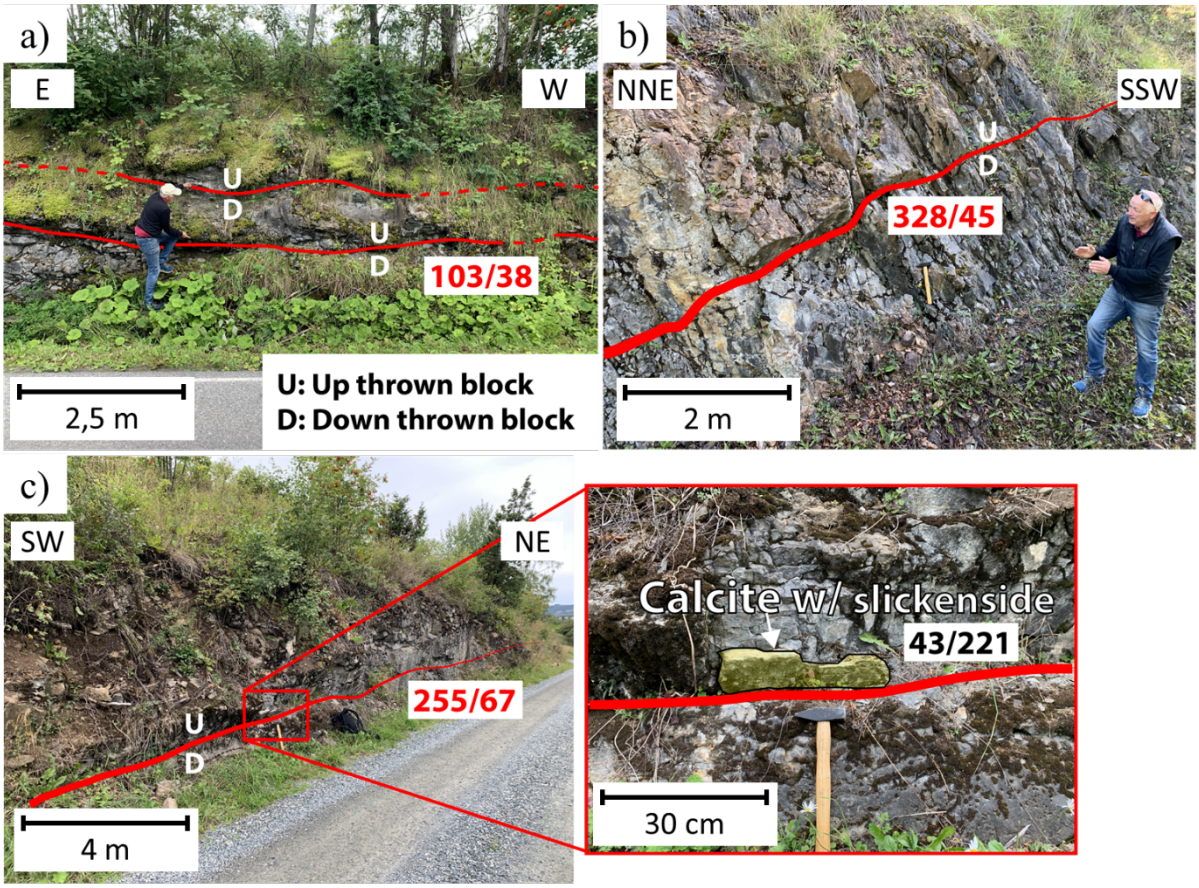

Figure 5.17: Thrusts marked with red line and corresponding orientation to fault plane with red numbers. Up- and down thrown blocks are marked with "U" and "D", respectively. (a) Two parallel thrust planes in what is interpreted to be upper parts of the Gamme Formation or the Kjørrven Formation. (b) Distinct thrust in the Kalvsjøen Formation which is perpendicular to bedding. (c) Calcite precipitated with slickensides indicating relative movement in the SW-NE direction, also in the Kalvsjøen Formation. (a)/(b)/(c) loc.: 60.3006859, 10.4992768/60.3128449, 10.3845810/60.2782198, 10.4997575.

Poles to measured fault planes can be seen in Figure 5.18, where contouring is used to enhance the overall trends in the plot. The majority of faults are steeply dipping with more than 60 degrees towards ESE or W.

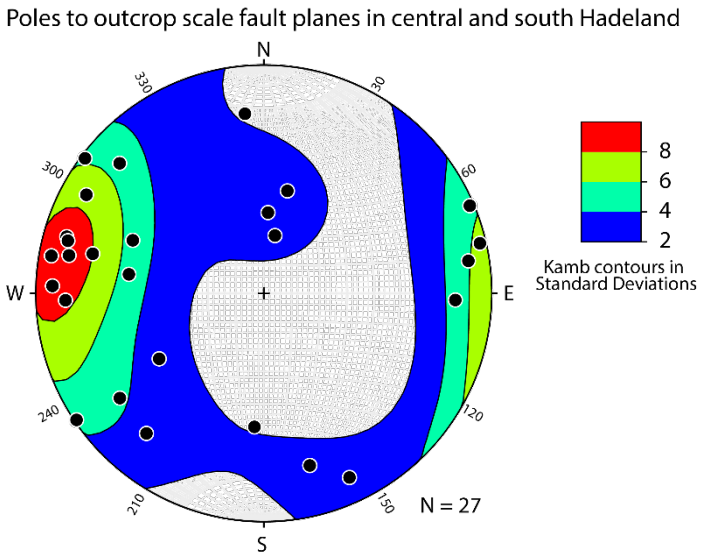

Figure 5.18: Poles to outcrop scale fault planes. Kamb contouring is used to enhance general trends in the stereonet. It creates a variable area which is color- depending on the number of data points, seen in the legend to the right. A dip direction towards ESE can be seen to be the dominating orientation of faults on outcrop scale.

5.2.3 Extensional lineaments/normal faults

Map

N-S oriented lineaments in the study area are, as stated in the beginning of the chapter, interpreted to be related to the Permian extension. N-S lineaments have been determined from LiDAR hillshade images (Figure 5.19), where an overall trend of 005-185 is dominating when all lineaments are included and line-length is not weighted for (as seen in rose diagram in Figure 5.19c). The largest and most prominent lineaments (blue lines in Figure 5.19a) are overall more east-west orientated compared to smaller lineaments (purple lines in Figure 5.19a). The longest continuous lineament has a length of 8.5 km, while the width is measured to be reaching 70 m (between 50 m and 130 m depending on where the start and end is defined, which is debatable). Normally the width is in the range of 10 to 30 m. The western parts of the area display a higher degree of NNE-SSW oriented lineaments compared to the eastern parts, where more of an NNW-SSE trend is dominating.

Strike/slip movement is not found to have resulted in displacement for the lineaments, and because heave and vertical throw cannot be determined from the LiDAR data, all the lineaments cannot confidently be identified as extensional faults. The term “lineament” is still considered suitable, even if the general interpretation is extensional faults. Nomenclature might suggest that these zones should be regarded as joint zones because they do not show any signs of fault-parallel displacement (Gabrielsen et al., 2002), but this will not be taken to further discussion here.

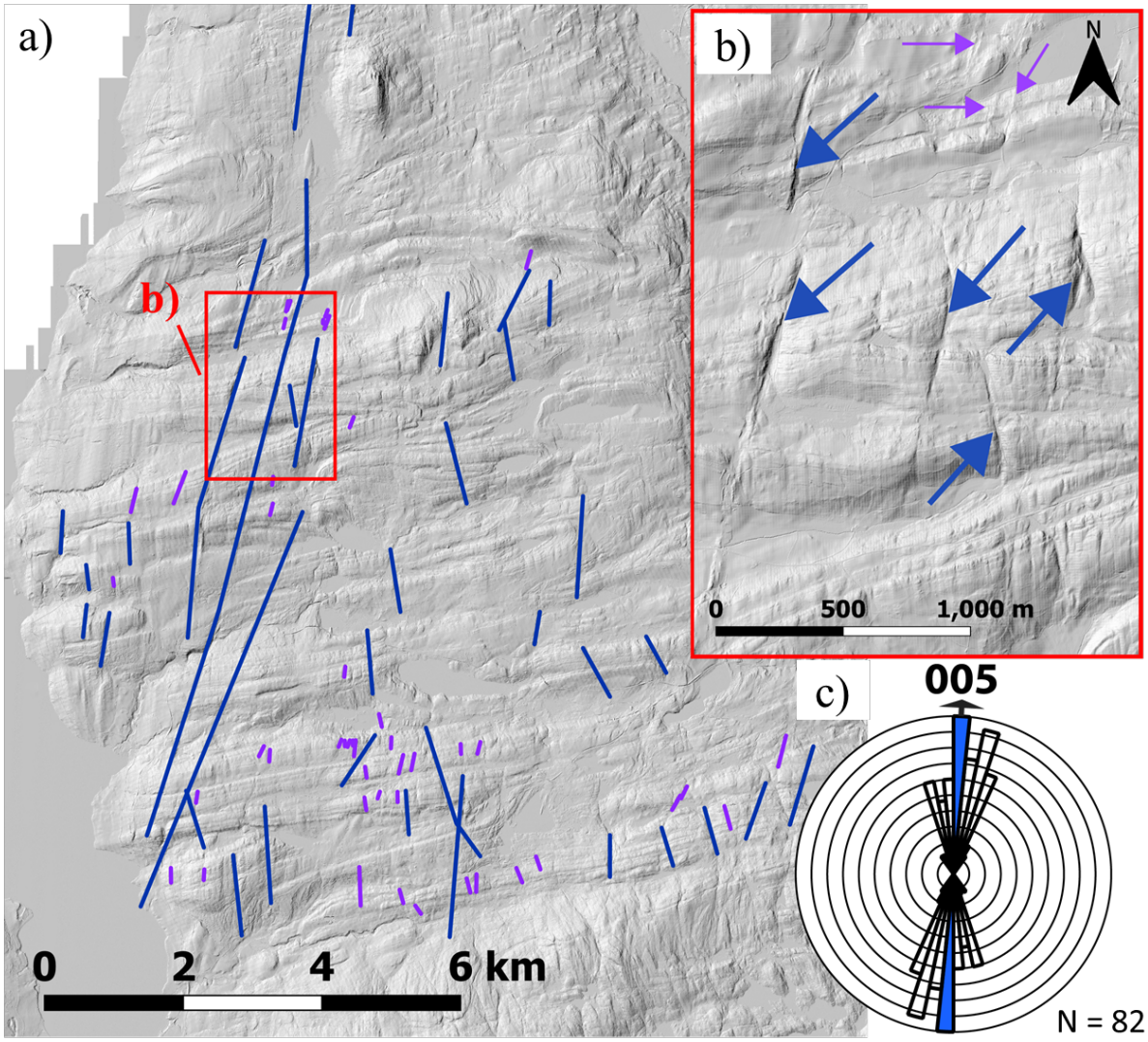

Figure 5.19: N-S oriented lineaments interpreted to be related to Permian extension identified by LiDAR hillshade images. (a) Overview of all lineaments in the study area. Blue lines have been interpreted on a scale of 1:40 000 while purple lines have been interpreted on a scale of 1:7 500. (b) Area marked in red square in (a). Displays how lineaments are seen on a hillshade map with azimuth 300 and altitude of 40. Arrows are pointing at interpreted lineaments with corresponding colors. (c) Rose diagram for all lineaments, not weighted for line-length. Blue spoke is main orientation and have a trend going 005-185.

Field

The most prominent structure related to the Permian extension in the field is magmatic dikes with a consistent N-S orientation. They are parallel to sub-parallel with the major Randsjord-Hunndal fault, cutting through the sedimentary successions with different angles and widths, most commonly near vertical and with widths between 0.5- and 2 m. Magmatic dikes are found throughout the study area with different mineral compositions, texture, phenocrysts, and colors. In the area close to the gabbroic volcano plug at Buhammeren, dikes range from dark and basaltic to light colored and rhyolitic. Porphyritic dikes with phenocrysts of pyroxenes are also

observed. The diversity of dikes is within tens of meters suggesting a complex network of magmatic chambers at the time of creation.

Due to immeasurable/small displacement and poor outcrops, any fault with a relative E-W movement between the hangingwall and the footwall was not determined in the field without further indications. Extensional faults of Permian age were only determined by slickensides or lineation's oriented E-W, which was found in twelve locations (see Figure 5.20 for example and Figure 5.21 for stereonet with all E-W related slickensides and lineaments).

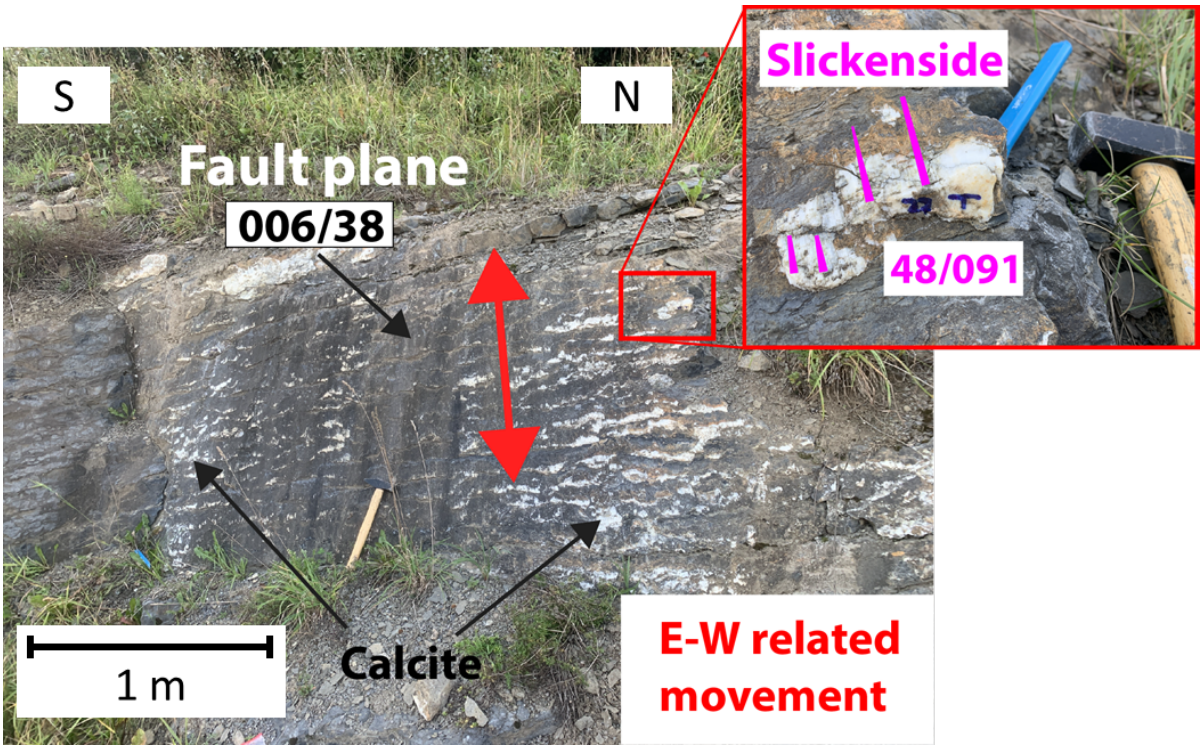

Figure 5.20: E-W oriented movement on fault plane determined from calcite slickensides in the Kalvsjøen Formation. This is an example of how structures related to the Permian extension can be observed in central and south Hadeland. Loc.: 60.29597256, 10.56777049.

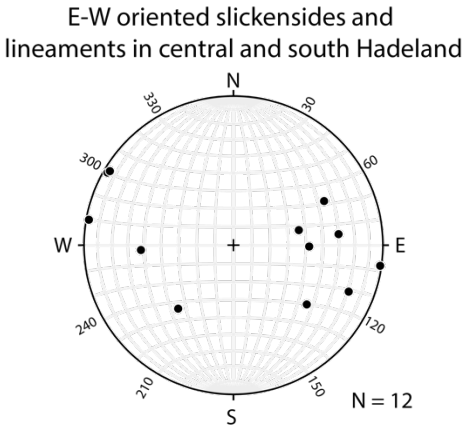

Figure 5.21: Slickensides and lineation's measured in central and south Hadeland with an orientation in the E-W direction. Interpreted to be related to Permian extension.

A number of the large scale lineaments was attempted visited in the field, but none were visible due to the overlaying sediments and poor exposures resulting in no field measurements and observations of the faults.

5.2.4 Final geological map for central and south Hadeland

A bedrock map with traditional mapping symbols covering central and south Hadeland has been produced by combining initial mapping of formations, cross-section for thrust orientations, and normal faults delineations based on LiDAR hillshade images (Figure 5.22). Fault zones could be eliminated by extrapolating the extent of surrounding formations, but this is not performed in this thesis.

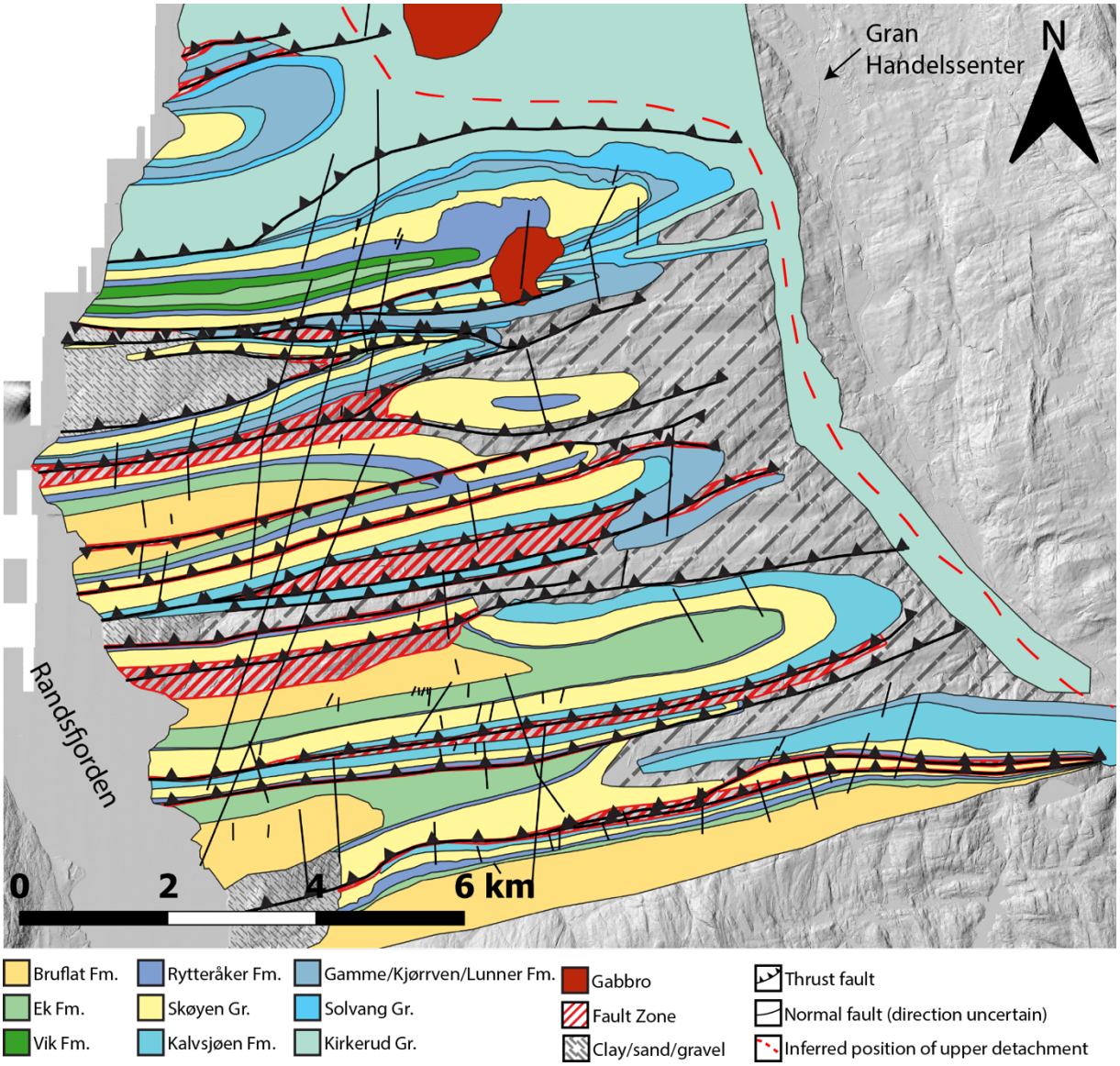

Figure 5.22: Final bedrock map from this study covering central and south Hadeland with structural symbols displaying dip direction of thrusts. Extensional faults interpreted to be of Permian age have orientations which are uncertain. The map is on top of LiDAR hillshade images, and Gran Handelssenter is noted in the northeast as positional reference.

5.3 Calcite samples and dating

Out of 34 calcite samples prepared and sent for dating, seven proved adequate for further analysis and dating as described in Figure 4.6 despite none of them being particularly well suitable. Extremely low U concentrations is the main cause for the large uncertainties in the age estimates. 26 samples had virtually no U and radiogenic Pb or unfavorable U/Pb relations, while the last one was not a carbonate or covered with epoxy.

The age estimates can numerically be seen in Table 5.2 and as a scatter plot in Figure 5.23. All information and further details on the calcites and dating performed can be seen in Appendix A. Five out of the seven show ages younger than 35 Ma, and only Cal 15 at 236 ± 39 Ma is close to the aimed ages of Permian rifting (~310-241 Ma) or the Caledonian orogeny (~425-400 Ma).

Table 5.2: Age estimates (Ma) and 95 % confidence interval for dated calcites.

Calcite ID	Age (Ma)	± 95 % conf.
Cal 2	5	16
Cal 4	34	35
Cal 7a	26	21
Cal 12	103	73
Cal 14	4.6	5.7
Cal 15	236	39
Cal 19	29	69

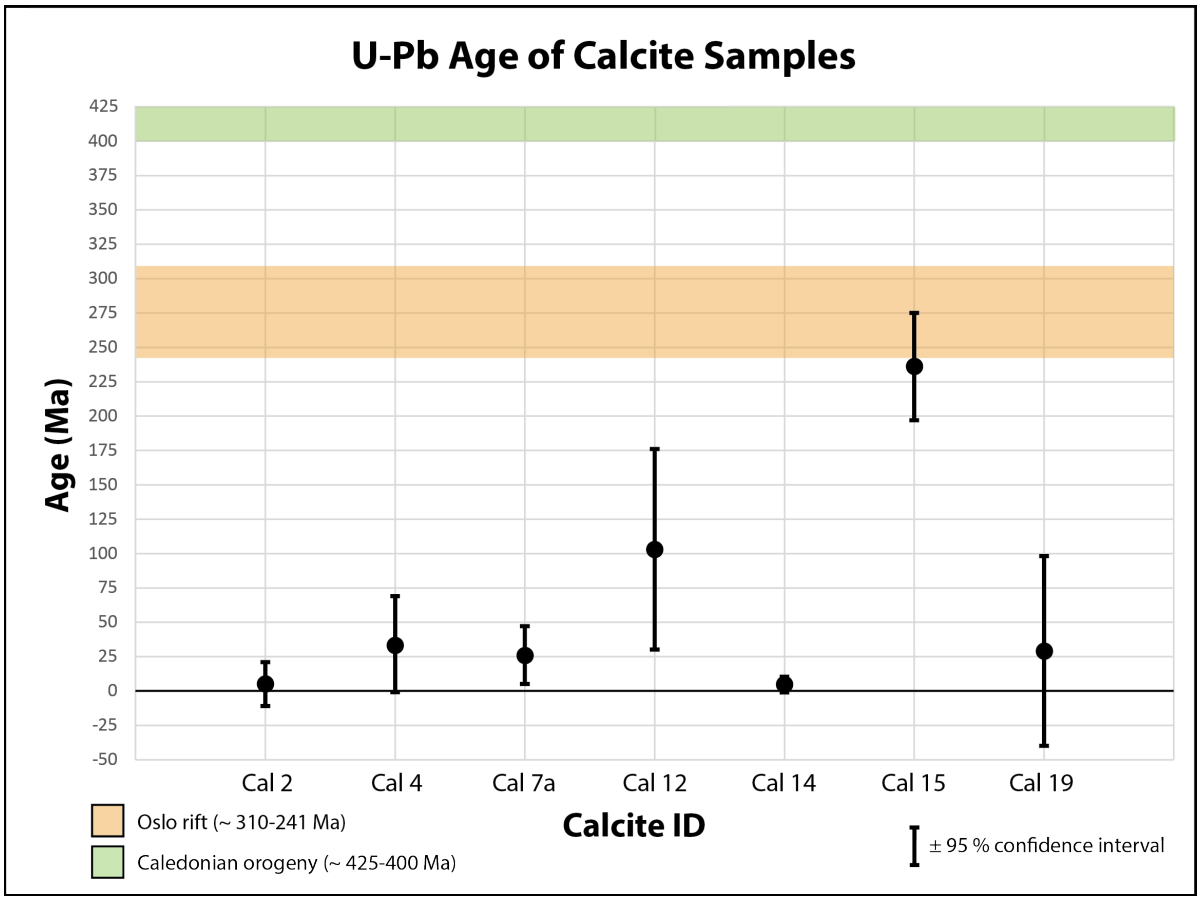

Figure 5.23: Scatter plot of U-Pb estimated age of calcite samples in this study. The aimed ages of the Caledonian orogeny and Permian rifting are highlighted. Only Cal 15 is within this range, with an estimated 95 % confidence age interval of 197 – 275 Ma.

Cal 13-, 14- and 15 were located in the Kalvsjøen Fm. nearby a strike/slip fault. Cal 13- and 14 were sampled directly from the same fault zone with slickensides oriented 01/028. Cal 13 was not datable, while Cal 14 indicated the youngest age of all samples with 4.6 Ma (± 5.7 Ma). Cal 15 was located just a few meters away from the fault zone. It was a vein with fiber growth measured at 06/074 (Figure 5.24). Despite poor counting statistics and very low U (<60 ppb) and radiogenic Pb concentrations, the age is deemed accurate within uncertainty. Its orientation and growth direction of fibers correlates with the Permian extension and opening of the Oslo Rift which was also the initial theory presented while in the field.

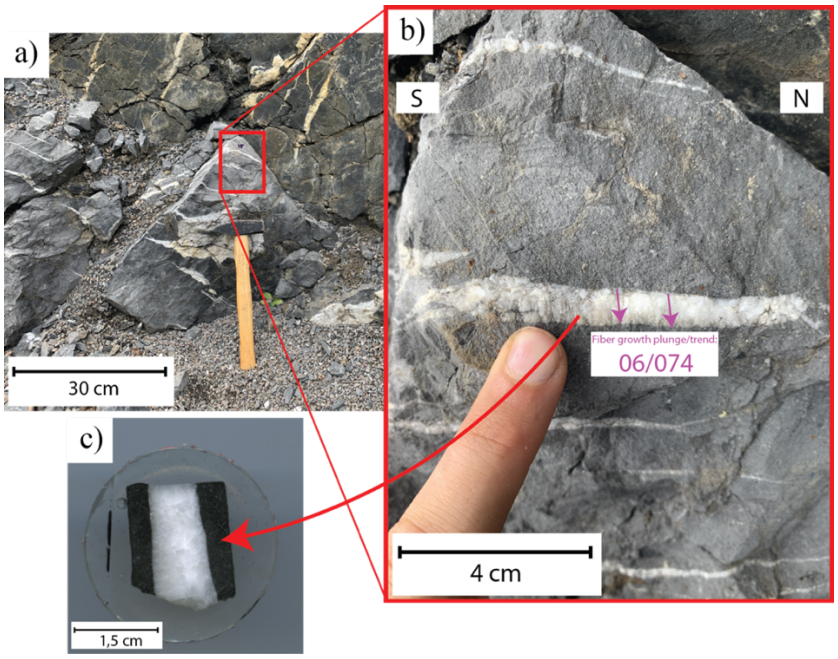

Figure 5.24: Cal 15. (a) Area from where Cal 15 was located in the Kalvsjøen Fm. Complex network of veins and precipitated calcite with a dominant N-S orientation. Loc.: 60.2966255, 10.5554227. (b) Close up image of Cal 15 with plunge/trend of fiber growth. (c) Prepared mount sent for analysis of Cal 15. Selected area of interest was parallel to fiber growth direction.

Observations and notes for remaining and younger samples

Cal 2- and 4 were precipitated calcite without any indication of direction of movement in sandstone dominated formations (Skøyen Gr. and Bruflat Fm. respectively). Cal 7 was located in the Bruflat Fm. but with clear indications of movement: on the sidewall of a large 3 m wide, N-S oriented, Permian intrusive with slickensides directly on sample oriented 54/023. In preparation it was split into 7a and 7b, where 7a was a surface sample and 7b was perpendicular to 7a, displaying a cross-section of the sample. Only 7a proved suitable for dating.

Cal 12 was collected in the Kalvsjøen Fm. in a reverse fault oriented 093/29. The sample had slickensides oriented 032/73, interpreted to be of Caledonian age. Cal 19 was the northernmost

datable sample, located in the Kirkerud Gr. It was small (1x3 cm) and collected in the same area as Cal 20- and 21. Slickensides indicated a 00/338 orientated movement.

These results inhabit large uncertainties with relatively young ages. To go in detail and further place them in a geological setting is outside of the scope of this thesis and should be done with care.

6 Discussion

The application of LiDAR data in bedrock mapping and the overall structural style and evolution of central and south Hadeland will be discussed in this chapter based on results from this study and other studies from the Oslo Region. Also, the results from the U-Pb dating are used for discussions on evolution of the area.

6.1 Applicability of LiDAR hillshade images in bedrock mapping

Hadeland is the perfect location to examine if LiDAR hillshade images can improve the accuracy and quality of bedrock maps in sedimentary successions. The difference between the Cambrian and mid-Ordovician strata and the overlying mid-Ordovician and Silurian strata clearly emerges. Sub-horizontal bedded layers, strongly deformed-, or highly soil and drift-covered areas might not exhibit a footprint on LiDAR data to be noticeably improved with increased efficiency. A thin-skinned foreland basin with competent and well defined folded and faulted stratigraphy appears on the LiDAR data in a different way. Hadeland holds all these features.

6.1.1 Why and where LiDAR data should be used in bedrock mapping

As mentioned earlier, an eye-catching observation when studying the LiDAR data covering central and south Hadeland is the prevalence of packages. Knowing the deformation history of the area and how geological structures are formed in a thin-skinned foreland basin, the LiDAR data resemble large scale folds with visible hinge points and disconformed sheets of thrusted sediments. The reasons why LiDAR data can be used in bedrock mapping at Hadeland are many, and some are more obvious than others. The local geology must contain heterogeneity to a degree where surficial processes sculpt the landscape with topographical differences in the terrain larger than the resolution of the LiDAR DTM, as also noted by Pavlis and Bruhn (2011). According to Scheiber et al. (2015), bedrock structures can, if present on the LiDAR data, reflect the surface expression of bedding, foliation, faults, fractures and fracture zones. Dip of bedding was therefore initially postulated to be important for the different units of strata to stand out from surrounding units and hence form geological structures visible on the LiDAR hillshade images.

However, after finishing the mapping process, a correlation between appearance on LiDAR data and degree of dip in measurements obtained in the field is found to be weaker than initially thought. A large portion of measurements, when viewed on top of LiDAR images, demonstrates that the general dip in an area cannot be uncovered by its appearance, as illustrated in Figure 6.1. To assume bedding direction based on LiDAR hillshade is not found favorable and can result in major confusions or misinterpretations. Changing of the azimuth of the shades in the hillshade image in a large degree also changes the "apparent" dip of the structures. This further rises the question if the LiDAR data can approve the quality of bedrock mapping when structures that appear on the LiDAR map for the most part does not conform with initial and "first glance" impressions of the structures.

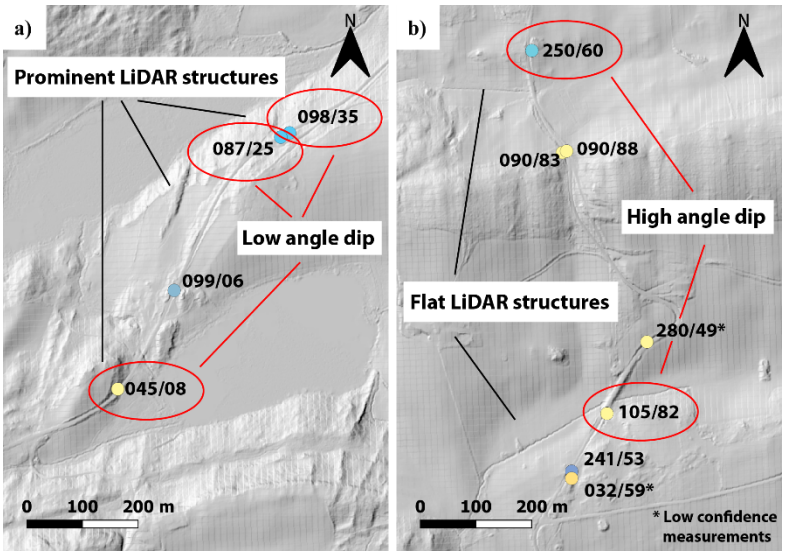

Figure 6.1: Comparison of two areas that reflects how LiDAR structures and bedding measurements not always correlates. (a) Prominent structures on LiDAR, but low angle dip of bedding measured in the field. (b) Flat structures on LiDAR, but relatively steeply dipping bedding measured in the field.

One major finding that indeed encourages LiDAR data to be applied in bedrock mapping is the correlation between hillshade structures and the observation of outcrops from different locations within the same package. In the aftermath, when all observations of different formations are imported and placed on top of the LiDAR data, it is ascertained that measurements within individual packages coincides well (see Figure 5.4). Notably, strike of bedding and identification of formations can to a high degree be correlated following the shadows produced by LiDAR hillshade images, while the general angle of dip varies more.

The limestones assigned in the Rytteråker Fm. is found to be the most consistent formation to base mapping on. Despite its thickness of ~50 m, which in comparison to its neighboring stratigraphic units in the Skøyen Gr. and the Vik/Ek Fm. is not great, when present in the field it functions as a reliable indicator for the general bedding in the area. If multiple localities with field measurements from the Rytteråker Fm. within the same package are obtained, they

definitely, without expectations, provide the most consistent bedding measurements out of all the formations. Some aspects that can explain why: The transition zone between the Skøyen Gr. and the Rytteråker Fm. is often shale rich, resulting in a deeper eroded zone with vegetation and trees in the fertile soil, as seen in Figure 6.2. This zone is notably less resistant to erosion than surrounding rocks, and will as a result emerge on the LiDAR data and provide for easier detection of formation boundaries, as can be seen in Figure 6.3.

Figure 6.2: One of many areas that exhibited a deeply eroded and highly vegetated zone in the transition zone between the Rytteråker Formation and the Skøyen Group. Position can be seen in Figure 6.3b. Loc.; 60.3196200, 10.4251739

Another reason for why the Rytteråker Fm. yields a dominant expression on the LiDAR is that it is often bordering to less resistant formations as the shale dominated Ek Fm. or areas covered in soils. These have, relative to the Rytteråker Fm., often flatter and homogeneous structures, leaving the Rytteråker Fm. to stand out as traceable.

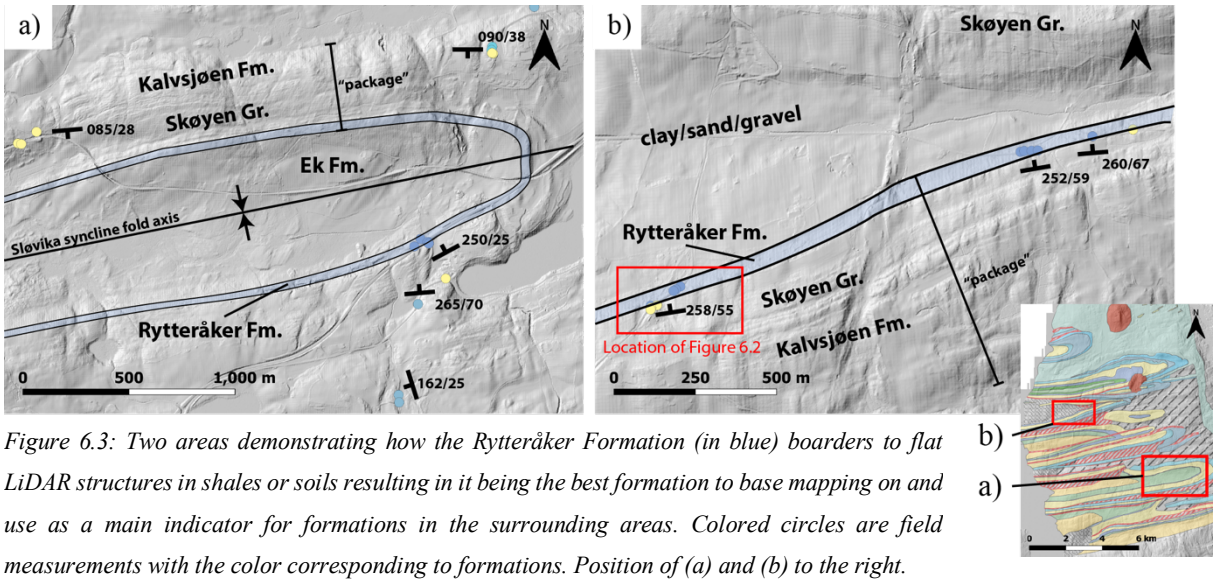

Figure 6.3: Two areas demonstrating how the Rytteråker Formation (in blue) boarders to flat LiDAR structures in shales or soils resulting in it being the best formation to base mapping on and use as a main indicator for formations in the surrounding areas. Colored circles are field measurements with the color corresponding to formations. Position of (a) and (b) to the right.

Interestingly, the Rytteråker Fm. is, as illustrated in Table 5.1, the formation which is second least accurate mapped in the existing NGU map (Owen et al., 2001) compared to the new map,

with an accuracy of 23 %. Considering that the Rytteråker Fm. is found to be the most consistent and easily mapped formation in this study, this finding clearly emerges the advantage of LiDAR.

Experience gained through the production of this map underlines the importance of traditional mapping methods, and to use LiDAR as a supporting tool for where final formation boundaries should be drawn. LiDAR cannot entirely replace field visits due to apparent bedding and appearance of different formations being highly variable (e.g. a shale or limestone dominated formation doesn't have a fingerprint appearance on the LiDAR hillshade images). In a highly drift-covered area like Hadeland, traditional mapping techniques have been proven by the map from Owen et al. (2001) to correctly identify the most prominent structures and formation boundaries. The map is a result of multiple geologists and revisions through decades, and as seen in Figure 5.1, its overall structural trends agrees well with the map produced in this thesis. However, as seen in Table 5.1, most formations have an area overlap that typically differs by more than 50 %. Details in formation tracing between outcrops and overall formation prevalence clearly benefit from structural trends highlighted by LiDAR hillshade images, which leaves the following conclusion: The main advantage of LiDAR is the significantly improved delineations of layer boundaries and structure tracing delineations over traditional mapping methods.

Identification of faults by LiDAR hillshade images

Another improvement in mapping by application of LiDAR hillshade images is its ability to trace fault zones between the more systematic packages and folds. Combined with observations from the field, fault zones and hence faults are determined with higher confidence and fewer uncertainties than earlier. An example demonstrating the importance of a combination of LiDAR and field measurement is the thrust identified as F13 (Figure 5.15). The thrust accommodates for displacement of more than 400 m and is therefore major in calculations of Caledonian shortening. Strictly using LiDAR images, this fault would probably not have been interpreted due to poor exposure in its immediate vicinity. The same goes with the existing map and associated cross-section, where the F13-fault accommodates close to zero displacement. Using LiDAR and field observations, vital geological structures on a mapping scale of 1:50 000 can therefore be identified and mapped.

Permian extensional structures and normal faults have been mapped out at Hadeland for the first time at this scale using LiDAR images. Creation of lineament maps, similar to the map in Figure 5.19a, is a commonly used technique (Gabrielsen et al., 2002; Scheiber et al., 2015) where LiDAR images is crucial in order to identify faults that are not visible on today's surface. At Hadeland, these faults would not be possible to identify without LiDAR.

6.1.2 Suggested method for implementation of LiDAR data in bedrock mapping

Based on the experience gathered in this thesis, the following workflow is recommended in the application of LiDAR to bedrock mapping, see Figure 6.4. Detailed field work should be conducted in advance of extensive work with mapping solely based on LiDAR data. This is because field observations are found to still function as the main basis in the mapping process, while LiDAR works as an exceptional tool to trace formation boundaries and faults with high confidence combined with observations from the field.

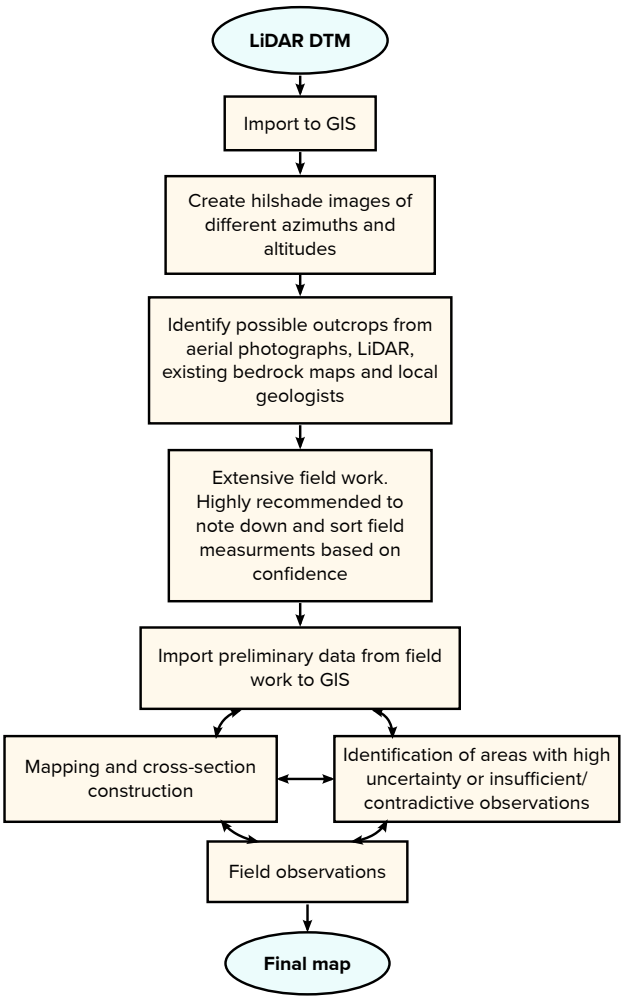

Figure 6.4: Suggested workflow for appliance of LiDAR hillshade images in bedrock mapping from this study.

After initial and extensive field work, mapping and new field observations should be an iterative process with feedback. This workflow will drastically increase mapping quality and shorten field duration. With experience and future studies that recognizes the great potential as well as the problems of LiDAR in bedrock mapping, especially in highly drift-covered folded and faulted foreland basins, the preliminary geological understanding and evolution of the area can and should be revised. Finings in this study justifies that available LiDAR data should always be consulted when mapping out the bedrock in an area to examine its potential and further utilization.

The postulated approach from this study differs from Pavlis and Bruhn (2011) who emphasize that field work should be conducted after initial and extensive work with LiDAR data, and that a preliminary geological map should be constructed prior to arrival in the field. A major difference between this study and the study of Pavlis and Bruhn (2011) is the study area and associating local geology. In their study, stratigraphic formations are not mapped, only the bedrock structure which changes the role of LiDAR hillshades compared to this study. If the mere purpose of mapping is to identify structures, LiDAR can be the main tool to reveal areas covered by soils. But, if formations are to be mapped, LiDAR will function more as a supportive tool for placement of formation boundaries and fault tracing, combined with traditional field work. Hence, the suggested workflow is directly connected to the specific geology in central and south Hadeland. Studies in other regions and with other purposes might benefit from slight adjustments in workflow.

6.2 Overall structural style

This subchapter discusses the geology of central and south Hadeland using findings in this study, earlier studies from the area and other studies conducted in the Oslo Region.

6.2.1 Caledonian compressional structures

Compressional structures, mainly folds and thrust faults at different scales, are found to be the dominating structures at Hadeland. This is reflected in the new map and associating cross-section, as well as observations and measurements of third order structures in the field. If folds and faults of different orders are produced in the same deformation event, they usually have a coaxial or nearly coaxial orientation (Groshong Jr, 2006). The main direction of tectonic transport recognized in this study is towards S-SSE (175 degrees) based on analyzes of orientation for fold axes and faults. This is in line with tectonic transport of the Osen-Røa thrust sheet (e.g. Morley, 1983; Bruton et al., 2010; Sippel et al., 2010). While fold axes measured in the field coincides well with the orientation of higher order folds, the thrusts measured in the field (seen in Figure 5.18) deviates, overall, substantially from the orientation of the first- and second order thrusts with a dominating ESE dipping orientation. Difficulties in obtaining accurate measurements in the field of these thrusts is a probable explanation for this, and, as noted in Chapter 5, most of the outcrops in the field are oriented parallel to the strike of the large-scale thrusts. This can lead to several thrusts being overseen, and chances are that thrusts at this scale accommodates for a substantially larger displacement than indications provided by

measurements (not calculated in this study). Folds at scale larger than single outcrops, but not sizable to be displayed in the main profile covering central and south Hadeland (12.9 km N-S), with amplitudes in the 50-200 m range is found difficult to pinpoint due to poor exposure percentages. Measurements on the map from this study indicates that these "intermediate sized" folds accommodate an admissible amount of shortening, but only in local subareas.

The frequency of thrusts that can be identified in the field is distinctly larger than the frequency of folds, but calculations of total displacement is found not desirable to assume due to throw and heave being immeasurable. Still, retrospectively, it would be possible to calculate a mean displacement based on the few measurable thrusts in the area, and then multiply with number of identified thrusts. For this to be desirable, detailed restrictions for thrusts identifications in central and south Hadeland must be made in order to consistently distinguish between bedding and thrusts.

6.2.2 Large scale structural differences in central and south Hadeland

The difference in strain between northern and southern parts of Hadeland is a result of lateral and not vertical changes; the formations exposed in the north is situated stratigraphically lower compared to further south. The Cambro and mid-Ordovician units are shale dominated, and their competence is low compared to the mid-Ordovician and Silurian units. In order to explain how the difference in structural styles between the two areas are formed by the same deformation event, the bedding-parallel detachment (from Morley, 1983; 1987b) have also been postulated in this study (as illustrated in main cross-section A-A'). Detailed analyzes of the strain accommodated by folds and thrusts within the mid-Ordovician and Silurian sequence carried out in this study also reflect some differences in structural style between the northernmost- and southernmost parts of the study area. However, not to the same extent as between north Hadeland and central/south Hadeland.

Southwards and westwards in the study area equals to moving stratigraphically higher. The Bruflat Fm., which is the youngest exposed formation in the study area, is more dominating in outcrops close to Randsfjorden and Ringerike. The general plunge of five large scale synclines of approximately four degrees towards WSW (Figure 5.8) can explain the reason for this. Even

when the areas further east are located at a higher topographic level, the tilt of the area and later erosion exposes younger formations further west (Figure 6.5). The majority of large scale structures are plunging towards WSW, inferring that tilting of Hadeland occurred after Caledonian compression, most probably in stage 2 and 3 (between 300 Ma and 280 Ma) in Permian with the creation of the Oslo Rift and a graben structure. A general plunge of fold axis in the Tyrifjord area towards SW is also observed by Vlieg (2015), which can be postulated to be a result of the same mechanisms.

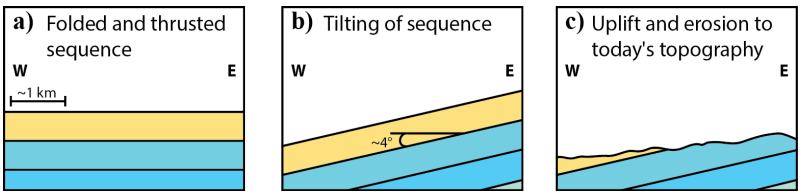

Figure 6.5: Schematic illustration to demonstrate why younger formations is located westwards at Hadeland. (a) The folded and thrusted stratigraphic sequence after the Caledonides. (b) Tilting of sequence resulting in synclines plunging approximately four degrees. (c) Uplift and erosion to today's topography. Note that the relation between the processes might have interfered with each other and that this is a simplified illustration.

The general structural trend of central and south Hadeland can be inferred by combining the findings in Figure 5.6 and Figure 5.15. They show that strain is decreasing when moving southwards, which is in line with the general lateral variations in deformation style in the Oslo Region as illustrated by Morley (1987a) in the lower Ordovician sequences (Figure 6.6). Morley notes that the lateral changes in deformation style is far greater in the Cambrian to mid-Ordovician units than in the mid-Ordovician to Silurian units. Still, the information compiled from this study reflects that the lateral differences in deformation might also be valid within the current area (summed up in Figure 6.7), at a smaller 1:50 000 scale.

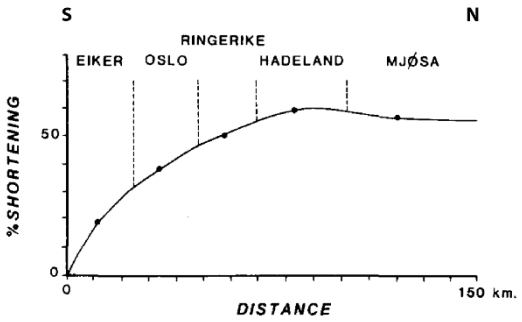

Figure 6.6: Average amount of shortening in the lower Ordovician for each district from Morley (1987a) shows a general decrease in strain towards south.

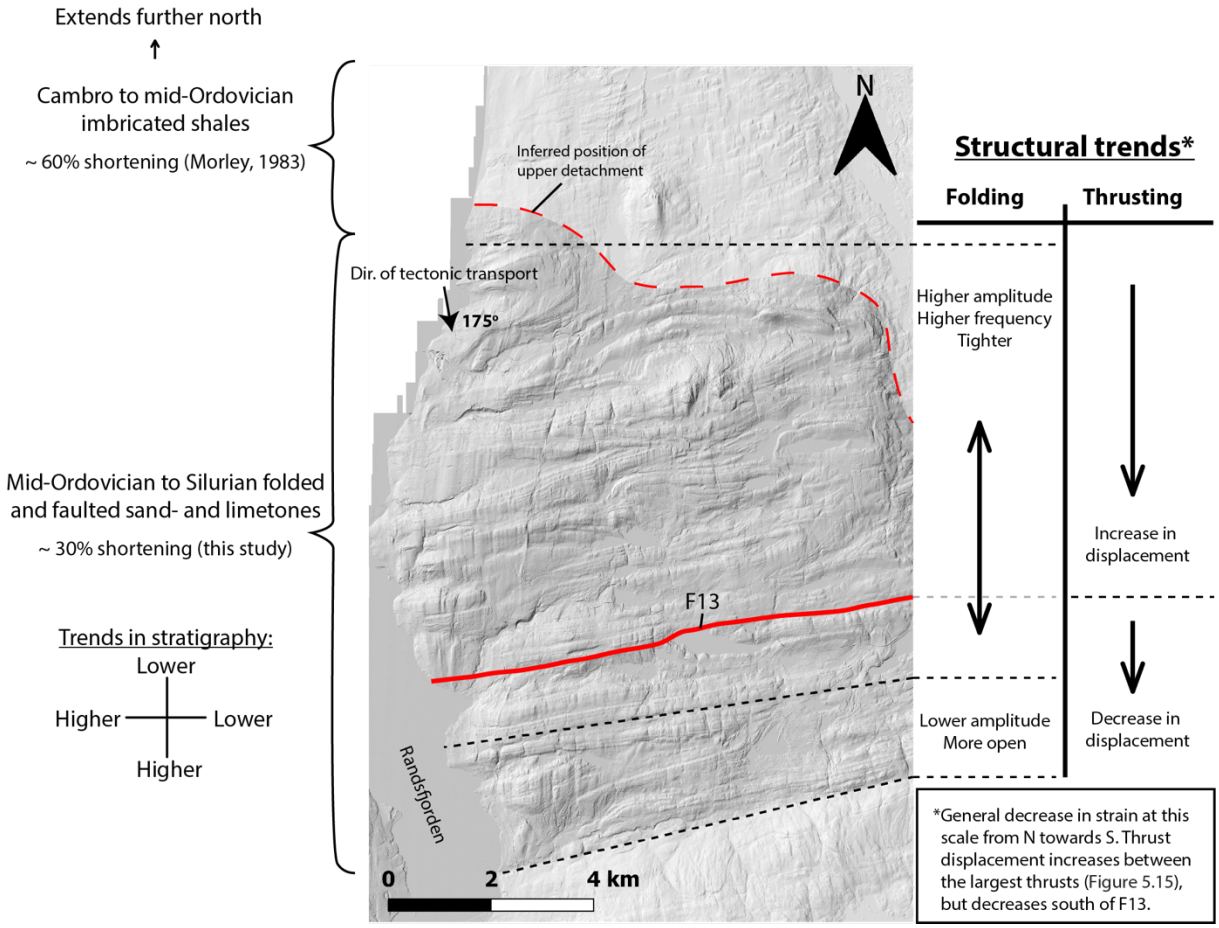

Figure 6.7: Structural trends within central and south Hadeland generalized from large scale structures in this thesis. F13 (forethrust 13 from Figure 5.15) accommodates the larges displacement. South of F13, the thrust displacement and fold amplitude drastically decreases.

The reason why strain decreases southwards narrows down to multiple reasons, but the most important might be the Ringerike Sandstone. It is situated stratigraphically higher than the Bruflat Fm., and is completely eroded away at Hadeland. Under the main stages of deformation it capped the sequence with a thickness up to 1250 m (Bruton et al., 2010). The strengthening effect of the overburden and competent sandstones limited strain in formations in direct vicinity of it. This combined with an increase in competent formations (exposed) southwards, might explain some of the differences in strain. Stress building up and at one point releasing in F13 can also be a possible contributor to difference in thrust displacement, but at this point, these factors and their relative importance remain uncertain. The main finding is that the large scale structures in the mid-Ordovician to Silurian strata at Hadeland reflects the general variations in structural style from north to south in the Oslo Region as discussed by Bruton et al. (2010) and Morley (1983; 1987a).

Structural differences from field observations in outcrop scale

Based on observations from the field it can be postulated that faults, predominantly fore- and backthrusts, occur more commonly in the limestone dominated formation of Kalvjsøen and the more shale rich Gamme-, Kjørrven and Lunner Fm. compared to remaining formations. To confirm this, a more detailed and comprehensive study focusing on faults should be conducted.

When traveling across Hadeland in search of bedding measurements for mapping, structural observations was not made to a desired level, making it difficult to synthesize and assemble concluding remarks on the geological structures at this scale. Still, one important concluding remark is that the formations display large and notable differences depending on geographic position within the studied area. Great lateral changes at this scale were observed, but not in a pattern allowing for trends to be perceived. Each formation has its own structural and sedimentological fingerprint according to outcrop and position of outcrop on a larger scale. E.g., a relatively shale dominated unit like the Ek Fm. can be close to unstrained in areas within packages (generally, not always), but highly strained with folds and faults closer to the fault zones marked at the 1:50 000 map. The same goes for lime- and sandstone dominated formations. A systemized and comprehensive study is recommended to be conducted, allowing for comparisons of structures at different scales within a concentrated and fairly well understood area.

6.3 Structural synthesis

Orientation of bedding planes

Bedding measurements gathered in central and south Hadeland can be seen in Figure 6.9. The poles show a fairly wide scatter, but a consistent E-W dominating direction of strike. Measurements from this study and Morley (1987a; 1987b) both indicate that folding, relatively broad and open, is the dominating deformation style. The poles are relatively evenly distributed in the N-S direction as opposed to e.g. measurements from north Hadeland (Figure 6.8), where a cluster of poles in the southern half is dominating, reflecting more of a hinterland dominating dip direction in the imbricated successions.

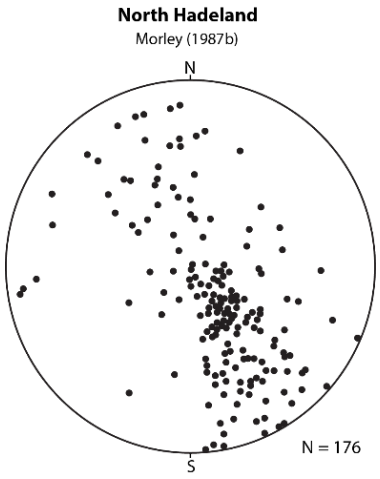

Figure 6.8: Bedding in north Hadeland, re-digitalized from Morley (1987b).

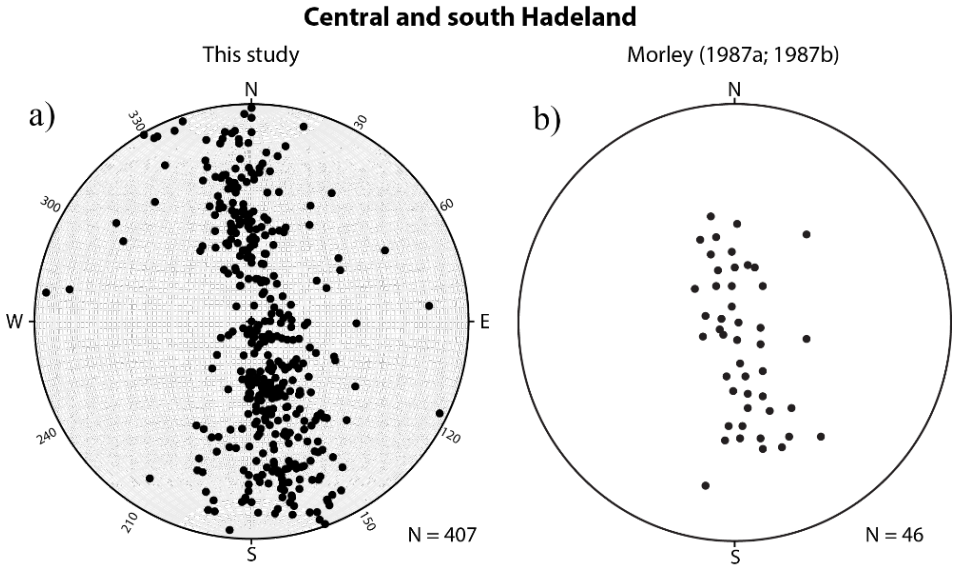

Figure 6.9: Poles to bedding in central and south Hadeland. (a) Measurements from this study. (b) Measurements re-digitalized from Morley (1987a; 1987b). The two studies complement each other well.

Still, when studied in detail, bedding in central and southern Hadeland is somewhat clustered on the southern half of the stereonet in measurements from both studies. The dominance is not as governing as for north Hadeland, but with 61 % and 65 % (this study and Morley respectively) of the poles in the southern half of the stereonet, the large scale forethrusts are influencing the overall hinterland dominated dip direction of outcrops when quantified.

When comparing bedding measurements from north Hadeland with central and south Hadeland, the difference in direction of transport, orientation, and structural style clearly emerges. The bedding parallel structural detachment postulated by Morley (1983) is found reasonable to retain. In the case of more W and E oriented structures in central and south Hadeland, the nature of the detachment could probably be questioned further. But, with such great differences in overall bedding-, thrust- and fold axis orientations, the hypothesis of a detachment is strengthened after findings in this thesis. Additional information for discussion on the development and architecture of the detachment, and on foreland vs. hinterland directed transported hangingwall (see Morley (1987a) for further reading) is not obtained in this thesis. A hinterland directed detachment is postulated in this thesis and from Morley (1987a) to be preferred, even though it cannot be confirmed or observed in the field. This is mainly due to lack of evidence of a large ramp through the Silurian sequence which would be needed to explain a foreland directed upper detachment.

Backthrusts

Backthrusts are not common in the mid-Ordovician and Silurian strata at Hadeland. However, multiple other studies in the Oslo Region notes a higher abundance of backthrusts than previously though (e.g. Hjelseth, 2010; Vlieg, 2015; Broek, 2015; Weekenstroo, 2015). All these studies are from areas south of Hadeland, and hence often stratigraphically higher. Analogue models by Vlieg (2015), Broek (2015) and Weekenstroo (2015) shows a high prevalence of backthrusting in some scenarios, especially in higher parts of the stratigraphy. Broek (2015) stated that backthrusting in the Tyrifjord area could be a result of the highly competent strata not being able to accommodate for the shortening, resulting in backthrusts to put up with movement along the ramp fault. They also note that the backthrusting seems to die out below the Ringerike Gr. and that backthrusts nucleates from second order thrust faults higher in the stratigraphy (Vlieg, 2015; Broek, 2015).

Smit et al. (2003) discusses the brittle-ductile coupling between layers in thrust wedges by performing a set of models where the variations in relative strength between brittle and ductile layers can be controlled. This is done by changing the basal wedge angle and shortening rate. In their experiments, backthrusts were always developed in strongly decoupled parts of the wedge. They also concluded that an overall weak brittle-ductile coupling (high wedge-angle and low shortening rate) display a dominant backward thrusting sequence. Opposed to this, an intermediate to high brittle-ductile coupling (low wedge-angle and high shortening rate) results in a regular and frontward-oriented thrusting sequence. Comparing these results with findings in this study, it can be postulated that the Hadeland area was situated in a part of the thrust wedge with a relatively low wedge-angle and high shortening rate, which can be one of multiple reasons for lack of backthrusts in Hadeland.

All in all, absence of backthrusting in the mid-Ordovician and Silurian strata at Hadeland agrees well with observations from studies southward in the Oslo Region. The shortening has been able to be accommodated in folds and forethrusts in this part of the succession, and the brittle-ductile coupling was probably high.

Caledonian shortening

Morley (1983; 1986; 1987a) have studied the Caledonian shortening of sediments in the Oslo Region in detail. He is, as far as known, the most recent geologist to publish regional calculations on amount of Caledonian shortening from the area. For the mid-Ordovician and

Silurian successions at Hadeland, he calculated an average shortening of 29 % (see Table 6.1). This coincides well with calculations in this study which indicates a shortening percentage of 30 % (Figure 5.7). However, Morley further notes that the successions in central and south Hadeland are deformed by broad and open folds, and that thrusting does not apparently contribute a significant amount to the total shortening. Additionally, he states that thrusts are rare, and that most of the faults in the area have high angle and small displacement of a few meters (Morley, 1983). Størmer (1943) shares a lot of the same opinions as Morley, stating that fault zones and possible thrust faults is "in short supply" in the area. He underlines that the geology of central and south Hadeland is folded, and hence does not need to hold thrust faults.

Table 6.1: Variation in average shortening percentage in areas from the Oslo Region. Data from Morley (1987a).

	S ←				→ N	
Area:	**Eiker**	**Oslo**	**N. Ringerike**	**Hadeland**	**S. Mjøsa**	**N. Mjøsa**
Avg. shortening % (e)						
Lower Ordovician	15	37	50	60	55	60
Lower Silurian	15	27	?	29	28	(Eocambrian)

Detailed mapping with tremendous support from LiDAR data in this study reveal a different view on thrusts in central and south Hadeland. The structures on the bare-earth LiDAR hillshade map (e.g. Figure 5.2a and Figure 5.15a), display a highly thrusted as well as folded sequence. Calculations also indicate that displacement accommodated by thrusting is responsible for 31 % of total shortening, which is a significant amount. It was the relationship between LiDAR data and field observations that made it possible to trace fault zones with high certainty. Without LiDAR, these zones would probably be more debatable or even not mapped/detected at all. Hence, it is easy to recognize the interpretation done by Størmer (1943) and Morley (1983), but it is also suggested that future studies undertake the importance of forethrusts in the area. Other areas within the Oslo Region with mid-Ordovician and Silurian sediments are also presumably more thrust-dominated than presumed today if the upper detachment follows north and southwards, isolating the sediments above the Kirkerud Gr. and below the Ringerike Sandstones as one unit with shared structural elements. Still, differences between the hinterland and foreland are to be expected.

The interaction and relationship between folds and faults through the evolution of the area is outside the scope of this thesis to discuss, but fault-propagation folds followed by a break-

forward sequence (Figure 6.10a) and/or break thrusts in folding of relatively competent units (Figure 6.10b) are two important evolutionary structures in this often complex relationship that should be disputed. The latter was proposed by Morley (1994) to be important in the Cambrian to mid-Ordovician sequence in the Oslo Region, and in both cases the thrust development is synchronous or post to folding.

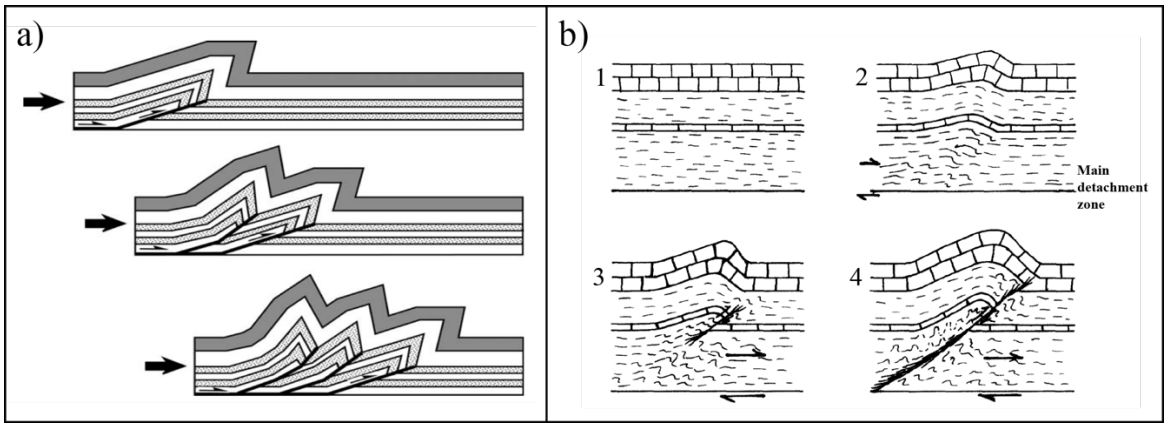

Figure 6.10: Structures proposed to be relevant for discussion of fold and faults relations in the Oslo Region and hence also central and south Hadeland. (a) Development of fault-propagation folds followed by a break forward sequence illustrated by Mitra (1990) and modified by Poblet and Lisle (2011). (b) Evolution of break thrust after Morley (1994) where the thrust propagates downwards from a competent layer like the Huk Formation to the main detachment horizon.

6.3.1 Significant uncertainties with cross-section and estimates of shortening

Cross-section construction and estimates of bulk shortening in a highly drift-covered and poorly exposed area where about 90 % of outcrops are related to road cuttings has several uncertainties that should be announced.

Mapping of stratigraphy at Hadeland is challenging due to etc. the detailed formation division based on paleontological features. The different formations show great variation in local thickness. Sedimentation rates in particular depositional conditions, syn-depositional folding and thrusting, followed by Permian rifting with volcanic plugs and dikes have modified the thickness of formations at local scales. These variations are often observed within areas situated 50 m apart, and thickness presented in existing literature should be taken with reservation for errors. As noted earlier, the Rytteråker Fm. was found to be a consistent formation to base mapping on, and combined with LiDAR data, local outcrop findings are needed to be overridden by the stratigraphic pattern reveled by high confidence strike/dip and formation measurements. This simplifies the existing bedrock map, but is also regarded as to increase its accuracy.

The main cross-section (in Figure 5.6) was constructed at a 1:1 scale. Hence, the vertical and horizontal scale are similar. The main advantage with this is that the dip seen on the section is corresponding to the true dip measured in the field. This resulted in a total thickness of the sediments between the Kirkerud Gr. and the Bruflat Fm. to reach upwards of 800 m, with the bottom of the Kirkerud Gr. at depths of 450 meters under mean sea level. To rectify this error, only the height of today's topography was noted on the final cross-section. This solution does not make the section perfect, and it points out major errors and uncertainties that are linked to construction of such sections.

The contact between the Precambrian basement and the Alum shales is detectable in the area close to Jarenvannet (R. Knarud, personal communication, August 16, 2021) at a height of 200 m.a.s.l. A total thickness of the sediments reaching 1000 m in e.g. the area of Buhammeren (450 m.a.s.l) would therefore be deemed highly implausible. Thicknesses of formations in the area, as well as in the Oslo Region, might have been measured in stacked tectonic units, not accounting for overthrusting. Another and probably more plausible explanation is that the few outcrops on the surface today, in reality, cannot be used to reveal the full and undeniable truth of the deformation history and structures under the surface. Still, attempts have to be made, and in lack of superior alternatives, cross-sections and under-ground assumptions have to be constructed to the best of our ability in order to gain information and further develop our geological understanding of the area.

The amount of Caledonian shortening achieved by folding and thrusting were calculated solely based on mapping and the associated cross-section in this thesis. Taking into account the uncertainties in the cross-section as already discussed above, several other deformation mechanisms contribute to the total strain in central and south Hadeland, as also noted by Morley (1986). He calculated shortening of the Asker-Bærum area by ET (total natural strain) which is calculated by adding the amount of shortening from buckling (folds) and contractional faults, but also two additional factors: layer parallel shortening and pressure-solution (after Simon and Gray (1982)). Morley found that the lower Silurian in the area had a total natural strain of 26 % shortening, where about 6 % of the total shortening were caused by layer parallel shortening, and 18 % by pressure-solution. Neither layer parallel shortening nor pressure-solution have been taken into account for when calculating the shortening in this thesis. Outcrops displaying layer parallel shortening were identified (see Figure 5.9 and Figure 5.16) both with and without visible thrusts, but Morley's calculations on amount of layer parallel shortening are based

indirectly on measurements of pressure-solution and thrust wedging, and found unfavorable to calculate with higher accuracy in this thesis.

Koyi et al. (2004) also illustrated the importance of layer parallel shortening by restoring sections from the Spanish Pyrenees and model profiles. In the eastern parts of the Spanish Pyrenees, 16-23 % of shortening was accommodated by layer parallel shortening, and only 6-10 % by folding. The study notes that shortening by layer parallel shortening is three times greater in models with high basal friction compared to low basal friction, and when sand is embedded in a viscous layer, the layer accommodates all shortening in folding with no significant layer parallel shortening. However, the relative level of basal friction compared to the Oslo Region is not known, but the study highlights that layer parallel shortening should be accounted for in contractional areas.

Combining this with the earlier discussed folding at scales too large for outcrops but too small to reveal at the present scale of mapping at 1:50 000, a total shortening of 30 % in the mid-Ordovician and Silurian succession at Hadeland should be regarded as a minimum. By utilizing the numbers given by Morley (1986), where 6 % of shortening is accommodated in layer parallel shortening and 18 % by pressure-solution, a combined shortening of 24 % (6 % + 18 %) is then added to the calculated 30 % shortening accommodated in folding and thrusting of the sediments in central and south Hadeland in this thesis. This gives a total of 37.2 % shortening. By adding the unknown amount of shortening provided by intermediate sized folding, Caledonian shortening is proposed to be in the range of 38-45 % in central and south Hadeland. This indicates that the percentage of shortening in the mid-Ordovician and Silurian strata at Hadeland is higher than previously assumed, and that the differences in shortening between the north and the south of the Oslo Region is larger than earlier estimated.

6.4 Structural evolution

Earlier thesis's in the Oslo Region, e.g. from Hjelseth (2010), Repshus (2012) and Dehli (2012), recognizes the structural evolution of their areas in detail with different phases of deformation and relative age of structures. All of these are located south of Hadeland, and even if the focus of this thesis has been on mapping of larger scale structures, an agreement is found that the structural development of the Hadeland area is a result of one progressive event, the Scandian phase, with initial folding followed by large first- and second order forethrusts, and later a few

backthrusts. Eventually, Permian extension have resulted in large scale normal faults, identified on the LiDAR data, and approximately four degrees of tilting of the entire succession either syn- or post Permian rifting (this study).

Morley (1987b) stated that deformation in Hadeland is thought to be of Caledonian age, possibly in the middle to late Devonian boundary (about 382 Ma). This corresponds well with e.g. Henningsmoen and Dons (1978), which noted that the Cambro-Silurian strata in the northern and central parts of the Oslo Region most probably were folded during a late phase of the Caledonian orogeny, in Devonian times.

To identify higher order folds and thrusts with precipitated calcite and slickensides as indication for direction of movement, and hence age of the structures, was aimed in this thesis to determine the absolute age and development of the structures at Hadeland. U-Pb dating of calcites in the Oslo Region have been attempted earlier (R. Knarud, personal communication, March 17, 2022) without desirable results. Unfortunately, results received from U-Pb dating in this study cannot be used as a foundation to derive final ages and discuss the evolution of the area as well as the Oslo Region as aimed. Yet, the results demonstrate that the quality and accuracy of U-Pb dating of calcites are highly variable. Six out of seven dated samples indicated relatively young ages (within uncertainties), which probably is caused by reactivation of earlier developed faults and fractures. Only Cal 15 was dated to possibly be of late Permian age (Figure 5.23). As this imply that some calcites in the Hadeland area are from one of the two main stages of deformation, it also emphasizes the complexity of the system. A large portion of movement indicated by slickensides and high order thrusts is a result of reactivation and local deformation within the latest of 35 Ma.

To draw any conclusive remarks from the U-Pb dating in this study is not reasonable. Future studies that aim to absolute date deformation events in the Oslo Region are recommended to obtain a larger number of samples. Only 22 % of the prepared and sent mounts were datable in this study, mainly due to low U concentrations. Elsewhere in the region, the percent of datable samples might be higher, while uncertainties can be lower. This would ensure data that is imperative to fully understand the structural evolution of Hadeland and the Oslo Region. Although U-Pb dating results in this study were relatively inconclusive, they underline that the method should not be disregarded in the Oslo Region.

7 Conclusion and further work

This chapter summarizes the main contributions of this study from the new, revised bedrock map, and discussions on geological structures and evolution of central and south Hadeland. Furthermore, the chapter leaves suggestions for future research based on the conclusions gathered in the present work.

7.1 Concluding remarks

The presented results and discussion have led to the following conclusions of this thesis:

- LiDAR DTM and hillshade images is advised to be utilized to a greater extend in the creation of bedrock maps. A suggested workflow is presented in Figure 6.4, which easily improves placement of exact layer boundaries and fault traces in highly drift-covered areas like Hadeland. LiDAR hillshade images should however not replace traditional mapping methods, but function as an additional tool.
- The structural style of central and south Hadeland is dominated by Caledonian folding and thrusting, both on a larger mapping scale and on outcrop scale, with a uniform and dominant tectonic transport direction of 175 degrees (NNW-SSE).
- From the updated and improved map, a 12.9 km long cross-section at a 1:1 scale has been created. Calculations on Caledonian deformation indicates a total of 30 % shortening due to folding and thrusting which correlates with existing and regional estimates. However, 31 % of shortening is caused by thrusting which is considerably more than assumed by earlier published work. The findings are likely due to the improved delineations introduced by LiDAR hillshade in mapping.
- The calculated Caledonian shortening of 31 % should be regarded as a minimum. If shortening caused by layer parallel shortening, pressure-solution and intermediate sized folding is included, the total shortening is probably in the range of 38-45 %.
- Large scale structures in the mid-Ordovician to Silurian strata at Hadeland reflects the general variations in structural style from north to south in the Oslo Region. Amount of strain decreases southwards.
- U-Pb dating results of calcites to date the deformational events of the Caledonian orogeny and Permian rifting at Hadeland were inconclusive. Out of the 34 samples, only 22 % had sufficient U/Pb relations, and in general, low U concentrations prevented for overall desired results. Five out of seven calculated ages were younger than 35 Ma, interpreted to be caused by reactivation of earlier developed faults and fractures.

- The structural development of the Hadeland area is a result of one progressive event, the Scandian phase, with initial folding followed by large first- and second order forethrusts, and later, less common NNW directed backthrusts. Eventually, Permian extension have resulted in large scale normal faults, identified on the LiDAR data, and approximately four degrees of tilting of the entire succession syn- or post Permian rifting.

7.2 Suggestions for further work

Suggestions for further work that should be considered to improve the understanding of the geology at Hadeland and in the Oslo Region:

- Collection of seismic data and/or drilling cores in an attempt to determine the total thickness of the sedimentary successions throughout the Hadeland area could reveal new and possibly crucial details for updates to the existing knowledge of depth to detachment and complexity of the deformation history.
- Conduct a quantitative study on the relation between LiDAR-based versus traditional mapping methods to recognize how they both ameliorate and conflict each other.
- Detailed structural analysis of outcrop scale structures in central and south Hadeland would allow for comparison to large scale structures from this study as well as other areas in the Oslo Region. Thrust displacement and quantifying of structures in relation to mapped fault zones and their relationship could strengthen our understanding of thin-skinned foreland basin development.
- Estimates on shortening caused by intermediate sized folding (larger than outcrop-, smaller than 1:50 000 mapping scale) would yield a more precise estimate on Caledonian deformation.
- New and a more widespread collection of calcite samples throughout the Oslo Region in an attempt to absolute date the Scandian event and Permian extension with U-Pb is suggested. The method should not be disregarded in the Oslo Region after this study, but rather upscaled to secure a significant sample size before drawing concluding remarks.

References

Alania, V., Chabukiani, A., Chagelishvili, R., Enukidze, O., Gogrichiani, K., Razmadze, A. & Tsereteli, N. 2017. Growth structures, piggy-back basins and growth strata of the Georgian part of the Kura foreland fold–thrust belt: implications for Late Alpine kinematic evolution. *Geological Society, London, Special Publications,* 428**,** 171-185.

Allmendinger, R. W. 2021. *Stereonet v. 11.3.5* [Online]. Available: https://www.rickallmendinger.net/stereonet [Accessed 23.09.2021].

Allmendinger, R. W., Cardozo, N. & Fisher, D. M. 2011. *Structural geology algorithms: Vectors and tensors*, Cambridge University Press.

Ballo, E. G., Augland, L. E., Hammer, Ø. & Svensen, H. H. 2019. A new age model for the Ordovician (Sandbian) K-bentonites in Oslo, Norway. *Palaeogeography, Palaeoclimatology, Palaeoecology,* 520**,** 203-213.

Bates, R. L. & Jackson, J. A. 1987. Glossary of geology.

Berry, W. B. & Boucot, A. J. 1973. Glacio-eustatic control of Late Ordovician–Early Silurian platform sedimentation and faunal changes. *Geological Society of America Bulletin,* 84**,** 275-284.

Bingen, B., Belousova, E. & Griffin, W. 2011. Neoproterozoic recycling of the Sveconorwegian orogenic belt: Detrital-zircon data from the Sparagmite basins in the Scandinavian Caledonides. *Precambrian Research,* 189**,** 347-367.

Bjørlykke, A. 2017. *Skyvedekkenes nordiske far* [Online]. GEO365.no. Available: https://geo365.no/aktuelt/alfred-elis-tornebohm-skyvedekkenes-nordiske-far/ [Accessed 27.08.2021].

Bjørlykke, K. 1974. *Depositional history and geochemical composition of Lower Palaeozoic epicontinental sediments from the Oslo Region*, Universitetsforlaget.

Bjørlykke, K. n.d. A short introduction to the geology around the inner part of the Oslo fjord.

Braithwaite, C. J. & Heath, R. A. 1996. Regional geometry, petrographic variation, and origins of Upper Ordovician dolomites in Hadeland, Norway. *Norsk Geologisk Tidsskrift,* 76**,** 63-74.

Braithwaite, C. J., Owen, A. W. & Heath, R. A. 1995. Sedimentological changes across the Ordovician-Silurian boundary in Hadeland and their implications for regional patterns of deposition in the Oslo Region. *Norsk Geologisk Tidsskrift,* 75**,** 199-218.

Brenchley, P. J. & Newall, G. 1975. The stratigraphy of the upper Ordovician Stage 5 in the Oslo–Asker district, Norway. *Norsk Geologisk Tidsskrift,* 55**,** 243-275.

Brenchley, P. J. & Newall, G. 1977. The significance of contorted bedding in upper Ordovician sediments of the Oslo region, Norway. *Journal of Sedimentary Research,* 47**,** 819-833.

Brenchley, P. J. & Newall, G. 1980. A facies analysis of Upper Ordovician regressive sequences in the Oslo region, Norway—a record of glacio-eustatic changes. *Palaeogeography, Palaeoclimatology, Palaeoecology,* 31**,** 1-38.

Broek, J. V. D. 2015. *Caledonian deformation in the Oslo Region, updating the regional tectonic model.* MSc, University of Utrecht.

Bruton, D. L., Gabrielsen, R. H. & Larsen, B. T. 2010. The Caledonides of the Oslo Region, Norway- stratigraphy and structural elements. *Norwegian Journal of Geology,* 90**,** 93-121.

Brøgger, W. C. 1882. *Die silurischen Etagen 2 und 3 im Kristianiagebiet und auf Eker, ihre Gliederung, Fossilien, Schichtentstörungen und Contactmetamorphosen*, AW Brogger.

Brøgger, W. C. 1887. Forelöbig meddelelse om mineralerne på de sydnorske angit-og nefelinsyeniters grorkornige gange. *Geologiska Föreningen i Stockholm Förhandlingar,* 9**,** 247-274.

Bubniak, I., Bubniak, A. & Gavrilenko, O. 2020. Digital field geology. *Geoinformatics: Theoretical and Applied Aspects 2020.* European Association of Geoscientists & Engineers.

Buckley, S. J., Kurz, T. H., Howell, J. A. & Schneider, D. 2013. Terrestrial lidar and hyperspectral data fusion products for geological outcrop analysis. *Computers & Geosciences,* 54**,** 249-258.

Baarli, B. G. & Harper, D. A. 1986. Relict Ordovician brachiopod faunas in the lower Silurian of Asker, Oslo region, Norway. *Norsk Geologisk Tidsskrift,* 66**,** 87-97.

Caine, J. S., Evans, J. P. & Forster, C. B. 1996. Fault zone architecture and permeability structure. *Geology,* 24**,** 1025-1028.

Cardozo, N. & Allmendinger, R. W. 2013. Spherical projections with OSXStereonet. *Computers & Geosciences,* 51**,** 193-205.

Childs, C., Walsh, J. & Watterson, J. 1997. Complexity in fault zone structure and implications for fault seal prediction. *Norwegian Petroleum Society Special Publications.* Elsevier.

Cocks, L. & Torsvik, T. 2002. Earth geography from 500 to 400 million years ago: a faunal and palaeomagnetic review. *Journal of the Geological Society,* 159**,** 631-644.

Cocks, L. R. M. & Torsvik, T. H. 2005. Baltica from the late Precambrian to mid-Palaeozoic times: the gain and loss of a terrane's identity. *Earth-Science Reviews,* 72**,** 39-66.

Dahlstrom, C. 1969. Balanced cross sections. *Canadian Journal of Earth Sciences,* 6**,** 743-757.

De Paor, D. & Anastasio, D. 1987. The Spanish External Sierra: a case history in the advance and retreat of mountains. *National Geographic Research,* 3**,** 199-209.

Dehli, G. 2012. *The geometry and structural development of Caledonian folds and faults, inner Oslofjord.* MSc, University of Oslo.

Dewey, J. F. 1969. Evolution of the Appalachian/Caledonian orogen. *Nature,* 222**,** 124-129.

Dowman, I. 2004. Integration of LiDAR and IFSAR for mapping. *International Archives of Photogrammetry and Remote Sensing,* 35**,** 90-100.

Drost, K., Chew, D., Petrus, J. A., Scholze, F., Woodhead, J. D., Schneider, J. W. & Harper, D. A. 2018. An image mapping approach to U-Pb LA-ICP-MS carbonate dating and applications to direct dating of carbonate sedimentation. *Geochemistry, Geophysics, Geosystems,* 19**,** 4631-4648.

Feng, L., Bartholomew, M. J. & Choi, E. 2015. Spatial arrangement of décollements as a control on the development of thrust faults. *Journal of Structural Geology,* 75**,** 49-59.

Fleuty, M. 1964. The description of folds. *Proceedings of the Geologists' Association,* 75**,** 461-492.

Fossen, H. 2010. Extensional tectonics in the North Atlantic Caledonides: a regional view. *Geological Society, London, Special Publications,* 335**,** 767-793.

Fossen, H. 2016. *Structural geology*, Cambridge university press.

Fossen, H., Cavalcante, G. C. & De Almeida, R. P. 2017. Hot versus cold orogenic behavior: Comparing the Araçuaí-West Congo and the Caledonian orogens. *Tectonics,* 36**,** 2159-2178.

Fossen, H. & Dunlap, W. J. 1998. Timing and kinematics of Caledonian thrusting and extensional collapse, southern Norway: evidence from 40Ar/39Ar thermochronology. *Journal of structural geology,* 20**,** 765-781.

Fung, J. 2016. *Fold Structure* [Online]. Own work. Available: https://commons.wikimedia.org/wiki/File:Fold_terminology-01.jpg [Accessed 12.01.2022].

Gabriel, V. & Miller, R. J. 1952. Apparent dip-true dip formula using a unit hemisphere. *Eos, Transactions American Geophysical Union,* 33**,** 734-738.

Gabrielsen, R. H., Braathen, A., Dehls, J. & Roberts, D. 2002. Tectonic lineaments of Norway. *Norsk Geologisk Tidsskrift,* 82**,** 153-174.

Gabrielsen, R. H., Nystuen, J. P., Jarsve, E. M. & Lundmark, A. M. 2015. The Sub-Cambrian Peneplain in southern Norway: its geological significance and its implications for post-Caledonian faulting, uplift and denudation. *Journal of the Geological Society,* 172**,** 777-791.

Gee, D. G. 1978. Nappe displacement in the Scandinavian Caledonides. *Tectonophysics,* 47**,** 393-419.

Google Earth. 2016. *V 9.157.0.0 WebAssembly* [Online]. Available: https://earth.google.com/web/@60.284627,10.45164825,350.20193737a,7001.52481539d,35y,0h,0t,0r [Accessed 28.02.2022].

Groshong Jr, R. H. 2006. *3-D structural geology*, Springer.

Hearn, P., Hare, T., Schruben, P., Sherill, D., Lamar, C., Tsushima,P. 2003. Global GIS Europe and Eurasia disks developed by the U.S. *Geological Survey. American Geophysical Union. Two discs.*

Heeremans, M., Larsen, B. T. & Stel, H. 1996. Paleostress reconstruction from kinematic indicators in the Oslo Graben, southern Norway: new constraints on the mode of rifting. *Tectonophysics,* 266**,** 55-79.

Henningsmoen, G. 1982. The Ordovician of the Oslo Region. A short history of research. *Field Excursion Guide. IV International Symposium on the Ordovician System, Oslo-Norway.* Paleontological Contributions from the University of Oslo.

Henningsmoen, G. & Dons, J. 1978. Sedimentary rocks associated with the Oslo region lavas. *The Oslo paleorift. A review guide to excursions. Norges Geologiske Undersøkelse Bulletin,* 337**,** 17-24.

Hjelseth, E. V. D. F. 2010. *Caledonian structuring of the Silurian succession at Sundvollen, Ringerike, southern Norway.* MSc, University of Oslo.

Holtedahl, O. & Schetelig, J. 1923. Kartbladet Gran. *Norges geologiske under-søkelse 97,* 1-46.

Hossack, J. & Cooper, M. 1986. Collision tectonics in the Scandinavian Caledonides. *Geological Society, London, Special Publications,* 19**,** 285-304.

Jakob, J., Andersen, T. B. & Kjøll, H. J. 2019. A review and reinterpretation of the architecture of the South and South-Central Scandinavian Caledonides—A magma-poor to magma-rich transition and the significance of the reactivation of rift inherited structures. *Earth-Science Reviews,* 192**,** 513-528.

Johnson, G., Raynolds, R., Burbank, D., Allen, P. & Homewood, P. 1986. Foreland basins. *International Association of Sedimentologists Special Publication 8***,** 273-291.

Johnson, M. D., Fredin, O., Ojala, A. E. & Peterson, G. 2015. Unraveling Scandinavian geomorphology: the LiDAR revolution. Taylor & Francis.

Kartverket. 2015. *Høydedata, Euref89 UTM33* [Online]. Available: https://hoydedata.no/LaserInnsyn/ [Accessed 08.06.2021].

Kiær, J. A. 1897. *Faunistische Uebersicht der Etage 5 des norwegischen Silursystems*, Ludwig-Maximilians Universität München.

Kiær, J. A. 1902. Etage 5 i Asker ved Kristiania (English Summary). *Nor. Geol. Unders. Skr,* 34**,** 1-112.

Kiær, J. A. 1908. *Das Obersilur im Kristianiagebiete: eine stratigraphisch-faunistische Untersuhung*, Jacob Dybwad.
Kiær, J. A. 1917. *The Lower Cambrian Holmia fauna at Tømten in Norway*, In commission at J. Dybwad.
Kjerulf, T. 1857. *Ueber die Geologie des südlichen Norwegens*, J. Dahl.
Kjerulf, T. 1862. Beskrivelse over jordbunden paa Hadeland. *Polytekn. Tidskr. Aarg,* 9.
Kjerulf, T. 1879. *Udsigt over det sydlige Norges geologi*, WC Fabritius.
Korja, T., Smirnov, M., Pedersen, L. & Gharibi, M. 2008. Structure of the Central Scandinavian Caledonides and the underlying Precambrian basement, new constraints from magnetotellurics. *Geophysical Journal International,* 175**,** 55-69.
Koyi, H. A., Sans, M., Teixell, A., Cotton, J. & Zeyen, H. 2004. The significance of penetrative strain in the restoration of shortened layers—Insights from sand models and the Spanish Pyrenees.
Larsen, B. T., Olaussen, S., Sundvoll, B. & Heeremans, M. 2008. The Permo-Carboniferous Oslo Rift through six stages and 65 million years. *Episodes,* 31**,** 52-58.
Lauritzen, Ø. 1973. THE MIDDLE ORDOVICIAN OF THE OSLO REGION, NORWAY 24. STAGE 4b AT LUNNER, HADELAND. *Norsk Geologisk Tidsskrift,* 53**,** 25-40.
Mitra, S. 1990. Fault-propagation folds: geometry, kinematic evolution, and hydrocarbon traps. *AAPG bulletin,* 74**,** 921-945.
Morley, C. K. 1983. *The structural geology of the southern Norwegian Caledonides in the Oslo graben and sparagmite region.* City of London Polytechnic.
Morley, C. K. 1986. The Caledonian thrust front and palinspastic restorations in the southern Norwegian Caledonides. *Journal of Structural geology,* 8**,** 753-765.
Morley, C. K. 1987a. Lateral and vertical changes of deformation style in the Osen-Røa thrust sheet, Oslo Region. *Journal of Structural Geology,* 9**,** 331-343.
Morley, C. K. 1987b. The structural geology of north Hadeland. *Norsk geologisk tidsskrift,* 67**,** 39-49.
Morley, C. K. 1989. Basin inversion in the Osen-Røa thrust sheet, Southern Norway. *Geological Society, London, Special Publications,* 44**,** 259-273.
Morley, C. K. 1994. Fold-generated imbricates: examples from the Caledonides of Southern Norway. *Journal of Structural Geology,* 16**,** 619-631.
Neumann, E.-R., Olsen, K., Baldridge, W. & Sundvoll, B. 1992. The Oslo rift: A review. *Tectonophysics,* 208**,** 1-18.
NGU. 2021a. *Berggrunn - Nasjonal berggrunnsdatabase* [Online]. Available: http://geo.ngu.no/kart/berggrunn_mobil/ [Accessed 08.06.2021].
NGU. 2021b. *Skøyengruppen* [Online]. Database for geologiske enheter. Available: https://aps.ngu.no/pls/utf8/geoenhet_SokiDb.Vis_enhet?p_id=158130&p_spraak=N [Accessed 22.11.2021].
Nicholson, R. & Rutland, R. 1969. A section across the Norwegian Caledonides; Bodø to Sulitjelma.
Nordgulen, Ø. 1999. Geologisk kart over norge, berggrunnskart HAMAR, M 1:250 000. *Norges geologiske under-søkelse*.
Novakova, L. & Pavlis, T. L. 2017. Assessment of the precision of smart phones and tablets for measurement of planar orientations: A case study. *Journal of Structural Geology,* 97**,** 93-103.
Novakova, L. & Pavlis, T. L. 2019. Modern methods in structural geology of twenty-first century: Digital mapping and digital devices for the field geology. *Teaching methodologies in structural geology and tectonics.* Springer.
Nuriel, P., Weinberger, R., Kylander-Clark, A., Hacker, B. & Craddock, J. 2017. The onset of the Dead Sea transform based on calcite age-strain analyses. *Geology,* 45**,** 587-590.

Nystuen, J. P. 1981. The late Precambrian" sparagmites" of southern Norway; a major Caledonian allochthon; the Osen-Roa nappe complex. *American Journal of Science,* 281**,** 69-94.
Nystuen, J. P. 1983. Nappe and thrust structures in the Sparagmite region, southern Norway.
Nystuen, J. P., Andresen, A., Kumpulainen, R. A. & Siedlecka, A. 2008. Neoproterozoic basin evolution in Fennoscandia, East Greenland and Svalbard. *Episodes,* 31**,** 35-43.
Ogg, J. G., Gradstein, F. M. & Smith, A. G. 2004. *A geologic time scale 2004*, Cambridge University Press.
Olaussen, S., Larsen, B. T. & Steel, R. 1994. The Upper Carboniferous-Permian Oslo Rift; basin fill in relation to tectonic development.
Owen, A. W. 1978. The Ordovician and Silurian stratigraphy of central Hadeland, south Norway.
Owen, A. W., Bruton, D. L., Bockelie, J. F. & Bockelie, T. G. 1990. The Ordovician successions of the Oslo region, Norway.
Owen, A. W., Olerud, S. & Morley, C. K. 2001. *Gran. Berggrunnskart; Gran; 18151; 1:50 000; Foreløpig utgave plotteversjon* [Online]. Norges Geologiske Undersøkelse. Available: https://www.ngu.no/publikasjon/gran-berggrunnskart-gran-18151-150-000-forel-pig-utgave-plotteversjon [Accessed 28.09.2021].
Pavlis, T. L. & Bruhn, R. L. 2011. Application of LIDAR to resolving bedrock structure in areas of poor exposure: An example from the STEEP study area, southern Alaska. *Bulletin,* 123**,** 206-217.
Perroud, H., Robardet, M. & Bruton, D. 1992. Palaeomagnetic constraints upon the palaeogeographic position of the Baltic Shield in the Ordovician. *Tectonophysics,* 201**,** 97-120.
Pfiffner, O. A. 2017. Thick-skinned and thin-skinned tectonics: a global perspective. *Geosciences,* 7**,** 71.
Poblet, J. & Lisle, R. J. 2011. Kinematic evolution and structural styles of fold-and-thrust belts. *Geological Society, London, Special Publications,* 349**,** 1-24.
QGIS.org. 2021. *QGIS Geographic Information System* [Online]. QGIS Association. Available: http://www.qgis.org [Accessed 15.05.2021].
Ramberg, I. B., Bryhni, I. & Nøttvedt, A. 2007. *Landet blir til: Norges geologi*, Norsk geologisk forening.
Ramberg, I. B. & Larsen, B. T. 1978. Tectonomagnetic evolution. *The Oslo paleorift - A review and guide to excursions,* 337**,** 55-73.
Ramsay, J. G. 1967. Folding and fracturing of rocks. *Mc Graw Hill Book Company,* 568.
Rasbury, E. T. & Cole, J. M. 2009. Directly dating geologic events: U-Pb dating of carbonates. *Reviews of Geophysics,* 47.
Repshus, G. S. 2012. *Caledonian structural development on Hovedøya and Lindøya, in the inner Oslofjord.* MSc, University of Oslo.
Ricketts, B. 2021. *Faults – some common terminology* [Online]. Geological Digressions. Available: https://www.geological-digressions.com/faults-some-common-terminology/ [Accessed 21.03.2022].
Ro, H. & Faleide, J. 1992. A stretching model for the Oslo Rift. *Tectonophysics,* 208**,** 19-36.
Roberts, D. 2003. The Scandinavian Caledonides: event chronology, palaeogeographic settings and likely modern analogues. *Tectonophysics,* 365**,** 283-299.
Roberts, D., Gee, D. G. & Sturt, B. 1985. An introduction to the structure of the Scandinavian Caledonides. *The Caledonide orogen–Scandinavia and related areas,* 1**,** 55-68.
Roberts, D. & Sturt, B. 1980. Caledonian deformation in Norway. *Journal of the Geological Society,* 137**,** 241-250.

Roberts, N. M., Drost, K., Horstwood, M. S., Condon, D. J., Chew, D., Drake, H., Milodowski, A. E., Mclean, N. M., Smye, A. J. & Walker, R. J. 2020. Laser ablation inductively coupled plasma mass spectrometry (LA-ICP-MS) U–Pb carbonate geochronology: strategies, progress, and limitations. *Geochronology,* 2**,** 33-61.

Roberts, N. M. & Walker, R. J. 2016. U-Pb geochronology of calcite-mineralized faults: Absolute timing of rift-related fault events on the northeast Atlantic margin. *Geology,* 44**,** 531-534.

Scheiber, T., Fredin, O., Viola, G., Jarna, A., Gasser, D. & Łapińska-Viola, R. 2015. Manual extraction of bedrock lineaments from high-resolution LiDAR data: methodological bias and human perception. *Gff,* 137**,** 362-372.

Sheehan, P. M. 1973. The relation of Late Ordovician glaciation to the Ordovician-Silurian changeover in North American brachiopod faunas. *Lethaia,* 6**,** 147-154.

Simon, R. I. & Gray, D. R. 1982. Interrelations of mesoscopic structures and strain across a small regional fold, Virginia Appalachians. *Journal of Structural Geology,* 4**,** 271-289.

Sippel, J., Saintot, A., Heeremans, M. & Scheck-Wenderoth, M. 2010. Paleostress field reconstruction in the Oslo region. *Marine and Petroleum Geology,* 27**,** 682-708.

Skjeseth, S. 1963. Contributions to the geology of the Mjøsa districts and the classical sparagmite area in Southern Norway.

Smit, J., Brun, J. & Sokoutis, D. 2003. Deformation of brittle-ductile thrust wedges in experiments and nature. *Journal of Geophysical Research: Solid Earth,* 108.

Spjeldnæs, N. 1955. Middle Cambrian stratigraphy in the Røyken area, Oslo region. *Norsk Geologisk Tidsskrift,* 34**,** 105-121.

Størmer, L. 1943. Kaledonisk dekke-tektonikk på Hadeland. *Norsk geol. tidsskr,* 22**,** 74-91.

Størmer, L. 1945. Remarks on the Tretaspis (Trinucleus) shales of Hadeland. *Norsk geol. tidsskr,* 25**,** 379-425.

Størmer, L. 1953. The Middle Ordovician of the Oslo Region, Norway, 1. Introduction to stratigraphy. *Norsk Geologisk Tidsskrift,* 31**,** 37-141.

Sundvoll, B. & Larsen, B. 1994. Architecture and early evolution of the Oslo Rift. *Tectonophysics,* 240**,** 173-189.

Sundvoll, B., Neumann, E.-R., Larsen, B. & Tuen, E. 1990. Age relations among Oslo Rift magmatic rocks: implications for tectonic and magmatic modelling. *Tectonophysics,* 178**,** 67-87.

Vlieg, M. 2015. *Structural style and evolution of the Caledonian foreland, northeast Tyrifjorden, Oslo Region.* MSc, University of Utrecht.

Wang, J., Ju, N., He, C., Cai, J. & Zheng, D. 2020. Assessment of the accuracy of several methods for measuring the spatial attitude of geological bodies using an android smartphone. *Computers & Geosciences,* 136**,** 104393.

Weekenstroo, M. 2015. *The controlling parameters of the structural style in the Oslo-Asker section: A field and analogue modeling study.* MSc, University of Utrecht.

Woodward, N. B., Boyer, S. E. & Suppe, J. 1989. Balanced geological cross-sections. *American Geophysical Union, Short Course in Geology,* 6**,** 132.

Worsley, D., Aarhus, N., Bassett, M. G., Howe, M., Mørk, A. & Olaussen, S. 1983. *The Silurian succession of the Oslo region*, Universitetsforl.

Yan, D. P., Xu, Y. B., Dong, Z. B., Qiu, L., Zhang, S. & Wells, M. 2016. Fault-related fold styles and progressions in fold-thrust belts: Insights from sandbox modeling. *Journal of Geophysical Research: Solid Earth,* 121**,** 2087-2111.

Zachrisson, E. 1969. *Caledonian Geology of Northern Jämtland-Southern Västerbotten: Köli Stratigraphy and Main Tectonic Outlines*, Svensk reproduktions AB (distr.).

Appendix A

A-Table 1: Analytical setup, operating conditions, and data processing for LA-ICP-MS U-Pb analyses in this study.

Laboratory & Sample Preparation	
Laboratory name	Dept of Earth Science, Trinity College Dublin
Sample type/mineral	Calcite
Sample preparation	Polished rock slab in 25mm epoxy mount, 1µm polish to finish
Imaging	High-resolution scan of mount
Laser ablation system	
Make, Model & type	Teledyne/PhotonMachines Analyte Excite, 193nm, Excimer
Ablation cell & volume	HelEx II Active 2-volume cell; 100mm × 100mm sample area
Laser wavelength (nm)	193nm
Pulse width (ns)	<4ns
Fluence (J.cm^{-2})	06.10.2021: 2.0 J/cm^2 16.11.2021: 2.1 J/cm^2 24.11.2021: 2.2 J/cm^2
Repetition rate (Hz)	50 Hz
Spot size (um)	06.10.2021: 80 µm round 16.11.2021: 95 µm square 24.11.2021: 80 µm round
Sampling mode / pattern	Line raster, 1 pass, 30 µm/sec scan speed
Carrier gas	Optimized daily - 100% He in the cell (c. 0.40 l/min), Ar carrier gas (c. 0.70 l/min) and N_2 (c. 12 ml/min) added at ARIS adaptor
Ablation duration (secs)	06.10.2021: 21 x 66s NIST614, 21 x 42s WC-1, 7 x 184s DBT; Cal12: 40 x 64s, Cal14: 40 x 113s 16.11.2021: 21 x 64s NIST614, 21 x 45s WC-1, 7 x 185s DBT; Cal15: 40 x 93s, Cal19: 24 x 126s 24.11.2021: 24 x 66s NIST614, 24 x 50s WC-1, 8 x 180s DBT; Cal2: 16 x 236s, Cal4: 12 x 308s, Cal7a: 10 x 330s
Cell carrier gas flow (l/min)	06.10.2021: 0.30 l/min in the cell and 0.10 l/min in the cup, 7 ml/min N_2 16.11.2021: 0.275 l/min in the cell and 0.125 l/min in the cup, 12.5 ml/min N_2 24.11.2021: 0.225 l/min in the cell and 0.175 l/min in the cup, 12 ml/min N_2
ICP-MS Instrument	
Make, Model & type	Agilent 7900 quadrupole ICP-MS
Sample introduction	Ablation aerosol via ARIS
RF power (W)	1550W
Carrier gas flow (l/min)	06.10.2021: 0.64 l/min Ar 16.11.2021: 0.65 l/min Ar 24.11.2021: 0.70 l/min Ar
Detection system	Dual-mode discrete dynode electron multiplier
Masses measured and [Integration time per peak (ms)]	06.10.2021: 25 [2], 43 [4], 51 [2], 55 [2], 57 [2], 63 [2], 66 [2], 71 [2], 85 [4], 88 [2], 137 [2], 140 [2], 202 [1], 204 [1], 206 [30], 207 [70], 208 [30], 232 [20], 238 [30] 16.11.2021, 24.11.2021: 25 [2], 43 [4], 51 [2], 55 [2], 57 [2], 63 [2], 66 [2], 71 [2], 85 [4], 88 [2], 137 [2], 140 [2], 202 [1], 204 [1], 206 [40], 207 [80], 208 [40], 232 [30], 238 [40]
Total integration time per reading (secs)	06.10.2021: 250ms / 1.5s after averaging 16.11.2021, 24.11.2021: 300ms / 1.5s after averaging
Sensitvity / Efficiency (%, element)	0.02% U
IC Dead time (ns)	38ns
Data Processing	
Gas blank	≥18s on-peak zero subtracted
Calibration strategy	NIST614 as primary reference material, WC-1 carbonate standard for matrix matching of $^{206}Pb/^{238}U$, DBT carbonate for QC
Reference Material info	NIST614 (concentration data Jochum et al., 2011; Pb isotopes Woodhead and Hergt, 2001) WC-1 (Roberts et al., 2017) DBT (Hill et al., 2016)

Data processing package used / Correction for LIEF	Iolite V3.6 & Monocle & in-house spreadsheet; no LIEF correction for linear rasters
Normalisation and age calculation	Standard bracketing; Iolite Data Reduction Scheme VizualAge_UcomPbine (Chew et al. 2014; based on U-Pb Geochronology DRS of Paton et al., 2010 and VizualAge DRS of Petrus and Kamber, 2012) is used to correct for down hole fractionation and drift and to normalize to primary reference material. Downhole fractionation for linear rasters is modelled using a linear correction (y=a+bx) with zero slope (b=0). U/Pb ages and initial Pb compositions are calculated using Isoplot v4.15 (Ludwig, 2012).
Common-Pb correction, composition and uncertainty	Unanchored regression in Tera-Wasserburg, isochron and 86TW plots, respectively. All model 1. Except WC-1: Anchored regression in TW using an initial $^{207}Pb/^{206}Pb$ of 0.85±0.04 (Roberts et al., 2017) to receive a non-matrix-matched lower intercept age, the corresponding ratio of which is used to calculate the matrix-dependent factor for correction of $^{206}Pb/^{238}U$ ratios of QC and unknowns
Uncertainty level & propagation	Ratios and ages are quoted at 2s. Uncertainty propagation was carried out according to the recommendations of Horstwood et al. (2016) and Roberts et al. (2020). The first uncertainty quoted is a session wide estimate including the data point uncertainty, uncertainty on weighted means of primary reference material ratios and their excess scatter (1.5% to 1.8%). The second uncertainty quoted additionally includes systematic uncertainties (2.8% to 3.0%) such as the uncertainty on the reference age of WC-1, uncertainty on the ^{238}U decay constant and a laboratory-specific long-term reproducibility based on the results of the QC material.
Quality control / Validation	*DBT (Hill et al., 2016: 64.04 ± 0.67 Ma / 0.738 ± 0.010)* 06.10.2021: Lower Intercept Age = 65.1±1.1/2.1 Ma, $^{207}Pb/^{206}Pb_{initial}$ = 0.710±0.021 (2s, MSWD = 0.59) 16.11.2021: Lower Intercept Age = 64.5± 1.1/2.2 Ma, $^{207}Pb/^{206}Pb_{initial}$ = 0.692±0.020 (2s, MSWD = 1.03) 24.11.2021: Lower Intercept Age = 64.2± 1.0/2.1 Ma, $^{207}Pb/^{206}Pb_{initial}$ = 0.708±0.015 (2s, MSWD = 0.94)
Other information	All samples were cleaned with ethanol followed by sonication in DIW. Potentially remaining surface contamination was removed during a preablation of all ablated sites. Detailed information on the general analytical protocol and data processing is given in Drost et al. (2018) in addition to all references referred to in this table.

A-Table 2: General information about sampled calcites from the field. Highlighted samples are dated, while the rest did not hold favorable U/Pb relations for further dating.

Sample ID	Date collected	Lithological unit	Strike/dip of sample	Lineation (plunge/azimuth)	Coordinates	Comments
Cal 0	09.08.2021	Skøyen Gr.	-	-	60.3407260, 10.5039487	Precipitation
Cal 1	11.08.2021	Skøyen Gr.	115/89	-	60.3407467, 10.5038209	Fault, no lineations
Cal 2	11.08.2021	Skøyen Gr.	268/78	-	60.3398528, 10.5039005	Precipitation
Cal 3	11.08.2021	L/G/K Fm.	075/24	-	60.3268546, 10.4884469	Fault
Cal 4	11.08.2021	Bruflat Fm.	183/88	-	60.2563129, 10.4667680	Fault
Cal 5	11.08.2021	Bruflat Fm.	248/21	19/006	60.2572717, 10.4706479	Lineations in area, not on sample
Cal 6	12.08.2021	Bruflat Fm.	359/76	62/025	60.2619794, 10.4888041	Wall of intrusion
Cal 7	12.08.2021	Bruflat Fm.	357/75	56/023	60.2619949, 10.4888256	Wall of intrusion
Cal 8	12.08.2021	Bruflat Fm.	069/51	53/161	60.2619228, 10.4886591	-
Cal 9	12.08.2021	Bruflat Fm.	069/51	46/167	60.2619128, 10.4886781	-

Cal 10	12.08.2021	Bruflat Fm.	075/49	49/163	60.2621000, 10.4893989	Reverse fault (?)
Cal 11	12.08.2021	Bruflat Fm.	075/49	49/163	60.2621000, 10.4893989	Reverse fault (?)
Cal 12	12.08.2021	Kalvsjøen Fm.	032/73	24/041	60.2923136, 10.5796618	Reverse fault
Cal 13	12.08.2021	Kalvsjøen Fm.	029/76	01/028	60.2969775, 10.5554529	Strike/slip movement
Cal 14	12.08.2021	Kalvsjøen Fm.	029/76	01/028	60.2969775, 10.5554529	Strike/slip movement
Cal 15	12.08.2021	Kalvsjøen Fm.	163/75	Fiber growth orientation 06/074	60.2966255, 10.5554227	N-S oriented vein
Cal 16	12.08.2021	L/G/K Fm.	030/68	26/040	60.3576366, 10.4169477	-
Cal 17	12.08.2021	Kirkerud Gr.	083/39	37/129	60.3919917, 10.4659914	-
Cal 18	12.08.2021	Kirkerud Gr.	189/40	38/267	60.3919137, 10.4655649	Normal fault
Cal 19	12.08.2021	Kirkerud Gr.	158/06	00/338	60.3987176, 10.4829376	-
Cal 20	12.08.2021	Kirkerud Gr.	254/27	Vein orientation 087/72	60.3987403, 10.4829606	-
Cal 21	12.08.2021	Kirkerud Gr.	275/66	30/084 (uncertain)	60.3987379, 10.4830025	-
Cal 22	16.08.2021	Kirkerud Gr.	023/77	38/035	60.3710724, 10.5437736	Thrust
Cal 23	18.08.2021	Kalvsjøen Fm.	160/49	43/221	60.2782434, 10.4997645	Thrust
Cal 23b	18.08.2021	Kalvsjøen Fm.	-	-	60.2782434, 10.4997645	Extra sample for Cal 23
Cal 24	21.08.2021	Solvang Fm.(?)	178/84	05/000	60.3267259, 10.5125651	-
Cal 25	21.08.2021	Bruflat Fm.	159/69	75/164	60.3081358, 10.4317908	Unsure if calcite
Cal 26	22.08.2021	L/G/K Fm.	042/69	33/064	60.3132892, 10.3845624	Thrust in antiform
Cal 27	23.08.2021	Kalvsjøen Fm.	023/85	48/091	60.2959663, 10.5677680	Thrust with strike N-S
Cal 28	23.08.2021	Kalvsjøen Fm.	043/68	53/077	60.2959912, 10.5677769	Thrust with strike N-S

All comments and results from dating of calcites:

Performed by Dr. Kerstin Drost at Trinity College, Dublin. All comments and figures written and produced by Dr. Kerstin Drost. Received 21.04.2022 and esthetically modified.

Description for pictures in the figures can be seen in Figure 4.6. See references cited in subchapter 4.4.3 for further information.

Cal 2

General comments:

- Very low U (<100 ppb) and Pb concentrations and presumedly very young age(?) → not enough production of radiogenic Pb.
- Not enough spread of data points in isochron diagrams.
- Poor counting statistics due to low signals.
- Highest U concentrations are on grain boundaries → not clear whether that U was incorporated during calcite precipitation. It could as well have accumulated during a later stage or it could represent material that became trapped between crystals during crystallization.

Information regarding dating of sample:

- U-Pb data for both concordia diagrams are based on the same data set
- Criteria used for selection of pixels:
    - Ca>350000 ppm and Rb<0.1 ppm to include only the calcite and to avoid cracks/cavities and major impurities.
    - 206Pb, 207Pb, 208Pb and 238U > 0 cps to avoid negative values after baseline substraction for time slices with particularly low U and Pb signals.
- Pooling by ECDF of 207Pb/235U into:
    - Left: 54 pseudo-analyses.
    - Right: 108 pseudo-analyses.
- The results are identical within uncertainty. Precision is very poor due to poor counting statistics and limited spread of data points.

Cal 4

General comments:

- Extremely low U (<40 ppb) and Pb concentrations and presumedly very young age(?) → not enough production of radiogenic Pb.
- Spread of data points in isochron diagrams is not too bad, but counting statistics are really poor due to the very low signals.

Information regarding dating of sample:

- Criteria used for selection of pixels:
    - Ca_ppm_SQ_m43>350000 to avoid cracks and voids.
    - Th_ppm_SQ_m232<0.1 to avoid detrital material as much as possible.
    - U238_CPS>100; Pb207_CPS>50; Pb206_CPS>0 to avoid U- and Pb-free areas.
- Pooling by ECDF of 207Pb/235U ratio into 68 pseudo-analyses.
- Counting statistics are not great and the limited spread of the data points result in a very imprecise and possibly inaccurate age.

Cal 7a

General comments:

- The sample consists of a mixture of precipitated calcite and detrital material. Both components can't be separated from each other by selection criteria or regions of interest. Therefore, the significance of the obtained U-Pb dates is not clear
- U and Pb concentrations are reasonable but see point above and not enough spread in isochron diagrams.

Information regarding dating of sample:

- Criteria used for selection of pixels:
    - Mg_ppm_SQ_m25<3000; Rb_ppm_SQ_m85<0.1; U_ppm_SQ_m238<2.5; U238_CPS>100
- Pooling by ECDF of 207Pb/235U ratio into 70 pseudo-analyses.
- Counting statistics are fine but the limited spread of the data points results in a very imprecise and possibly inaccurate age. Moreover, and more importantly the heterogeneity of the sample (authigenic vs. detrital vs. ???) casts doubt about the significance of the obtained age.

Cal 12

General comments:

- Very low U (<70 ppb) and Pb concentrations.
- Not enough spread of data points in isochron diagrams.
- Relatively poor counting statistics due to low signals.
- Likely some contamination by detrital material.

Information regarding dating of sample:

- Criteria used for selection of pixels:
    - Ca_ppm_SQ_m43>300000 to avoid cracks and voids.
    - Th_ppm_SQ_m232<0.1 to avoid detrital material as much as possible.
    - U238_CPS>100; Pb207_CPS>10; Pb206_CPS>10 to avoid U- and Pb-free areas.
- Pooling by ECDF of Final238_208 into 66 pseudo-analyses.

- Counting statistics are not great and the very limited spread of the data points result in a very imprecise and possibly inaccurate age.

Cal 14

General comments:

- U concentration in indicated area too low, mapped different part of sample instead.
- The age for the brown material is imprecise but rather accurate.
- Data on the light material (ankerite?) that is also covered by the map are inconclusive.

Information regarding dating of sample:

- Criteria used for selection of pixels:
  - U_ppm_SQ_m238>0.15 to target brown material only which has a higher U concentration.
- Pooling by ECDF of Final238_208 into 66 pseudo-analyses.
- Counting statistics are reasonable but spread is limited, thus the calculated age is rather imprecise.

Cal 15

General comments:

- Very low U (<60 ppb) and radiogenic Pb concentrations.
- Not enough spread of data points in isochron diagrams.
- Rather poor counting statistics due to low signals.
- Age probably accurate within uncertainty.

Information regarding dating of sample:

- Criteria used for selection of pixels:
  - Th_ppm_SQ_m232<0.1 to exclude sediment on the left and U238_CPS>100.
- Pooling by ECDF of Pb/U into 58 pseudo-analyses with c. 60s of signal each.
- Counting statistics are poor and spread is limited, thus the calculated age is rather imprecise.

Cal 19

General comments:

- Very low U (<100 ppb) and radiogenic Pb concentrations.
- Not enough spread of data points in isochron diagrams.
- Poor counting statistics for U due to low signals.

Information regarding dating of sample:

- Criteria used for selection of pixels:
  - Th_ppm_SQ_m232<0.1 to exclude sediment on the right.
  - Rb_ppm_SQ_m85<0.1 to exclude potential fluid pathway.
  - Ba_ppm_SQ_m137<10 to exclude suspicious high Ba feature (barite inclusion?).
  - U238_CPS>100.
- Pooling by ECDF of Pb/U into 40 pseudo-analyses with c. 60s of signal each.
- Counting statistics are poor and spread is very limited, thus the calculated age is imprecise and possibly inaccurate.

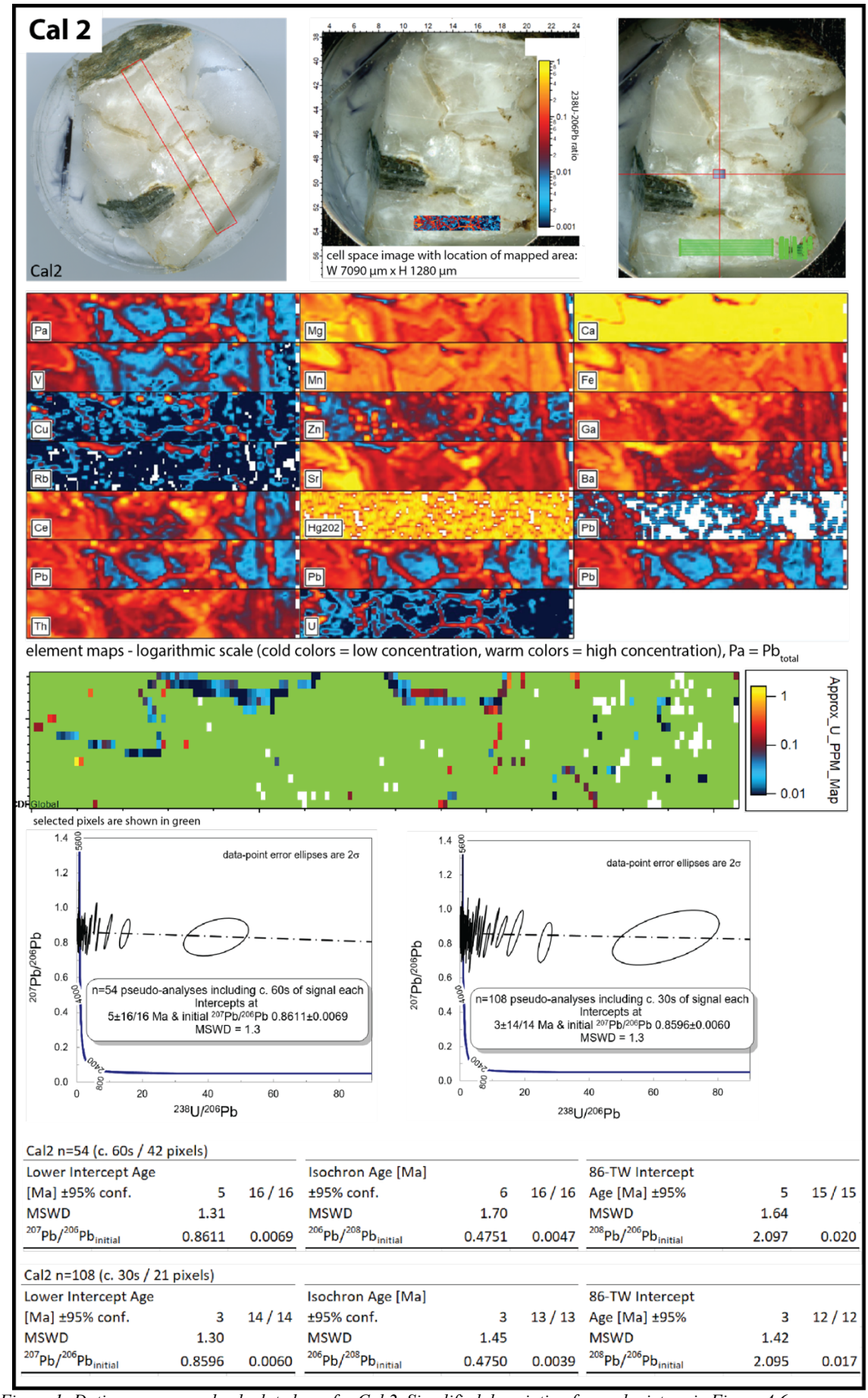

Cal2 n=54 (c. 60s / 42 pixels)			Isochron Age [Ma]			86-TW Intercept		
Lower Intercept Age								
[Ma] ±95% conf.	5	16 / 16	±95% conf.	6	16 / 16	Age [Ma] ±95%	5	15 / 15
MSWD	1.31		MSWD	1.70		MSWD	1.64	
$^{207}Pb/^{206}Pb_{initial}$	0.8611	0.0069	$^{206}Pb/^{208}Pb_{initial}$	0.4751	0.0047	$^{208}Pb/^{206}Pb_{initial}$	2.097	0.020

Cal2 n=108 (c. 30s / 21 pixels)			Isochron Age [Ma]			86-TW Intercept		
Lower Intercept Age								
[Ma] ±95% conf.	3	14 / 14	±95% conf.	3	13 / 13	Age [Ma] ±95%	3	12 / 12
MSWD	1.30		MSWD	1.45		MSWD	1.42	
$^{207}Pb/^{206}Pb_{initial}$	0.8596	0.0060	$^{206}Pb/^{208}Pb_{initial}$	0.4750	0.0039	$^{208}Pb/^{206}Pb_{initial}$	2.095	0.017

A-Figure 1: Dating process and calculated age for Cal 2. Simplified description for each picture in Figure 4.6.

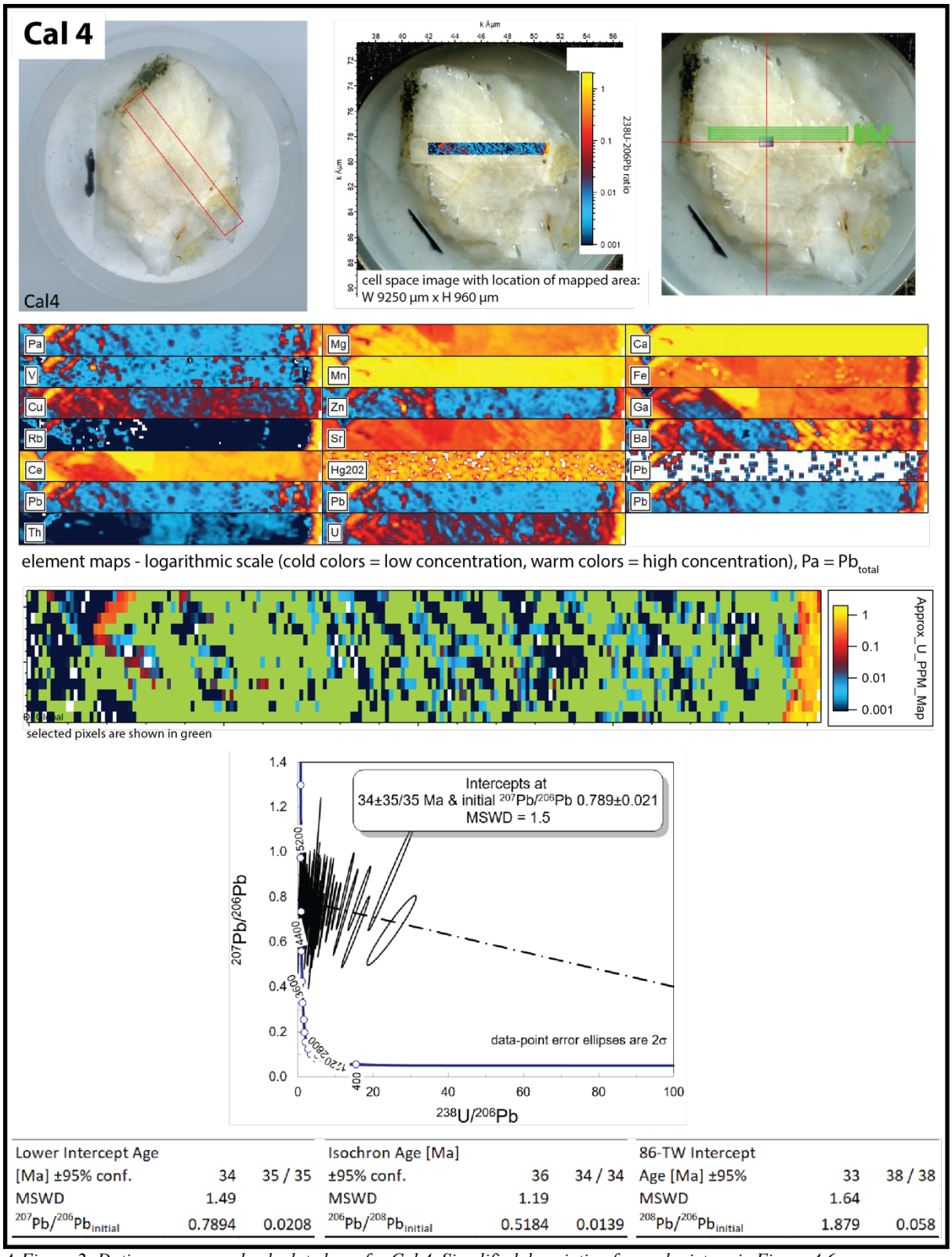

A-Figure 2: Dating process and calculated age for Cal 4. Simplified description for each picture in Figure 4.6.

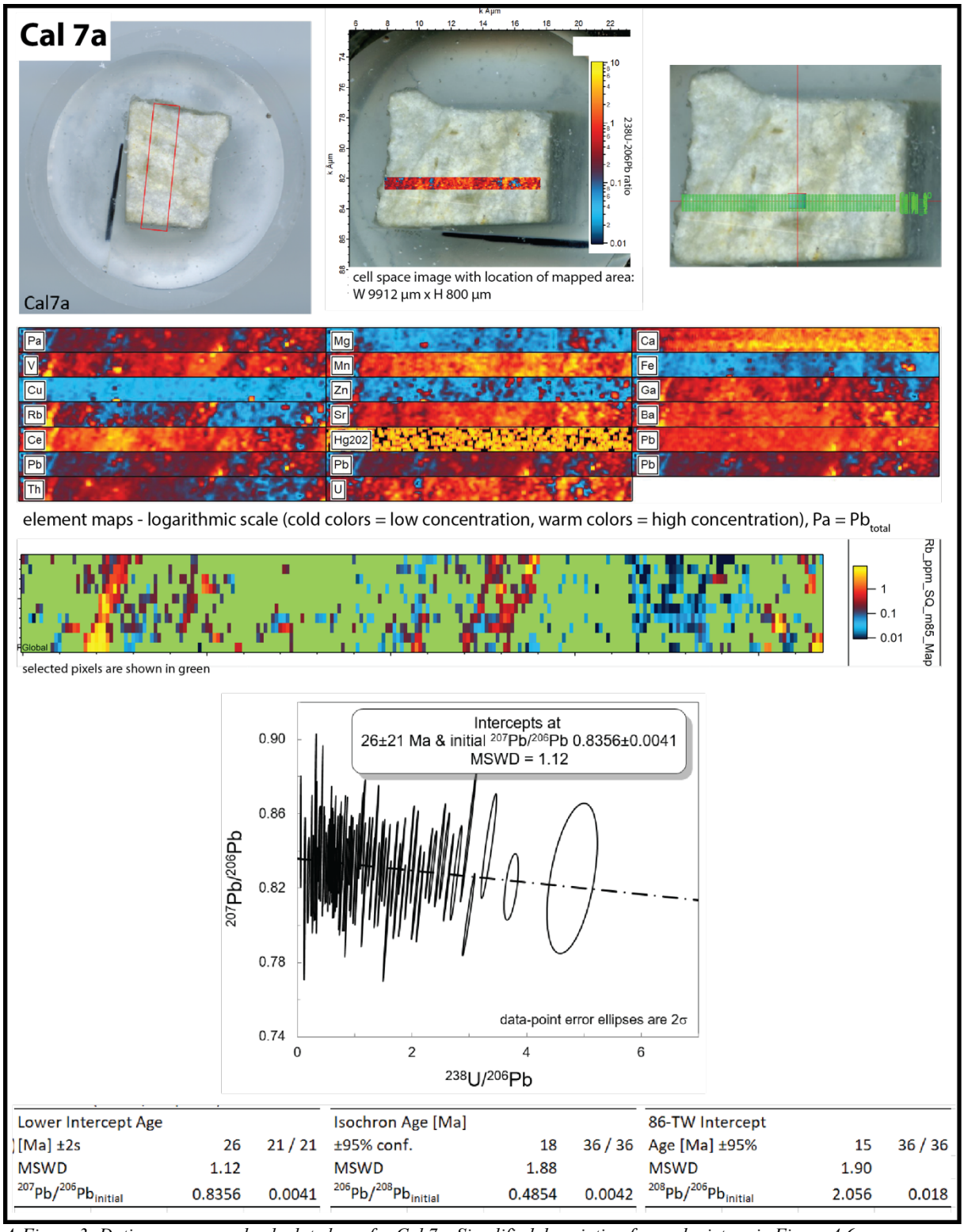

A-Figure 3: Dating process and calculated age for Cal 7a. Simplified description for each picture in Figure 4.6.

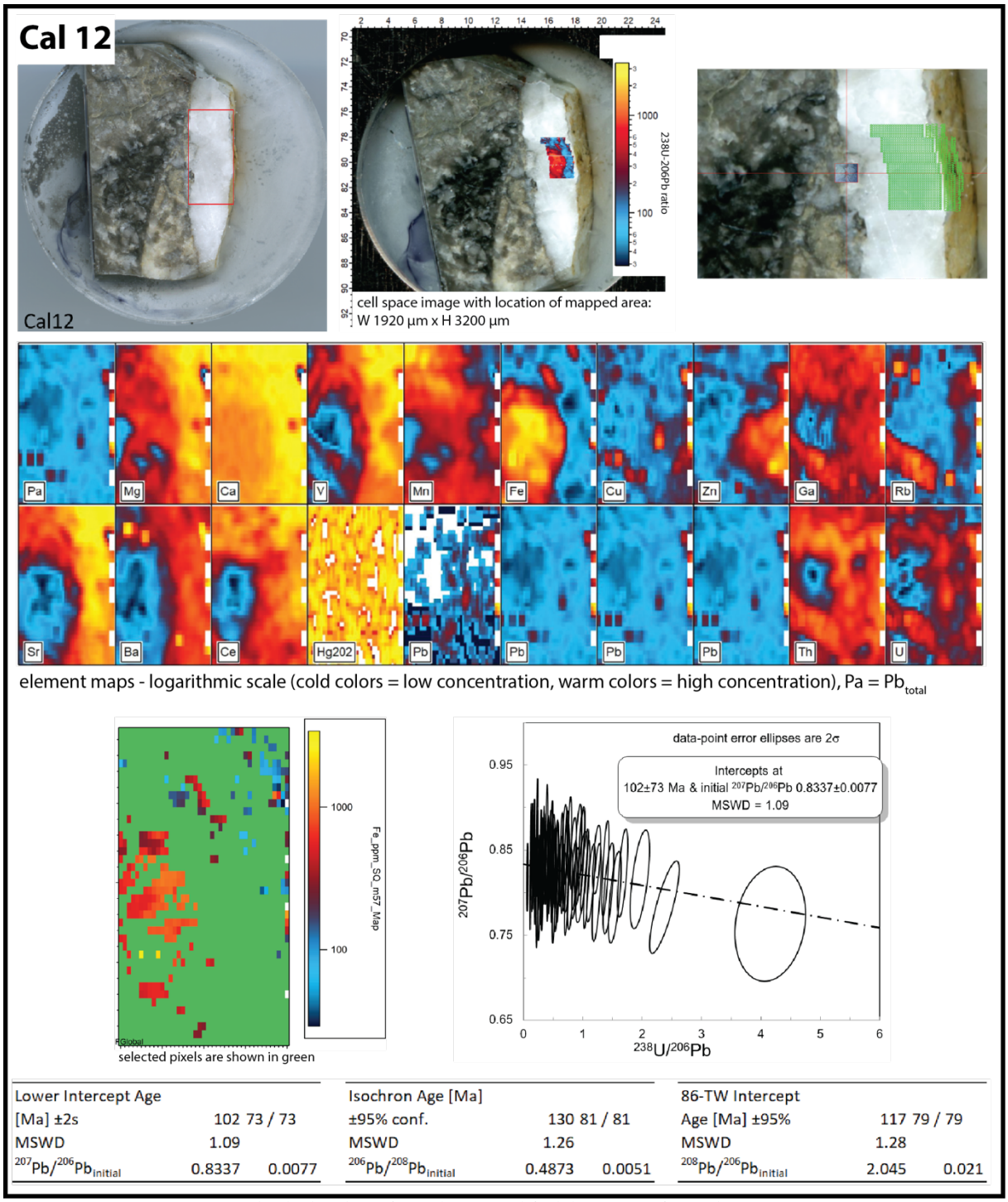

A-Figure 4: Dating process and calculated age for Cal 12. Simplified description for each picture in Figure 4.6.

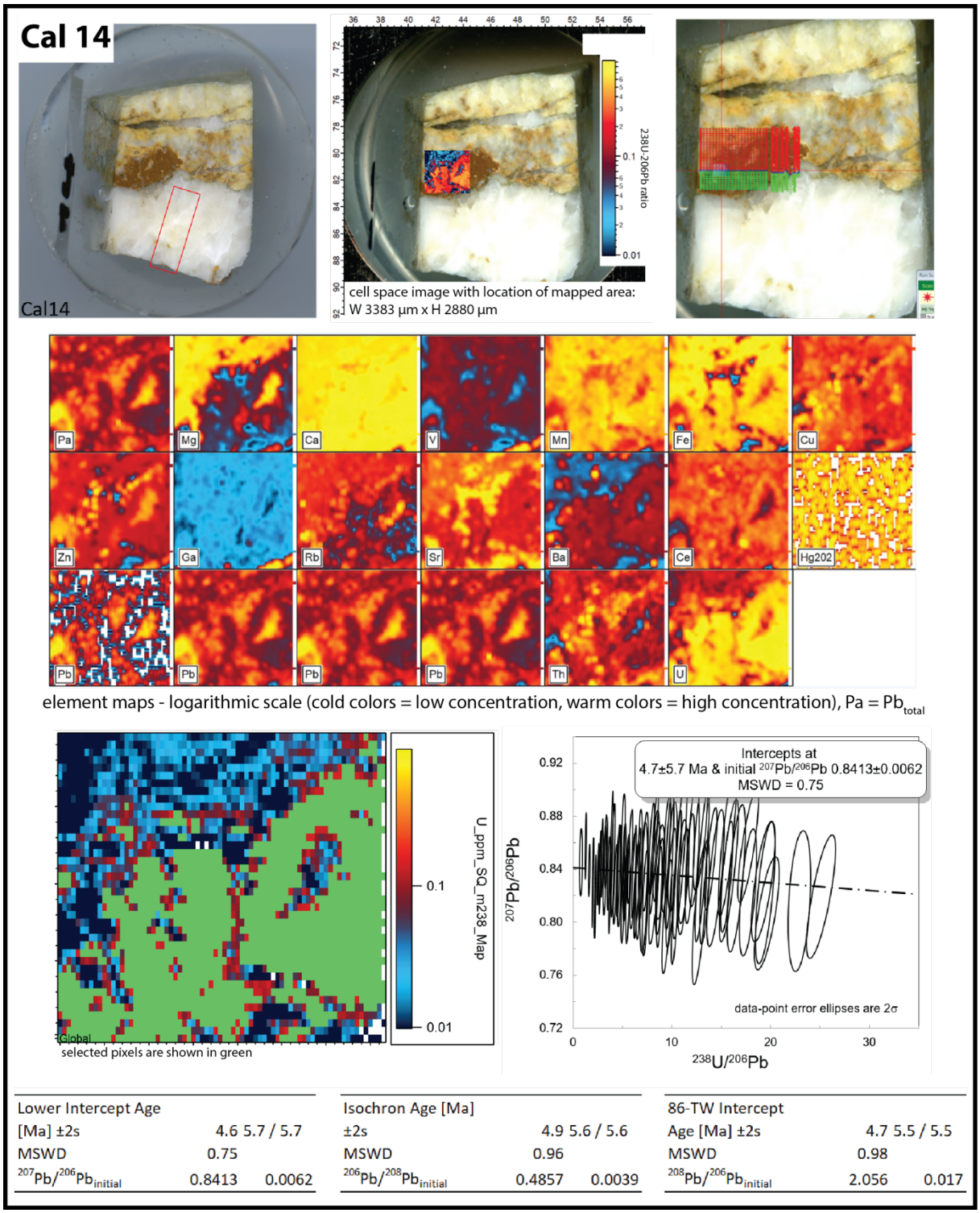

A-Figure 5: Dating process and calculated age for Cal 14. Simplified description for each picture in Figure 4.6.

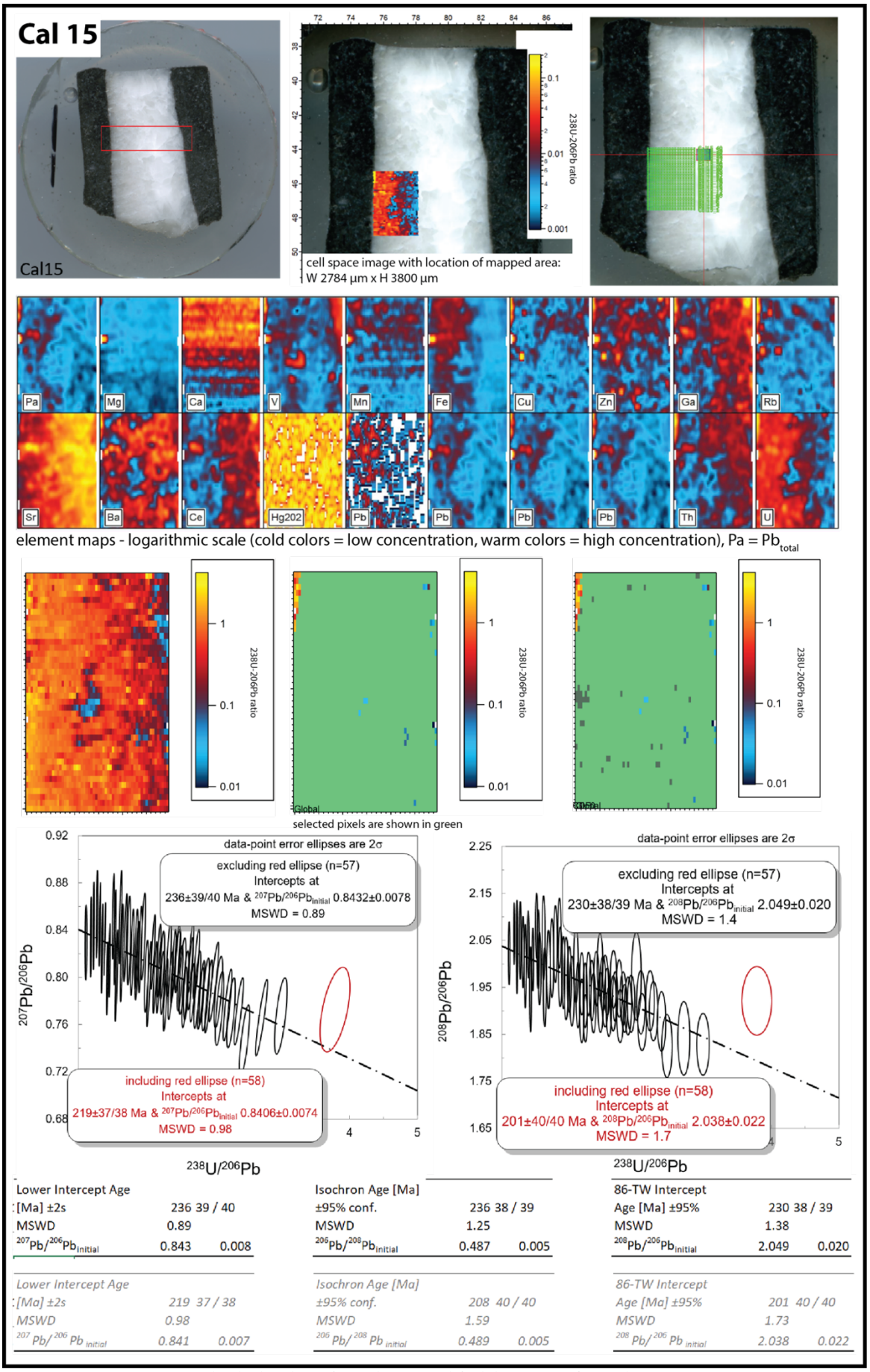

A-Figure 6: Dating process and calculated age for Cal 15. Simplified description for each picture in Figure 4.6.

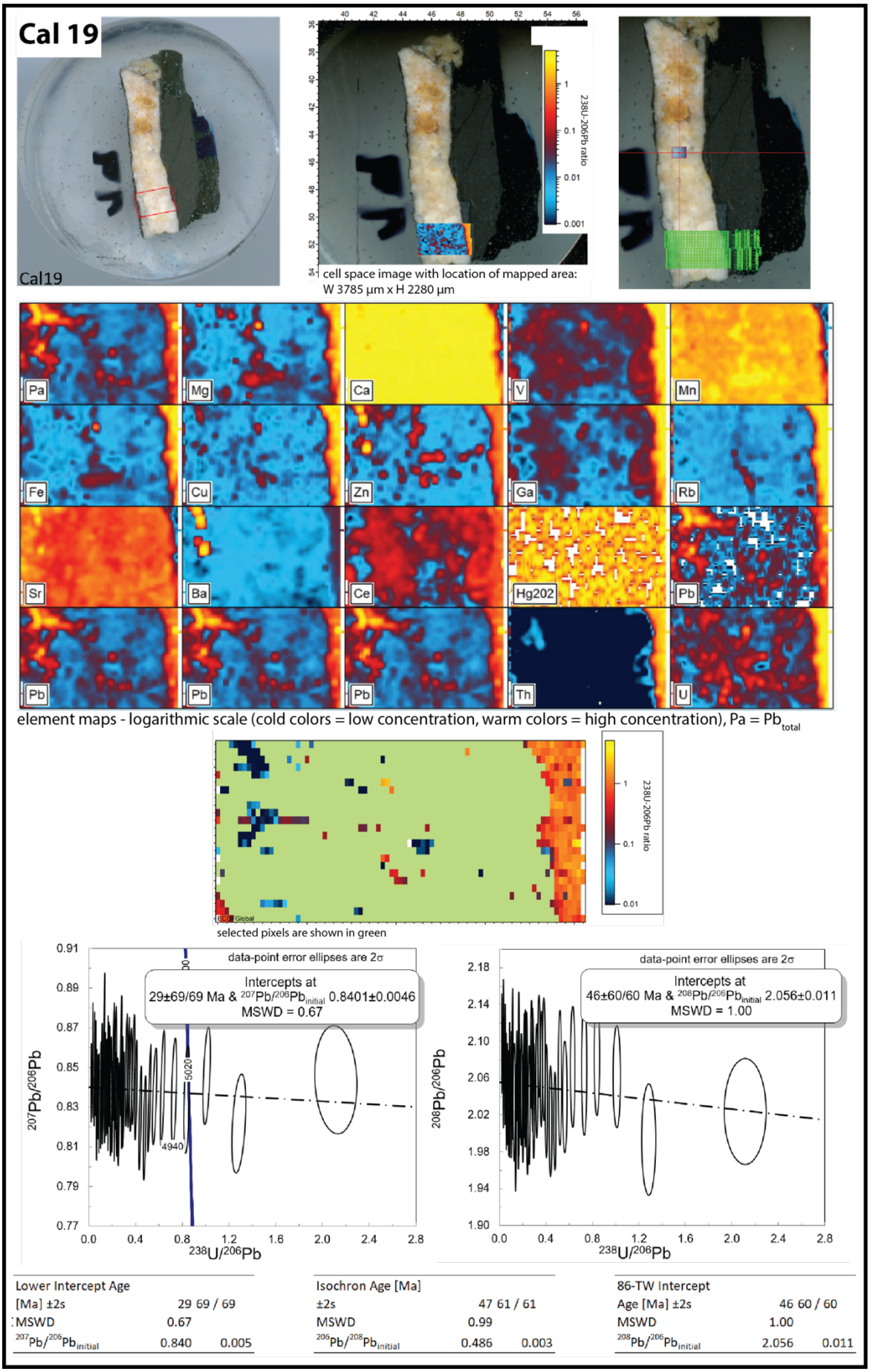

A-Figure 7: Dating process and calculated age for Cal 19. Simplified description for each picture in Figure 4.6.